Stefan Bernsteiner

Integration of Advanced Driver Assistance Systems on Full-Vehicle Level

Monographic Series TU Graz

Reihe Fahrzeugtechnik   Band 6

Herausgeber:
Institut für Fahrzeugtechnik

Monographic Series TU Graz

Stefan Bernsteiner

Integration of Advanced Driver Assistance Systems on Full-Vehicle Level

Parametrization of an Adaptive Cruise Control System Based on Test Drives

Erschienen in der Reihe Fahrzeugtechnik der Monographic Series

Band 1 Niederkofler, Haymo

Analyse radselektiv eingreifender Fahrdynamikregelsysteme für die Anwendung in Elektromechanischen Corner-Modulen, Dissertation, Verlag der TU Graz, ISBN 978-3-85125-220-0, 2012

Band 2 Rojas Rojas, Andrés Eduardo

Passenger Vehicles with In-Wheel Motors: Fundamentals, Potentials and Limitations, Dissertation, Verlag der TU Graz, ISBN 978-3-85125-234-7, 2012

Band 3 Daniel Wallner

Experimental and Numerical Investigations on Brake Squeal, Dissertation, Verlag der TU Graz, ISBN 978-3-85125-269-9, 2013

Band 4 Alexander Harrich

CAD-basierte Methoden zur Unterstützung der Karosseriekonstruktion in der Konzeptphase, Dissertation, Verlag der TU Graz, ISBN 978-3-85125- 420-4, 2015

Band 5 Cornelia Lex

Maximum Tire-Road Friction Coefficient Estimation, Dissertation, Verlag der TU Graz, ISBN 978-3-85125-422-8, 2015

Acknowledgement

Stefan Bernsteiner
Graz, May 2015

Abstract

Advanced Driver Assistance Systems (ADAS) support drivers in fulfilling their driving task by reducing workload and enabling a more safe and comfortable drive. However, the increasing market penetration of ADAS, along with the wide variety of types and models, has led to a need for a cost and time-efficient way to integrate and parametrize new systems. One essential point for the integration process of comfort-oriented ADAS is the question of driver satisfaction with respect to safety, reliability, trust and comfort.

The current work offers a method for parametrizing an ADAS controller with the help of test drives with non-professional drivers. The proposed method is validated by the parametrization of an *Adaptive Cruise Control* (ACC) system, which supports the driver by keeping a desired vehicle speed or defined distance to a proceeding slower moving vehicle, the *Object to Follow* (OTF). For the selection of the OTF, the prediction of the future path of the own vehicle (*ego vehicle*) is an essential part of the ACC system. Today, different algorithms are implemented for path prediction.

To evaluate these algorithms, test drives were carried out with a specially equipped vehicle with non-professional test drivers. Based on the measured data, different methods for path prediction were compared. A novel steering prediction algorithm was developed, which is used in combination with a linear *Single-Track Model* (STM) to predict the ego vehicle's path. Based on the predicted ego vehicle path, the OTF is selected, which is then used to parametrize a novel ACC controller. The performance of the controller fulfils previously defined safety and comfort requirements, as well as string stability. Simulations with the recorded OTF data as input were carried out, which showed that the ACC controller is able to simulate the behaviour of the human driver. Furthermore, the controller cuts acceleration peaks, which leads to a more comfortable feeling than with the measurements obtained when the human drove the vehicle. Finally, a comparison with measurements of a state-of-the-art ACC system showed similar behaviour compared to the production controller in following another vehicle.

The results of the present study show that the proposed method is able to identify an appropriate set of parameters for an ACC controller. The idea of parametrizing the controllers with the help of human test driver should lead to a human-like behaviour and increase customer acceptance of the system. Additionally, this optimized parametrization method will help to shorten the development and validation process, which is very important for saving costs.

Kurzfassung

Fahrerassistenzsysteme (FAS) unterstützen den Fahrer durch die Übernahme von Tätigkeiten in der Erfüllung der Transportaufgabe und ermöglichen dadurch sicheres und komfortables Fahren. Die steigende Marktdurchdringung in Kombination mit der großen Anzahl von Fahrzeugmodellen und -typen verlangt eine kosten- und zeiteffiziente Integration und Parametrierung solcher Systeme. Für die Qualität eines FAS ist die Kundenzufriedenheit in Hinblick auf Sicherheit, Zuverlässigkeit, Vertrauen und Komfort ein wichtiges Kriterium.

Die vorliegende Arbeit zeigt eine Methode zur Parametrierung von FAS mithilfe von nicht professionellen Testfahrern auf. Die Methode wird anhand der Parametrierung eines *Abstandregeltempomaten* (ACC) validiert, der den Fahrer bei der Längsführung des Fahrzeugs unterstützt, indem er eine gewünschte Geschwindigkeit oder einen eingestellten Abstand zu vorausfahrenden *Zielfahrzeugen* (OTF) hält. Für die Auswahl des OTF ist die Vorhersage des eigenen Fahrschlauchs ein essentieller Teil. Hierfür werden verschiedene Algorithmen verwendet.

Für die Bewertung dieser Algorithmen wurden Testfahrten mit speziell ausgerüsteten Fahrzeugen durchgeführt. Mit den gemessenen Daten werden die verschiedenen Algorithmen verglichen. In Kombination mit dem linearen *Einspurmodell* (ESM) zeigt ein neu entwickelter Lenkwinkel-Vorhersagealgorithmus die besten Ergebnisse. Basierend auf dem prädizierten Fahrschlauch wird das OTF ausgewählt, mit dessen Hilfe ein neuer ACC-Regler parametriert wird. Dieser kann die gestellten Sicherheits- und Komfortanforderungen, sowie String-Stabilität erfüllen. Simulationen zeigen, dass der Regler das gemessene menschliche Folgeverhalten nachahmen kann und zusätzlich Beschleunigungsspitzen glättet, was eine Steigerung des Fahrkomforts bedeutet. Ein Vergleich mit Messungen eines dem Stand der Technik entsprechenden Fahrzeugs zeigt, dass dessen Folgeverhalten dem des neuen Reglers ähnelt.

Die Ergebnisse der vorliegenden Arbeit zeigen, dass die vorgeschlagene Methode zur Parametrierung von FAS verwendet werden kann. Die Idee der Parametrierung durch Testfahrten mit nicht professionellen Testfahrern führt zu einer Fahrzeugführung durch das Systems, die der des Menschen ähnelt, was zu einer Steigerung der Kundenakzeptanz führen soll. Zusätzlich kann durch die Optimierung der Reglerparametrierung der Entwicklungs- und Validierungsprozess verkürzt werden, was auch eine Kostenreduktion mit sich bringt.

Contents

Contents

Abbreviations

ACC	Adaptive Cruise Control
ACC-SCU	ACC-Sensor and Controller Unit
ADAS	Advanced Driver Assistance System
ADMA	Automotive Dynamic Motion Analyser
AEB	Automatic Emergency Brake
BASt	Bundesanstalt für Straßenwesen
BSM	Blind-Spot Monitoring
CC	Cruise Control
CG	Center of Gravity
CTG	Continuous Time Gap
DIN	Deutsches Institut für Normung
DOF	Degree of Freedom
DVM	Driver-Vigilance Monitoring
ECU	Electronic Controller Unit
ESC	Electronic Stability Control
Euro-NCAP	European New Car Assessment Program
FCW	Forward Collision Warning
FMCW	Frequency-Modulated Continuous Wave
FOV	Field of View
FSK	Frequency Shift Keying
FSRA	Stop-and-Go Adaptive Cruise Control
GNSS	Global Navigation Satellite System
GPS	Global Positioning System
GSM	Global System for Mobile Communications
HIL	Hardware-in-the-Loop
HMI	Human-Machine Interface
ICR	Instantaneous Centre of Rotation
IIHS	Insurance Institute for Highway Safety
ISO	International Organization for Standardization
LDW	Lane-Departure Warning
LIDAR	Light Detection and Ranging
LKA	Lane-Keeping Assistant

LKS	Lane-Keeping Support
LSF	Low-Speed Following
MIL	Model-in-the-Loop
MPC	Model Predictive Control
NS	Navigation System
NHTSA	National Highway Traffic Safety Administration
OTF	Object to Follow
PA	Parking Assistant
PI	Proportional-Integral Controller
PID	Proportional-Integral-Derivative Controller
PIS	Perception Improvement Systems
RADAR	Radio Detection and Ranging
RTK	Real-Time Kinematic
SAE	Society of Automotive Engineers
SMC	Sliding Mode Control
STM	Single-Track Model
TOF	Time of Flight
TTC	Time to Collision
US-NCAP	United States New Car Assessment Program
V2I	Vehicle-to-Infrastructure Communication
V2V	Vehicle-to-Vehicle Communication
WLAN	Wireless Local Area Network

Symbols

In this work, variables and parameters are noted using

$$_1^4X_2^3,$$

where the symbol could be a scalar x, a vector $\mathbf{x}$ or a maxrix $\mathbf{X}$. The indices describe

1. the coordinate system in which the quantity is defined,

2. the index describing the instance,

3. the exponent or the transposition operator $^\mathrm{T}$ for vectors and matrices and

4. the iteration step or the point of application, which is in the origin of the coordinate system, if it is not given.

Coordinate Systems

$(_0x, {}_0y, {}_0z)$	The *global coordinate system* has its origin on the ground plane, and the $_0z$-axis is perpendicular to it.
$(_vx, {}_vy, {}_vz)$	The *vehicle coordinate system* has its origin in the vehicle CG, the $_vx$-axis is along the longitudinal direction of the vehicle body, and the $_vy$-axis is along the lateral direction of the body.
$(_\beta x, {}_\beta y, {}_\beta z)$	The *beta coordinate system* has its origin at vehicle CG, the $_\beta x$-axis is in the direction of the speed vector, and the $_\beta z$-axis is parallel to the $_0z$-axis.
$(_sx, {}_sy, {}_sz)$	The *sensor coordinate system* is described in the context used.
$(_wx, {}_wy, {}_wz)$	The *wheel coordinate system* has its origin in the W-point, and the $_wz$-axis is parallel to the $_0z$-axis. The $_wx$ and $_wy$-axes are the projections of the $_cx$ and $_cy$-axes along the $_wz$ direction onto the ground plane. The additional indices fl, fr, rr and rl describe the position of the wheels on the vehicle, which are described below.
$(_cx, {}_cy, {}_cz)$	The *wheel centre coordinate system* has its origin in the C-point, the $_cy$-axis is in the direction of the rotation axis of the wheel, and the $_cx$-axis is parallel to the ground plane. It uses the same additional indices for the position of the wheels mounted on the vehicle as the wheel coordinate system.
(s, u)	The *natural path coordinate system* measures s along the trajectory of the CG and u perpendicular (mathematical positive rotation angle around $_0z$-axis) to it. The origin is the vehicle CG.

Parameters and Variables

a	acceleration
A	amplitude, area
b	track width, path width
c	stiffness, speed of light
d	distance
e	error
f	frequency
F	force
g	acceleration of gravity
i	transmission ratio, imaginary unit
is	iteration step
k	controller gain
I	moment of inertia
J	cost function
l	length
L	length
m	mass
n	number
N	number
p	pressure, probability
P	priority, parameter, power
q	quartile, parameter
r	distance, radius
R	radius
s	coordinate in path direction, slip, sliding surface
t	time
T	torque, periodic time, sampling time
TTC	Time to Collision
u	coordinate perpendicular to path, plant input
v	speed
w	width, weight
α	tyre side slip angle, reflection parameter
β	vehicle side slip angle, inclination angle, expansion parameter
γ	contraction parameter
δ	steering angle
ε	error angle
η	efficiency
κ	curvature
λ	eigenvalue, wave length
μ	membership function

ρ	phase angle
σ	standard deviation
τ	time gap, propagation time
φ	azimuth angle
ψ	heading angle
ω	rotational speed

Vectors and Matrices

0	zero matrix
A	system matrix
b	input vector
c	output vector
C	output matrix
e	error-state vector
F	system matrix at MPC
I	identity matrix
L	observer gain
n	normal vector
p	direction vector, position vector
R	weight matrix
s	position vector
T	coordinate system transformation matrix
U	plant input vector at MPC
v	speed vector
x	state vector
y	output quantity
Y	output quantity at MPC
Φ	input vector at MPC

Indices

0	initial condition
∞	infinity
a	air drag
AW	anti-windup
b	brake, best
B	vehicle body
c	controlled
CG	centre of gravity
d	drive train

des	desired value
D	derivative term
DR	Doppler RADAR
e	engine
ex	exist
f	front
fl	front left
FOV	Field of View
fr	front right
FSK	Frequency Shift Keying RADAR
g	gear box
i	object number, prediction number
ib	in-between
is	iteration step
I	integral term
j	prediction number
k	time step
l	left, lower
long	longitudinal
max	maximum
min	minimum
nom	nominal
OTF	Object to Follow
p	predicted
P	proportional term
r	rear, right, rolling
rl	rear left
rr	rear right
set	set value
SMC	Sliding Mode Control
SW	steering wheel
T	target
u	upper
veh	vehicle
w	wheel, worst
x	x-direction
y	y-direction
z	z-direction
β	climbing resistance

1
Introduction

The term *Advanced Driver Assistance System* (ADAS) describes systems in a vehicle that support the drivers in their driving task. Donges shows in [Don99] that the driving task itself can be divided into the three levels

- *navigation,*
- *guidance* and
- *stabilization.*

For each driving task, special ADAS are available to support the driver. For example, a *Navigation System* (NS) supports the driver on the level of navigation, an *Adaptive Cruise Control* (ACC) on the level of guidance, and the *Electronic Stability Control* (ESC) on the level of stabilization. Chapter 2 describes these three levels in more detail, and appendix A provides additional descriptions of available ADAS.

Driver support can be accomplished via

- optical, acoustical or haptic *warnings* and/or
- driver-initiated or automatic *interventions* of the ADAS.

A *Lane-Departure Warning* (LDW) is a warning system that informs drivers that they are about to leave the lane unintentionally. In contrast, a *Lane-Keeping Assistant* (LKA) helps drivers hold the vehicle in its lane by applying interventions on the vehicle.

Another way to categorize ADAS is to distinguish between

- *comfort-oriented* and
- *safety-oriented* systems.

The main function of comfort-oriented ADAS is to assist drivers by taking over driving tasks. In the vehicle's longitudinal direction, ACC systems support the driver, while LKA systems provide support in the lateral direction. An *Automatic Emergency Brake* (AEB) is a safety-oriented system that should prevent collisions between vehicles.

ADAS cannot be assigned exclusively to one of the categories described above. As mentioned above, an ACC is a comfort-oriented system. Eichberger demonstrated in [Eic11], that ACC also increases the safety using an in-depth accident analysis of 217 (statistically corrected 260) fatal accidents from the database ZEDATU for the year 2003. This research showed that an ACC would have prevented eight accidents and would have reduced the severity of another eight accidents, representing about six percent of the total accidents. In comparison, an AEB, which is a safety-oriented system has a potential of about 21 percent. This example shows why systems cannot be classified clearly.

In the year 2010, the European Commission set the goal to halve the yearly 31 508 road fatalities by the year 2020, [Off11]. In the same document, they stipulated that one of the main actions to be taken to reach this goal is to deploy ADAS. Figure 1.1 shows the fatalities in the 28 European countries from the year 1991 until 2013. Using a regression line, from the data of the last four years, the predicted fatalities in the year 2020 would be 12 511, thereby reaching the set goal.

In the United States of America, the *National Highway Traffic Safety Administration* (NHTSA) is also working on ADAS. They also determined that these systems will reduce the severity of accidents [GFB13].

These initiatives show why the number of vehicles equipped with ADAS will increase in the future. A few years ago, they were only available in luxury class vehicles. Today they are available in all segments, even in lower ones.

The trend of the recent years toward automated driving has led to standards for categorizing the level of automation. Table 1.1 provides an excerpt of standard [Soc14], which shows a comparison between the *Society of Automotive Engineers* (SAE) levels of automation and those of the *Bundesanstalt für Straßenwesen* (BASt).

In both cases, the list starts at full manual driving by the human, *SAE level 0*, which already includes warning systems.

SAE level 1 is the commonly known ADAS, where the system performs the longitudinal *or* lateral control of the vehicle. These functions are available in some driving modes, while the human drivers are responsible for monitoring the environment and are the fallback in dynamic driving tasks. Examples include ACC and *Lane-Keeping Support* (LKS) systems. See appendices A.1 and A.3 for short descriptions of these systems.

SAE level 2 systems control longitudinal *and* lateral movement of the vehicle. However, the human driver has to monitor the system and is the fallback solution in dynamic driving events. *Low-Speed Following* (LSF) systems are an example of such a technology that is already available on the market, appendix A.4.
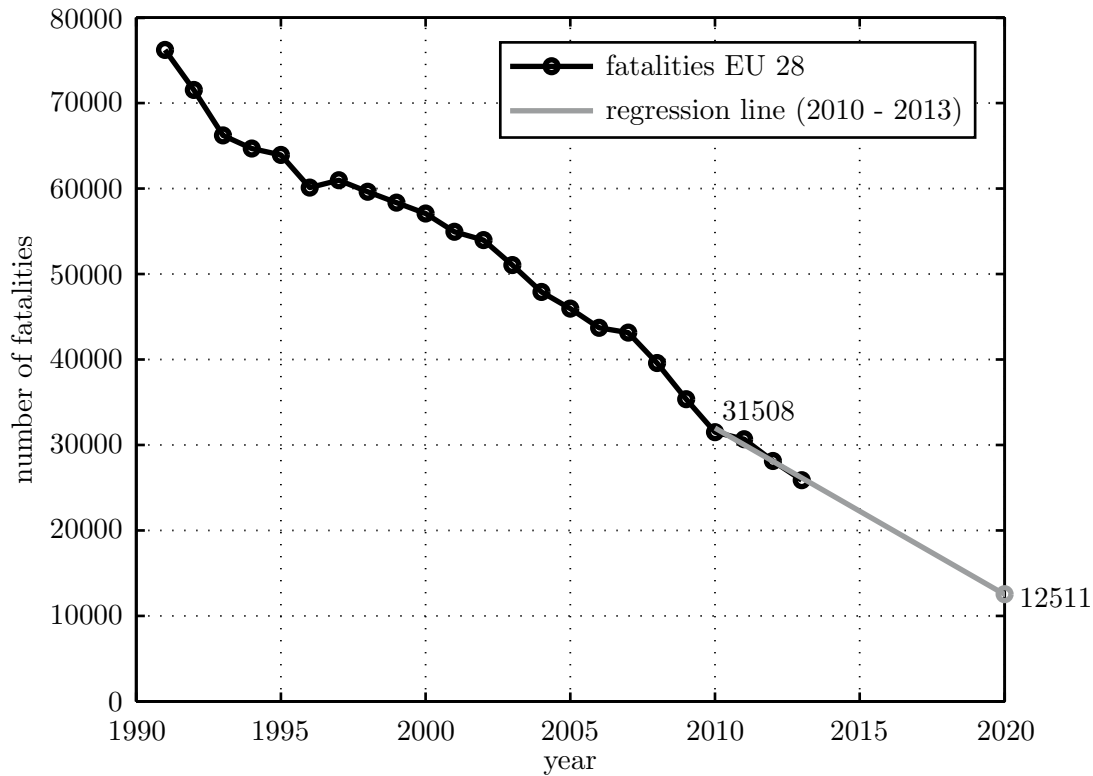
Figure 1.1.: Fatalities from 1991 until 2013 and forecast for 2020 for the EU 28, adapted from [Eur14a]

From *SAE level 3* upwards, the system itself is responsible for monitoring the environment. This involves very high requirements for the environmental-recognition sensors. The human driver is still the fallback solution in dynamic situations. In Europe, this level is not permitted. According to the *Convention on Road Traffic*, drivers must control their vehicle at all times, see chapter 1.1.1. Giesler et al. showed that it takes an average of 2.7 s to bring a distracted driver back into the loop, with a maximum time of 8.8 s [GT13]. This means that the system has to know about 10 s in advance when the driver has to takeover the control of the vehicle, which is one of the challenging topics in the research dealing with highly automated vehicles.

SAE level 4 is more or less the same as SAE level 3, with the difference that the human driver is no longer the fallback for dynamic driving tasks. The system has to handle such situations by itself.

The fully automated vehicle is just defined in the SAE levels; there is no corresponding BASt level available. Since *SAE level 5* systems do not need a human driver, the system has to be able to drive in all situations.

Today, systems up to SAE level 2 are available in production vehicles. Much research is focused on higher levels of automation, but such technologies are currently only available in simulations or as prototypes, which may change in the coming years.

1.1. Regulatory Framework

The Regulatory Framework for ADAS can be divided into different levels, which are explained in the following sections.

1.1.1. International Treaties

The goal of international treaties is to harmonize national legislations. Therefore, the *Convention on Road Traffic* was introduced in the year 1968 to define such factors as standard driving rules, the type approval for the vehicles and driver requirements [Eco68]. This treaty was ratified by nearly all European countries and in numerous countries worldwide, which pledged to adopt the contents in their national laws.

Paragraph five of article eight states:

> *Every driver shall at all time be able to control his vehicle or to guide his animals.*

The first paragraph in Article 13 states:

> *Every driver of a vehicle shall in all circumstances have his vehicle under control so as to be able to exercise due and proper care and to be at all times in a position to perform all manoeuvres required of him. [...]*

From these formulations, it could be inferred that only ADAS that can be overruled by the driver are allowed. However, this interpretation is incompatible with the goal of introducing more highly automated vehicles. Therefore, the changes of the Convention were drafted in [Eco14]. The following addition, paragraph 5bis, should be made to article eight:

> *Vehicle systems which influence the way vehicles are driven shall be deemed to be in conformity with paragraph 5 of this Article and with paragraph 1 of Article 13, when they are in conformity with the conditions of construction, fitting and utilization according to international legal instruments concerning wheeled vehicles, equipment and parts which can be fitted and/or be used on wheeled vehicles.*

> *Vehicle systems which influence the way vehicles are driven and are not in conformity with the aforementioned conditions of construction, fitting and utilization, shall be deemed to be in conformity with paragraph 5 of this Article and with paragraph 1 of Article 13, when such systems can be overridden or switched off by the driver.*

Table 1.1.: Levels of automation, excerpt of SAE standard [Soc14]

SAE level	BASt level	SAE definition	Long. and lat. control	Monitoring of environment	Fallback dynamic driving tasks	Modes
0	Driver only	Full-time performance by the human driver	Human driver	Human driver	Human driver	n/a
1	Assisted	Mode-specific execution of either long. or lat. control by system	Human driver and system	Human driver	Human driver	Some modes
2	Partially automated	Mode-specific execution by one or more driver assistance systems of both long. and lateral control	System	Human driver	Human driver	Some modes
3	Highly automated	Mode-specific performance by an automated driving system of all aspects of the dynamic driving task with the expectation that the human driver will respond appropriately to a request to intervene	System	System	Human driver	Some modes
4	Fully automated	Mode-specific performance by an automated driving system of all aspects of the dynamic driving task, even if the driver does not respond appropriately to a request to intervene	System	System	System	Some modes
5	-	Full-time performance by an automated driving system under all possible driving modes	System	System	System	All modes

These changes should form the legal basis for more highly automated vehicles. With the added paragraph, systems are allowed if the driver can overrule the system or switch it off.

1.1.2. National Laws and Type Approval

For the type approval, vehicles have to fulfil regulations, such as the the *ECE Regulations* in Europe. For ESC, a special test procedure is described in Annex nine of [Eco11]. The same procedure can be found in United States Law [Nat13b]. In Europe, for the braking function of an ACC or AEB, the system has to conform with the requirements in annex eight of ECE-R 13-H, [Eco11], which only defines the requirements for the design process of complex electronic vehicle control systems. No limits are given for physical quantities, e.g. acceleration.

1.1.3. Standards and Consumer Testing

Although the requirements derived from standards and consumer testing are not mandatory, they are still important for vehicle manufacturers. Standards describe the state-of-the-art and are available for most ADAS. For ACC systems, the *International Organization for Standardization* (ISO) and the SAE have defined standards [Tec10], [Tec09] and [SAE03]. There, ACC systems are divided into different classes, depending on the performance of the environmental-recognition sensor(s).

In Europe, the *European New Car Assessment Program* (Euro-NCAP) includes certain ADAS in its assessment, including Seat Belt Reminders, Speed Assist Systems, AEB and Lane Support Systems, [Eur12, Eur13]. Since the Euro-NCAP evaluation is an important selling point, car manufacturers are forced to introduce these safety systems in their new vehicles. In [Eur14b], Euro-NCAP announced that more complex tests would be defined in the coming years, since they expect a better system performance due to the extensive research by the car manufacturers.

In North America the *Insurance Institute for Highway Safety* (IIHS) set up standard tests for AEB systems, [Ins13]. The *United States New Car Assessment Program* (US-NCAP) evaluates ESC [Ins13], LDW and LKS [Nat13c], *Forward Collision Warning* (FCW) [Nat13a] and AEB [Nat12].

The boundary conditions described in chapters 1.1.1 to 1.1.3 provide only a very rough idea of how to design ADAS. Nevertheless, they have to be fulfilled to ensure conformity with laws and type approval. However, the performance of the ADAS depends on the strategy of the car manufacturer and the design and validation engineers of the system.

1.2. Goal and Structure of this Work

The present work focuses on the parametrization process of ADAS. It proposes a method for parametrizing an ADAS with the help of real-world test drives with non-professional drivers. The suggested method is validated by applying it to determine the controller parameters for an ACC controller. The hypothesis behind this research is that ACC systems parametrized by human behaviour will be better accepted, and this process will therefore provide a valuable tool for vehicle development.

Chapter 2 provides an overview of the required components of an ACC system, which focuses on the environmental-recognition sensors and offers examples of different upper level controllers of the ACC that are mentioned in literature.

Chapter 3 introduces the commonly used development process for ADAS. It shows the trade-off between shortening the development time for ADAS and delivering a system that satisfies the customer.

Chapter 4 describes measurements obtained with a specially equipped vehicle. A very complicated measurement setup was used to synchronously measure the movement of two vehicles during the tests. In addition, a production *Radio Detection and Ranging* (RADAR) sensor delivers the data received by an ACC system in an ACC vehicle.

Based on these measurements, *chapter 5* describes the selection of the *Object to Follow* (OTF). To this end, algorithms from literature and a new algorithm are applied to the measured data, and the output is validated.

Chapter 6 introduces a new non-linear ACC controller. The data measured for the OTF was used to parametrize this controller, and the identified parameters were verified via simulations. The output of the simulations indicates the high potential of the proposed method and the novel ACC controller.

Chapter 7 summarizes the key findings by chapter and provides a final statement.

2

Adaptive Cruise Control

The *Traffic System* describes the interactions between the vehicle, driver and environment. Figure 2.1 illustrates the signal flow between the components involved, focusing on *Advanced Driver Assistance System* (ADAS). The driver applies his/her longitudinal (gas and brake) and lateral (steering) inputs to the vehicle. Additional inputs for the vehicle include traffic and disturbances from the environment. As described by Donges in [Don99], the human operation can be divided into three different levels that accomplish the transport task: navigation, course guidance and stabilization. Each of these three levels has a corresponding area of human behaviours. Human behaviour consists of knowledge-based, rules-based and skill-based behaviour. According to [Don99], these behaviours cannot be directly connected to one human operation.

The output of navigation is the selection of the right route to accomplish the transport task (e. g. select the motorway to reach the desired destination). The desired trajectory is selected by the course guidance (e. g. drive at 120 km/h and change the lane to overtake a truck). The stabilization of the vehicle is an automatic response to stimuli (e. g. stabilization of the vehicle while over-steering through steering input). All of these three levels are based on the human perception of the environment and the vehicle. The information transfer from the vehicle to the driver happens through haptic perception (through the seat and the steering wheel) and optic and acoustic signals via the *Human-Machine Interface* (HMI).

The ADAS controller receives signals from the vehicle dynamic sensors, the environmental-recognition sensors, the HMI and the ADAS actuators. Based on this information, the ADAS controller operates the actuators to control the movement of the vehicle. Some of the environmental sensors need information about the current driving state, which is sent via the ADAS controller.
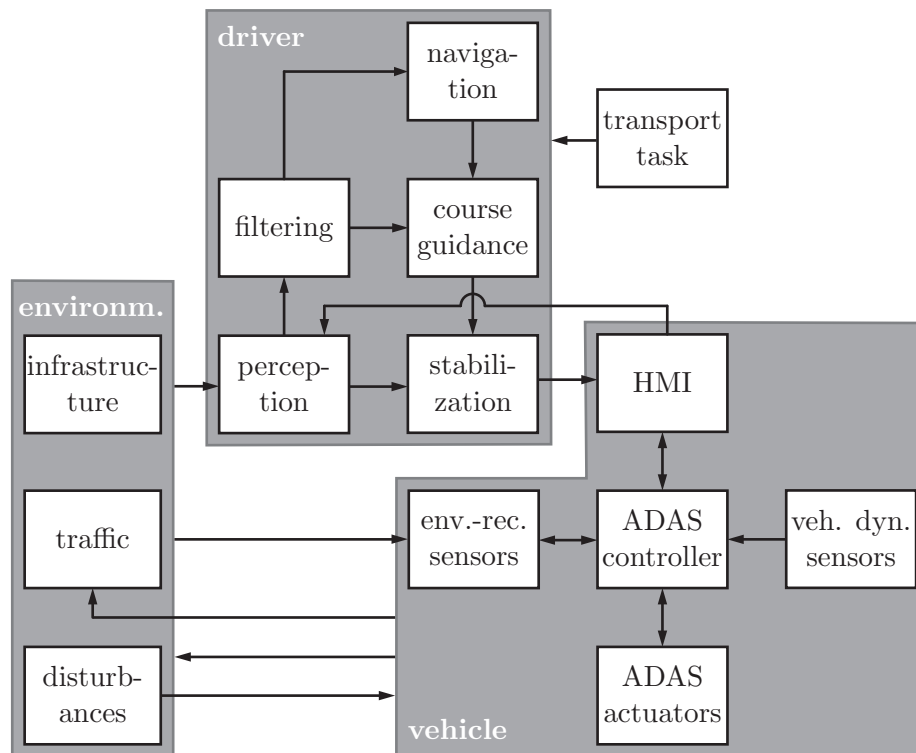
Figure 2.1.: Traffic System, adapted from [Don09]

The following chapters describe the most important components for *Adaptive Cruise Control* (ACC) systems in detail.

2.1. Human Machine Interface

The HMI is the connection between the driver and the vehicle. For ACC systems, the driver feeds the desired cruising speed and desired time gap into the system, and the HMI displays the actual speed and distances to the *Object to Follow* (OTF), if present. Additionally, if the ACC system cannot handle the current situation, warnings are displayed to transfer the longitudinal control back to the driver [Rob04] and [WDS09].

In production ACC vehicles, a common range for the desired driving speed is 20 to 200 km/h. The desired time gap can be selected in the range of 1 to 2.2 s, which is recommended in *International Organization for Standardization* (ISO) standard 22179, [Tec09]. It is important that the control of an ADAS does not distract the driver, [Rob04].
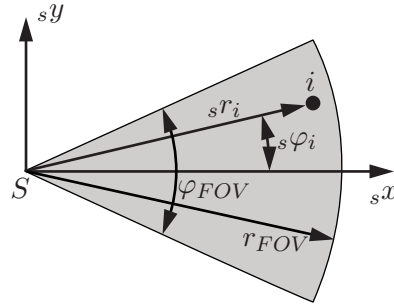
Figure 2.2.: Sensor quantities for object i, including FOV of the sensor

2.2. Environmental-Recognition Sensors

For ACC systems, environmental-recognition sensors measure the position of object i, described by the polar coordinates $_sr_i$ and $_s\varphi_i$ and in some cases, speed $_s\dot{r}_i$ and $_s\dot{\varphi}_i$ as well in the sensor coordinate system, see fig. 2.2. If speed is not measured directly, it is calculated in the data processing. In addition, fig. 2.2 depicts the *Field of View* (FOV) of the sensor bounded by r_{FOV} and φ_{FOV}, representing the area where the sensor can detect an object. The following sections describe various sensors that are available.

2.2.1. RADAR Sensor

Production ACC systems use at least one *Radio Detection and Ranging* (RADAR) sensor. The automotive RADAR sensor emits electromagnetic bundled waves, which are reflected by objects. They are available at frequency bands of 24 to 24.5 GHz, 76 to 77 GHz and 77 to 81 GHz, [Win09]. For automotive applications, different types of RADAR sensors with different measurement principles are available, which are described in the following sections.

Pulsed Doppler RADAR

The *Pulsed Doppler RADAR* is the simplest RADAR sensor for automotive application. It emits a pulse of a certain length, which is reflected by the object and received by the sensor, see fig. 2.3. The relationship

$$r = \frac{c\,\tau}{2} \tag{2.1}$$

describes how the distance r can be calculated using the signal propagation time τ and the speed of light c. The Doppler Effect is used to determine the relative velocity $\dot{r}$. Assuming small velocities ($\dot{r} \ll c$), the frequency shift reads

$$\Delta f_{\dot{r}} = -f_0 \frac{2\dot{r}}{c}, \tag{2.2}$$
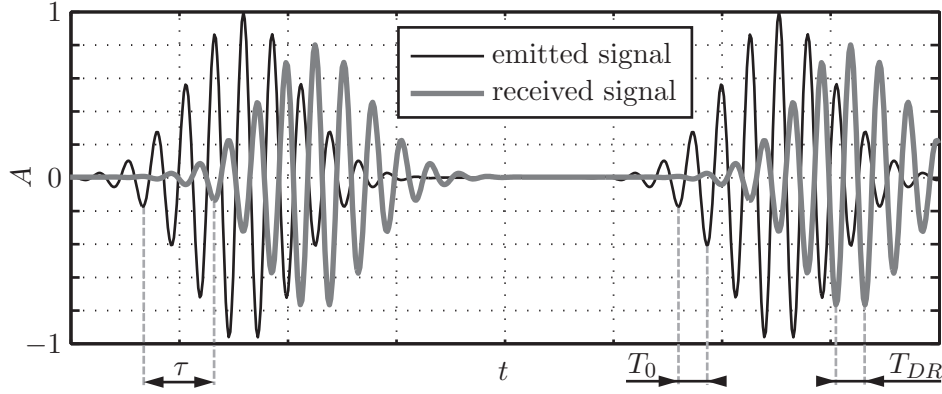
Figure 2.3.: Emitted and received pulses of a Pulsed Doppler RADAR, adapted from [Men99]

where $f_0 = \frac{1}{T_0}$ is the emitted carrier frequency of the RADAR sensor, [Men99]. The received signal has a frequency of $f_{DR} = f_0 + \Delta f_{\dot{r}}$, where $f_{DR} = \frac{1}{T_{DR}}$, see fig. 2.3.

FMCW RADAR

In contrast to the Pulsed Doppler RADAR, the *Frequency-Modulated Continuous Wave* (FMCW) RADAR sends and receives continuous electromagnetic waves. Using the rule

$$f(t) = f_1 + \frac{f_2 - f_1}{T} t, \tag{2.3}$$

the sending frequency $f(t)$ is modulated with linear ramps of the length T between f_1 and f_2. Figure 2.4 shows an example for three frequency ramps emitted by an FMCW RADAR sensor. The finite speed of propagation of RADAR waves, described in eq. (2.1), causes a frequency shift between the emitted and received signals of

$$\Delta f_r = f_1 - f(t) = -\frac{f_2 - f_1}{T} \frac{2r}{c}. \tag{2.4}$$

This effect is superimposed by the Doppler Effect of eq. (2.2). Therefore, the equation of the measured frequency difference between emitting and receiving signals of an object at distance r with the relative velocity $\dot{r}$ reads

$$\Delta f = -\frac{f_2 - f_1}{T} \frac{2r}{c} - f_0 \frac{2\dot{r}}{c}. \tag{2.5}$$

The detection of a single object requires two different ramps, while a third ramp must be added in order to detect more than one object. The graphical representation of the problem can be performed in the r-$\dot{r}$ plane, [Men99]. The solution for the distance and the relative velocity is at the point of the intersection of the different ramps. Figure 2.5 shows an example of a situation with three different ramps and four objects.
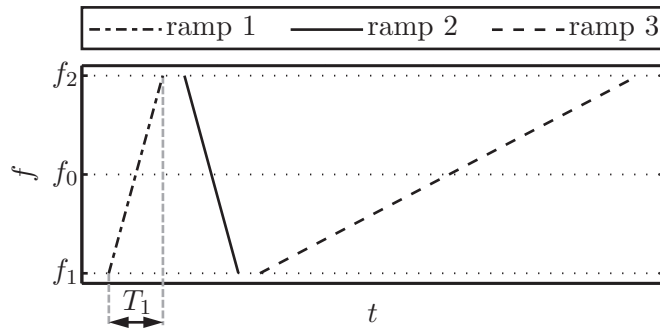
Figure 2.4.: Three generic frequency signals $f(t)$, according to eq. (2.3), adapted from [Win09]
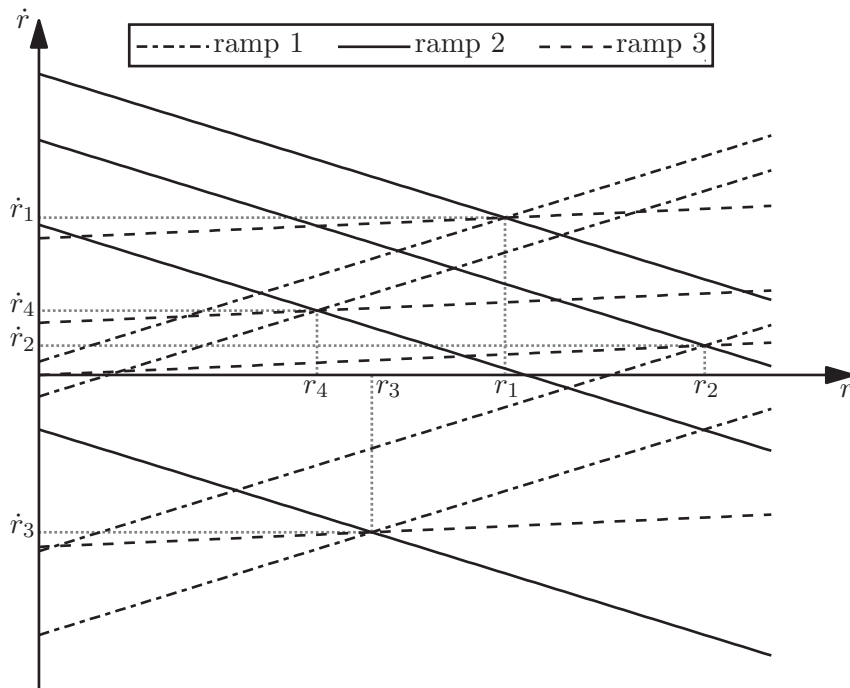
Figure 2.5.: Generic r-$\dot{r}$ plane for FMCW RADAR, adapted from [Win09]
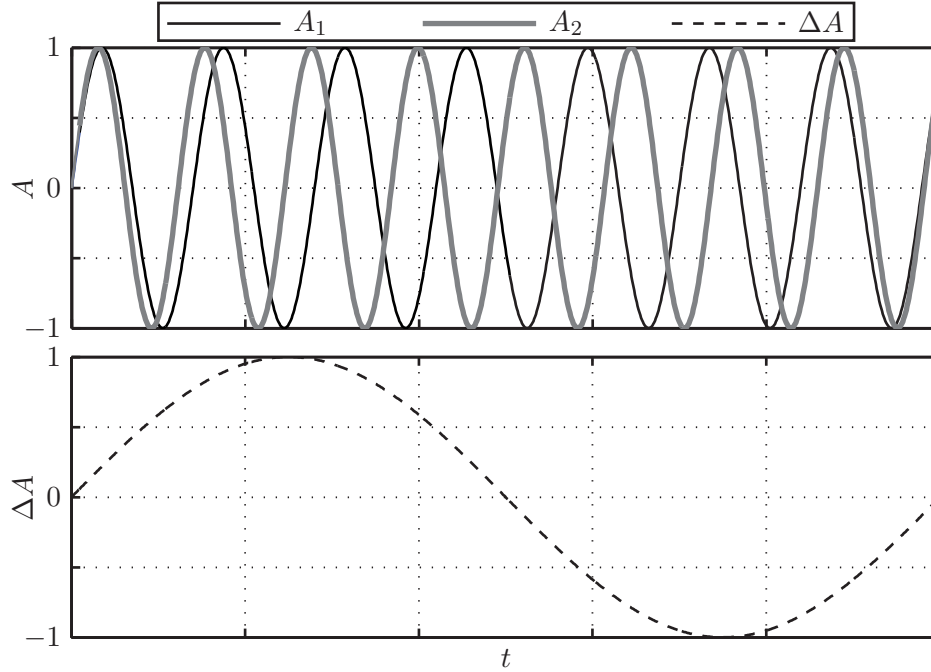
Figure 2.6.: Distance measurement through phase comparison, adapted from [Men99]

FSK RADAR

The *Frequency Shift Keying* (FSK) RADAR sends electromagnetic waves alternating between two constant frequencies $f_{1,2} = f_0 \pm \frac{\Delta f_{FSK}}{2}$. The normalized signals read $A_{1,2} = \sin(2\pi f_{1,2} t)$, see fig. 2.6. The RADAR sensor measures the phase angles $\rho_{1,2}$ of the two signals received and then calculates the phase difference

$$\rho_2 - \rho_1 = 2\pi(f_2 - f_1)\, \tau, \tag{2.6}$$

with the corresponding normalized amplitude $\Delta A = \sin(\rho_2 - \rho_1)$, as depicted in fig. 2.6. Using eq. (2.1), the phase difference of eq. (2.6) is rearranged to

$$\rho_2 - \rho_1 = \frac{4\pi}{c}(f_2 - f_1)\, r, \tag{2.7}$$

where the distance to the object r can be found. Due to the fact that $\Delta f_{FSK} \ll f_0$, the relative speed can be calculated using the frequency shift of the Doppler Effect $(\Delta f_{\dot{r}})$, as described in eq. (2.2).

Chirp Sequence Modulation RADAR

The *Chirp Sequence Modulation RADAR* combines the advantages of the RADAR sensor types mentioned above, [Win09]. It sends a high number of identical frequency ramps,
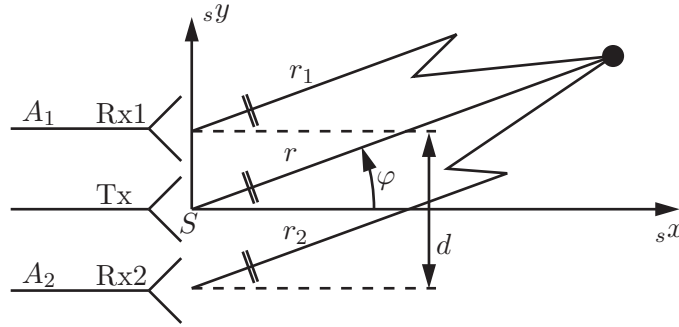
Figure 2.7.: Monopulse priciple, adapted from [Win09]

as described in eq. (2.3). When sending at frequency $f(t)$, it receives the frequency $f(t) - \Delta f_r$. At this measurement at time t, the frequency shift due to the Doppler Effect is omitted because it is much smaller than the change of the frequency due to the chirp. Using this frequency shift and eq. (2.4), the distance to the object can be calculated. The relative velocity is determined with the frequency shift due to the Doppler Effect, which is not determined at a single measurement point, but rather over a longer period of frequency ramps. Therefore, eq. (2.2) with $f_0 = f_1$ is used to find the relative speed $\dot{r}$, [Win09].

Monopulse RADAR

The *Monopulse Method* is used to find the azimuth angle φ, see fig. 2.2. The method is called monopulse because only one RADAR impulse, which is emitted by antenna Tx1, is necessary to detect the angle. The two antennas Rx1 and Rx2 receive phase-shifted signals. They have a horizontal distance of d in the $_sy$ direction of the sensor coordinate system, see fig. 2.7. Signal processing generates the sum $|\sum|$ and the difference $|\Delta|$ of the two signals. Figure 2.8(a) shows the normalized signals A_1 (solid) and A_2 (dashed) for the received signals of two different azimuth angles (black and grey). The error angle ε depicted in fig. 2.8(b) reads

$$\varepsilon = \frac{|\Delta|}{|\sum|} = \frac{|A_1| - |A_2|}{|A_1| + |A_2|}. \tag{2.8}$$

The gradient of ε is a measure for the azimuth angle φ, [Mah88].

Mahafza describes in [Mah88] another possibility to estimate the azimuth angle by measuring the phase shift between the two signals. Signal A_2 can be described as $A_2 = A_1\, e^{-i\,\Delta\delta}$, where $\Delta\delta$ describes the phase shift between the two signals. The modulus of the quotient of the difference $\Delta = A_1 - A_2$ and the sum $\sum = A_1 + A_2$ reads

$$\left|\frac{\Delta}{\sum}\right| = \tan\left(\frac{\Delta\delta}{2}\right). \tag{2.9}$$
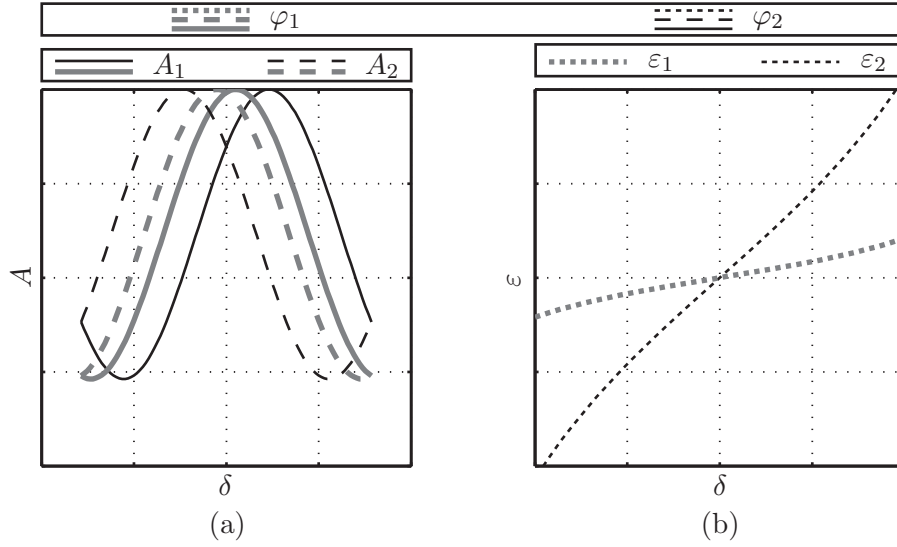
Figure 2.8.: (a) Signals received by Tx1 and Tx2 and (b) error signal of eq. (2.8), (a) and (b) for $\varphi_1 < \varphi_2$, both adapted from [Mah88]

Assuming that $d \ll r$ (fig. 2.7), the difference between the two signals reads $r_2 - r_1 = d\,\sin(\varphi)$. This difference in length results in a phase shift $\Delta\delta = \frac{2\pi\,d}{\lambda}\sin(\varphi)$ of the received signals. Using this expression and eq. (2.9), the azimuth angle can be calculated by

$$\varphi = \arcsin\left[\frac{\lambda}{\pi\,d}\arctan\left(\left|\frac{\Delta}{\Sigma}\right|\right)\right]. \tag{2.10}$$

Scanning RADAR

Scanning RADAR sensors sweep a narrow RADAR beam over the FOV. Figure 2.9(a) shows an illustration for one object at φ_i. The lower graph shows the received power P for different discrete angles. The maximum of the power is received at azimuth angle φ_i of the object, [Win09]. A mechanical or an electrical mechanism can be used to deflect the RADAR beam.

Multi-Beam RADAR

In *Multi-Beam RADAR* sensors, the device emits a number of fixed beams. Figure 2.9(b) gives an example of a RADAR sensor with two beams, Tx1 and Tx2. Using the received power P of every antenna and the antenna diagram, the azimuth angle φ_i of the object can be found, [Win09].
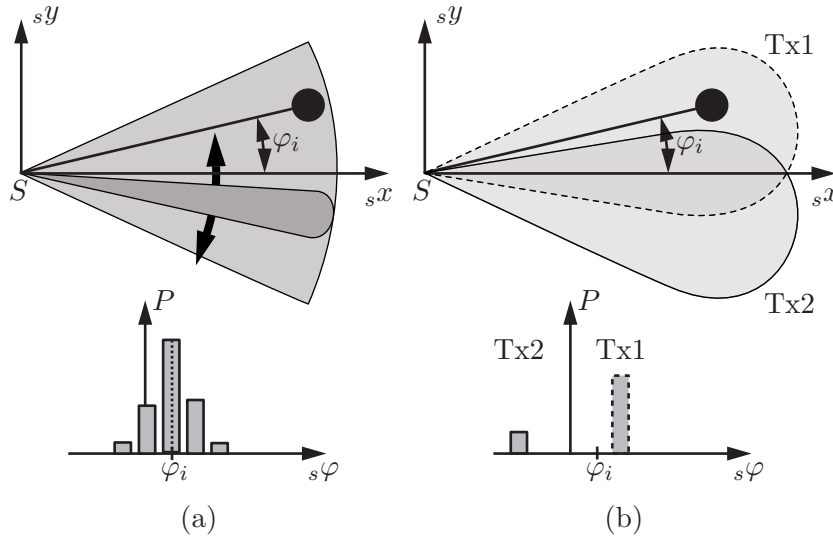
Figure 2.9.: (a) Scanning RADAR and (b) Multi-Beam RADAR, adapted from [Win09]

2.2.2. Video Camera

Common *video cameras* are passive sensors, which are very similar to the human eyes. There are also active cameras, which emit visible or infrared light. If infrared light is used, they are most often used as *Perception Improvement Systems* (PIS), see appendix A.7. *Time of Flight* (TOF) cameras, which emit visible light, are able to detect the depth coordinate for every pixel in the generated picture, [BLR09]. Since active cameras are not used in production ACC systems, they are not described in detail in this work.

Common cameras consist of lenses, the imager and the signal processing unit. The lens bundles the divergent light reflected by the object to convergent light and projects the picture of the object onto the imager, see fig. 2.10(a). The imager discretises the picture and sends the digital image to the signal processing unit, where the features used by the ADAS are extracted. Camera systems can be used to detect lane markings in order to ensure proper target selection or to detect objects to support another sensor(s), most often RADAR sensor(s), in the object classification, [SBD09].

Mono Camera

Stein et al. showed in [SMS03] that it is possible to use a single *mono camera* for ACC systems. Using the height of the camera above ground, the distance to the object can be estimated. In this case the target has to stand on the same planar surface as the ego vehicle that is equipped with the camera. If this is not the case, the non-planarity can be compensated by using lane markings detected by the camera.
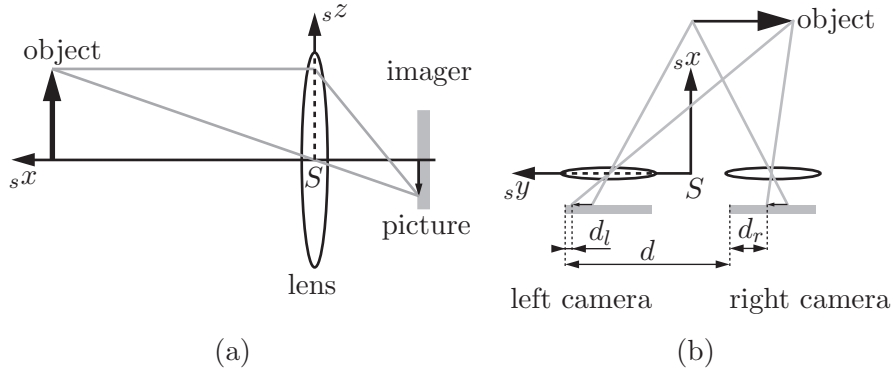
Figure 2.10.: (a) Projection of an object onto the imager and (b) stereo principle, adapted from [SBD09]

Stereo Camera

In *stereo cameras* systems, two cameras are mounted at a defined distance d, see fig. 2.10(b). The picture of one object is not at the same place on the two imagers. There is a lateral offset of $\Delta d = d_l - d_r$, which is called a disparity. So for every pixel on the imager, the depth information $_sx$ can be found because $\Delta d \sim \, _sx$. Using this so-called range map, the feature extraction is performed to find the objects in the picture. Due to the large number of pixels in a picture, this process requires a high computation power, [SBD09]. Stein et al. showed in [SGS10] that it is possible to reduce the required computation power if the order of the signal processing process is changed. In the *Stereo-Assist* approach, they use two mono cameras which perform the feature extraction. Afterwards, the stereo principle is used to find the distance for every object instead of for every pixel, which significantly reduces the number of operations.

2.2.3. LIDAR Sensor

The *Light Detection and Ranging* (LIDAR) sensor is an optical sensor that radiates electromagnetic waves, with a wave length of about 850 to 1000 nm. This is in the area of infrared light on the border to visible light. If too much power is emitted, human eyes will be hurt. Therefore, the impulse has to be very short. For automotive applications, an impulse length of about 30 ns is commonly used. The range measurement is performed as described in eq. (2.1) for the Pulse Doppler RADAR. For LIDAR sensors, it is possible to use the Doppler Effect to measure the relative speed, but it is too expensive for vehicles. Therefore, $\dot{r}$ is estimated with the difference quotient $\dot{r} = \frac{r_2 - r_1}{t_2 - t_1}$, where $r_2 - r_1$ describes the change of the distance between two measurements, and $t_2 - t_1$ describes the time between the measurements. The angle can be measured in different ways. For the fixed multi-beam LIDAR, the sensor emits different beams at fixed position, see fig. 2.11(a). The angular resolution of this type corresponds roughly to the width of the beam. The
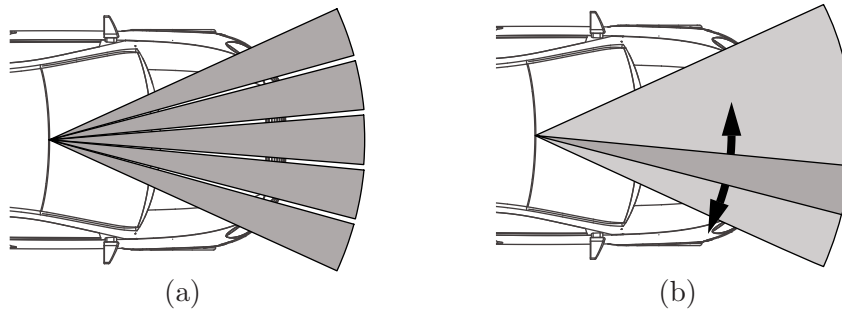
Figure 2.11.: (a) Fixed multi beam LIDAR sensor and (b) Scanning LIDAR sensor, adapted from [Ged09]

scanning LIDAR, which is depicted in fig. 2.11(b), moves the beam across the FOV. This results in a better angular resolution. If the beam does not scan the whole sensor area, but only the area that is of interest for the ADAS, the sensor is called sweeping LIDAR. Combinations of the different principles are also available (e. g. the scanning multi beam LIDAR).

There is a significant difference between the infrared radiation caused by the sun during the night and day, which makes it challenging to ensure correct sensor functionality.

2.2.4. V2X Sensor

V2X is a hypernym for *Vehicle-to-Infrastructure Communication* (V2I) and *Vehicle-to-Vehicle Communication* (V2V), which feature ad-hoc data networks using a special *Wireless Local Area Network* (WLAN) protocol. The advantage of this sensor is that information can be transmitted about actions which will occur in the future (e. g. the intention of a vehicle to change lanes before the lateral movement of the vehicle can be measured by another sensor in the ego vehicle). Bifulco et al. showed in [BPSP11] that a sensor data fusion of V2V data with other sensors smooths the distance measurements and therefore increases the quality of ACC systems.

The use of V2X sensors enlarges the FOV to several hundred meters with 360°, depending on the environment.

2.2.5. Required Field of View

This chapter describes an option to determine the required FOV for defined ACC operation limits. For ACC systems, standards are available that define the lateral and longitudinal acceleration limits. In [Tec10], the limits for ACC systems are described. The main limitations of this standard are the maximum longitudinal deceleration $_v a_{x,min} = -3.5\,\mathrm{m/s^2}$, the minimum speed, which can be set by the driver

Table 2.1.: Simulation input

simulation num.	v_0 [km/h]	δ_f [°]	simulation num.	v_0 [km/h]	δ_f [°]
1	50	2.03	8	120	0.45
2	60	1.45	9	130	0.40
3	70	1.09	10	140	0.36
4	80	0.86	11	150	0.33
5	90	0.71	12	160	0.30
6	100	0.59	13	160	0.00
7	110	0.51			

$v_{set,min} = 7\,\text{m/s}$, and the maximum lateral acceleration $_v a_{y,max} = 2.3\,\text{m/s}^2$. Using this data, simulations with a simplified vehicle dynamics model of eq. (B.17) were conducted. The initial vehicle speed was increased from $v_0 = 50$ to $160\,\text{km/h}$. The target vehicle was driving at $v_T = v_{set,min}$. Using the script of Hirschberg [HW10], the steering angle of the front tyre was calculated by

$$\delta_f = \frac{l_f + l_r}{\frac{v_0^2}{_v a_{y,max}}} + \frac{m\, a_{y,max}}{l_f + l_r} \left(\frac{l_r}{2_f c_y} - \frac{l_f}{2_r c_y} \right) \tag{2.11}$$

and was held constant during each simulation. Thereby, l_f and l_r are the front and rear axle distances to the *Center of Gravity* (CG), m equals the overall vehicle mass, and $_f c_y$ and $_r c_y$ are the side stiffnesses of one front and one rear tyre. Figure 2.13(a) shows the output of the simulation. During the simulation, the vehicle decelerated with $a_{x,min}$ until $v \leq v_T$, indicated with the triangle in fig. 2.13(a). The squares indicate the point where the vehicle has to detect the traget to have a final distance of $\Delta s = v_T\, \tau_{set} + s_0$ to the target. The time gap was set to $\tau_{set} = 1\,\text{s}$, and the final stopping distance to $s_0 = 2\,\text{m}$. The same simulations were performed according to standard ISO 22179 [Tec09], describing *Stop-and-Go Adaptive Cruise Control* (FSRA) systems. Only the target speed was set to $v_T = 0$, and the maximum deceleration was defined as a function of the vehicle speed, as depicted in fig. 2.12. The complete list of inputs for the 13 simulations is shown in table 2.1. Additionally, the FOV of the production RADAR sensor ARS 308 of Continental [LSKW10] is added in both graphs, representing the FOV at the time when the ACC vehicle begins to decelerate. This sensor was chosen because it is an example of a currently used RADAR sensor in an ACC-equipped vehicle. In the simulation, the system successfully handles a situation if the square is within the detection range of the sensor. This means that the target is within the FOV when the vehicle begins to decelerate. For ACC-equipped vehicles, this is possible up to an initial vehicle speed of $v_0 = 150\,\text{km/h}$. For FSRA systems, the highest initial velocity for which the situation was adequately handled is in simulation 4 at $v_0 = 80\,\text{km/h}$. This approach can be used to find the desired FOV for an ACC system according to set operation limits.
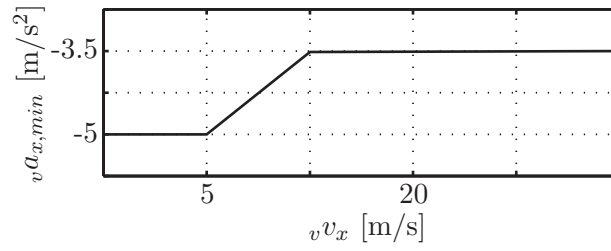
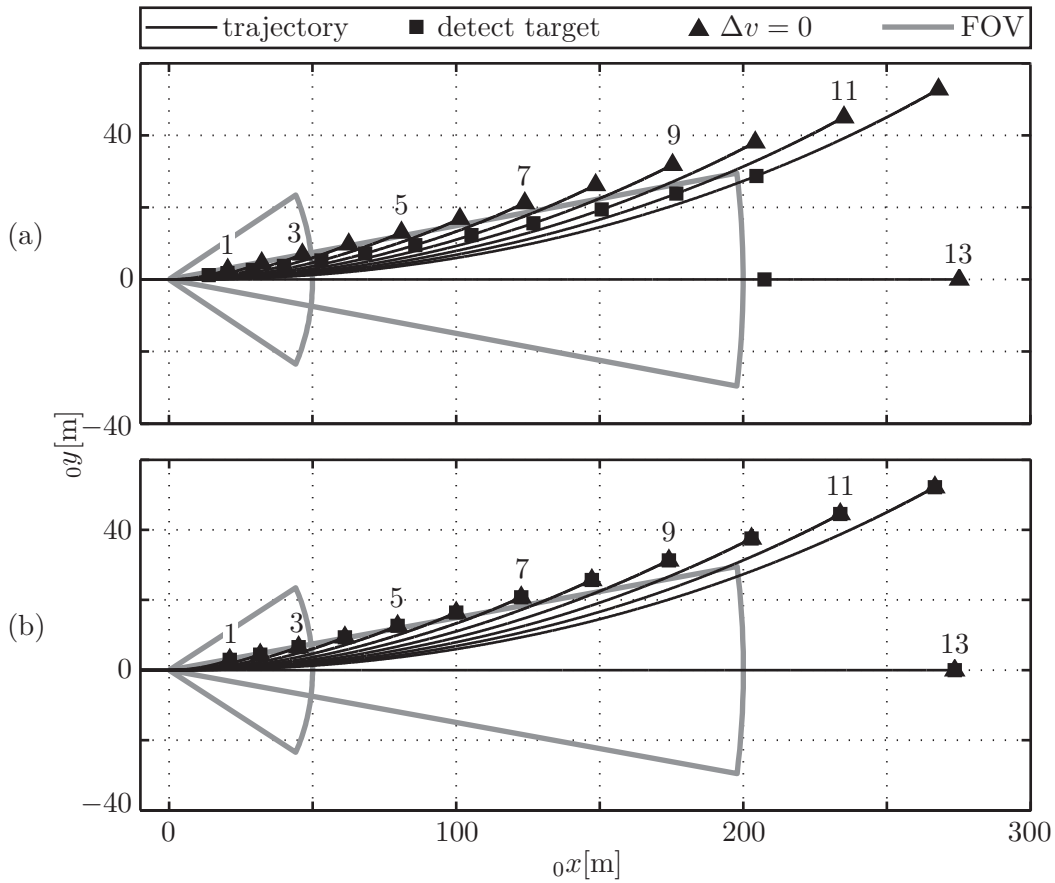Figure 2.12.: Maximum deceleration according to ISO 22179 [Tec09]

Figure 2.13.: Trajectory according to limits defined in (a) ISO 15622 [Tec10] and (b) ISO 22179 [Tec09]

2.3. Vehicle Dynamics Sensors

The Vehicle Dynamics Sensors are part of the *Electronic Stability Control* (ESC), which is standard equipment in every modern vehicle, [WWL$^+$04]. For ACC systems, the yaw rate $_v\omega_z$, the steering wheel angle δ_{SW}, the acceleration in longitudinal $_va_x$ and lateral $_va_y$ directions and the wheel speeds $_c\omega_i$ are sent to the ACC controller. According to [Rob02], the yaw rate is measured through micro-mechanical devices, which vibrate at about 2000 Hz. The yaw motion introduces the *Coriolis Force*, which is proportional to the yaw rate.

Modern vehicles use *Hall sensors* to detect the rotational speed of the wheels, [Rob02]. To this end, a multi-pole-ring is mounted on the wheel bearing. The Hall sensor detects the change in the magnetic field, which is proportional to the wheel speed. The advantage of this sensor type is that measurements near zero speed are possible.

The longitudinal and lateral accelerations are measured using the *Hall Principle* as well, [Rob02]. To achieve this, a permanent magnet is mounted on a spring. Due to accelerations, the spring is deflected, whereby the movement is measured with the help of a Hall sensor. The steering wheel angle δ_{SW} is measured via a potentiometer or magnetic sensors, such as Hall sensors. It is very important that the sensor can measure the steering wheel angle in the range of $\pm720°$, which represents four revolutions, [Rob02]. With the help of gearwheels, the four revolutions at the steering wheel correspond to less than one revolution at the sensor, where the actual steering wheel angle can be measured. Another possibility is to use two angular sensors, where both have different gear ratios to the steering column. The combination of the two measured angles provides clear information about the actual steering wheel angle.

There are other measurement principles possible, but modern vehicles most frequently use the principles described above.

2.4. ACC Controller

Usually, the ACC controller electronics are placed directly in the housing of the environmental-recognition sensor, which is therefore called the *ACC-Sensor and Controller Unit* (ACC-SCU), [WWL$^+$04]. The ACC controller itself consist of two levels, the

- *upper level controller* and the
- *lower level controller*.

The upper level controller receives the distance to the OTF $_sr_{OTF}$ and its relative velocity $_s\dot{r}_{OTF}$ in the sensor coordinate system. The driver sets the desired speed v_{set} and time gap τ_{set}. The lower level controller generates the drive train and brake actuation, u_d and u_b. Each controller receives the current state of the vehicle, the velocity $_vv_x$ and the longitudinal acceleration $_va_x$. As mentioned above, the RADAR sensor requires
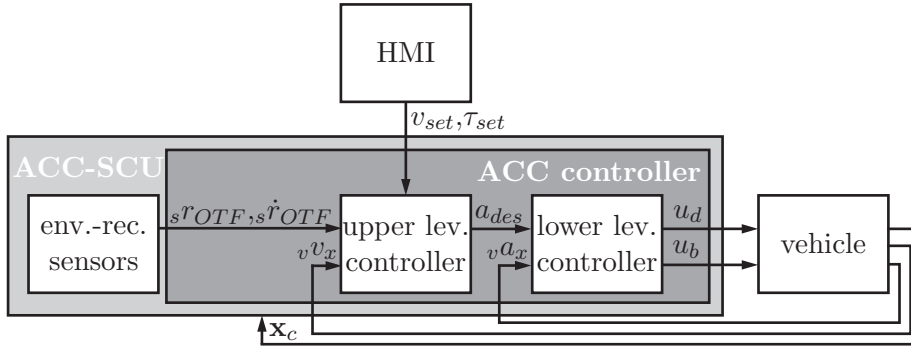
Figure 2.14.: ACC controller structure, adapted from [WWL$^+$04]

information about the vehicle state, $\mathbf{x}_c$, which contains the yaw rate $_v\omega_z$, the steering wheel angle δ_{SW}, the longitudinal $_va_x$ and lateral accelerations $_va_y$, etc. Figure 2.14 shows this controller structure.

2.4.1. Longitudinal Vehicle Dynamics

Unless otherwise indicated, the following chapter is based on [HW09] and [HW10]. Figure 2.15 shows the coordinate systems used. The global coordinate system $(_0x, _0y, _0z)$ is fixed on the ground, and the vehicle coordinate system $(_vx, _vy, _vz)$ is fixed to the vehicle body, with its origin in the CG of the vehicle. The sensor coordinate system $(_sx, _sy, _sz)$ is mounted on the vehicle body as well, with the origin at point S. The centre coordinate system $(_cx, _cy, _cz)$ has its origin at the centre of the wheel, where the $_cx$-axis is parallel to the ground plane, and the $_cy$-axis is the rotation axis of the tyre. In the middle of the contact patch between tyre and ground, the W-point is the origin of the $(_wx, _wy, _wz)$ coordinate system, where the $_wx$-axis is parallel and the $_wz$-axis is perpendicular to the ground plane.

Figure 2.16 shows the kinetic quantities in the longitudinal direction for the vehicle body, one front and one rear wheel. To find the equation of motion for all three bodies, the linear momentum is used. For the vehicle body, it reads

$$m_B \; _v\dot{v}_x = 2 \; _{cf}F_x + 2 \; _{cr}F_x - F_{\beta B} - F_a, \tag{2.12}$$

where m_B describes the vehicle body mass. The climbing resistance is given by

$$F_{\beta B} = m_B \, g \, \cos\beta, \tag{2.13}$$

and the air drag reads

$$F_a = \tfrac{1}{2} \, c_a \, A_x \, \rho_a \; _vv_x^2. \tag{2.14}$$

The air drag depends on the drag coefficient c_a, the frontal projection area A_x of the vehicle, the density of the air ρ_a, and the quadratic to the longitudinal speed $_vv_x$. The
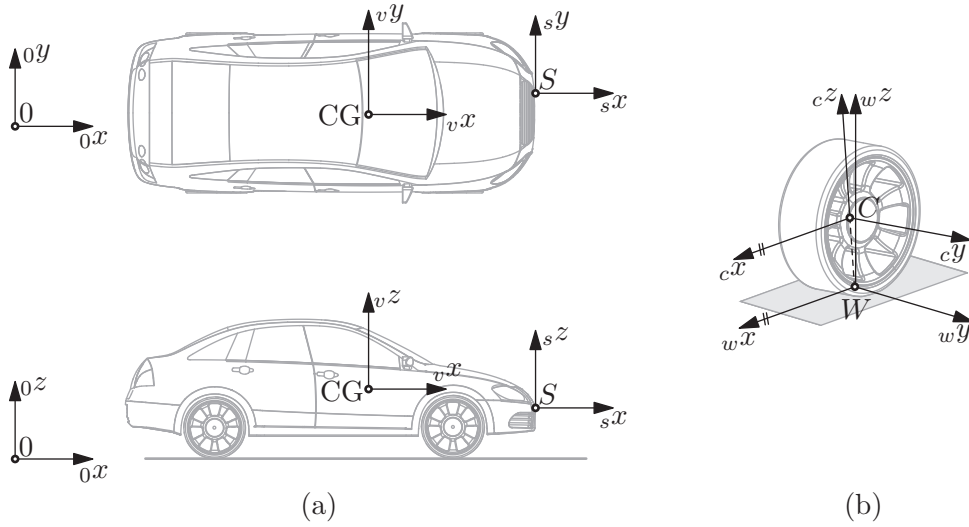
Figure 2.15.: (a) Global, vehicle and sensor coordinate systems and (b) wheel coordinate systems, both adapted from [HW10] and [Deu94]
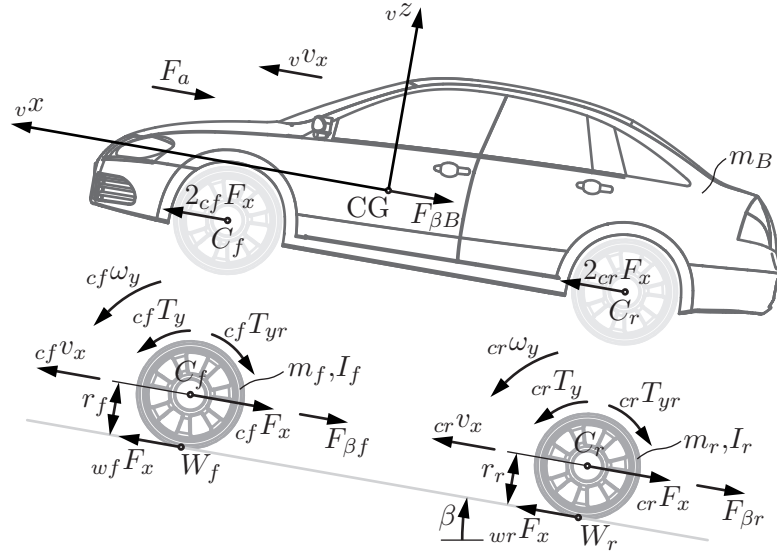
Figure 2.16.: Kinetic quantities in the longitudinal direction, adapted from [HW10]

forces $_{cf}F_x$ and $_{cr}F_x$ act between the vehicle body and the wheels in the longitudinal direction.

The same is done for one wheel of the front axle and one wheel of the rear axle. The linear momentum results in

$$m_j \; _c\dot{v}_{xj} = {_{wj}}F_x - {_{cj}}F_x - F_{\beta j}, \tag{2.15}$$

where j describes the index for one front (f) or one rear (r) wheel. The force $_{wj}F_x$ is the contact force between tyre and road in the W_j-point. The climbing resistance is given by $F_{\beta j} = m_j\, g\, \cos\beta$. The angular momentum for both wheels is given by

$$I_j \; _{cj}\dot\omega_y = \; _{cj}T_y - \; _{cj}T_{yr} - \; _{wj}F_x\, r_j, \tag{2.16}$$

where I_j is the moment of inertia of each wheel, and $_{cj}T_y$ equals the drive and brake torque. $_{cj}T_{yr}$ describes the rolling resistance of the tyre and depends approximately linearly on the wheel load F_{zj} at lower speeds and the distance between W_j and the point of load of $_{wj}F_z$, the distance f_{rj}. Hence, the formula for the rolling resistance reads $_{cj}T_{yr} = f_{rj}\; _{wj}F_z\, r_j$. The moment of inertia at wheel j reads $I_j = I_{wj} + i_{fj}^2\left(\frac{I_g}{2} + i_g^2\,\frac{I_e}{2}\right)$, where I_{wj}, I_g and I_e describe the moment of inertia of the wheel, the gear box and the engine, respectively. The moment of inertia depends quadratically on the transmission ratios of the final drive i_{fj} and of the gear box i_g.

The model in eqs. (2.12) and (2.14) to (2.16) has five *Degrees of Freedom* (DOFs), $_vv_x$, $_{cf}v_x$, $_{cr}v_x$, $_c\omega_{yf}$ and $_c\omega_{yr}$. Excluding elasto kinematics, the longitudinal velocity of the vehicle body and wheels has to be the same, $_vv_x = \; _{cf}v_x = \; _{cr}v_x$. Using this relation, eqs. (2.12) and (2.15) can be simplified to

$$\underbrace{(m_B + 2\, m_f + 2\, m_r)}_{m}\; _v\dot v_x = 2\; _{wf}F_x + 2\; _{wr}F_x - \underbrace{(F_{\beta B} + 2\, F_{\beta f} + 2\, F_{\beta r})}_{F_\beta = m\, g\, \cos\beta} - F_a. \tag{2.17}$$

Excluding longitudinal slip $_{cj}v_x = \; _{cj}\omega_y\, r_j$, due to low accelerations and a high friction potential of the road tyre contact, a combination of eqs. (2.16) and (2.17) results in the simplified longitudinal vehicle model with one DOF ($_vv_x$), which reads

$$\underbrace{\left(m + 2\frac{I_f}{r_f^2} + 2\frac{I_r}{r_r^2}\right)}_{m^*}\; _v\dot v_x = 2\frac{_{cf}T_y - \; _{cf}T_{yr}}{r_f} + 2\frac{_{cr}T_y - \; _{cr}T_{yr}}{r_r} - F_\beta - F_a. \tag{2.18}$$

Here, m^* is the so-called generalized vehicle mass. The torque $_{cj}T_y$ consists of the sum of the drive torque T_{dj} and the brake torque T_{bj}. The drive torque at one wheel reads

$$T_{dj} = \frac{1}{2}\eta_j\; i_{fj}\; i_g\; T_e(\omega_e, u_d)\, b_{dj}. \tag{2.19}$$

The efficiency of the drive train is described by η_j. Depending on the engine throttle u_d and its speed ω_e, the engine generates the torque T_e. The factor b_{dj} describes the percentage of the torque that is sent to the axle j (e. g. a front-driven vehicle has $p_{df} = 1$ and $p_{dr} = 0$). The dynamics of the combustion engine can be described with a first order lag, [Ise02]. Thus the differential equation for the engine torque reads

$$\tau_e\, \dot T_e + T_e = T_{e,min}\left(\omega_e\right) + \left(T_{e,max}\left(\omega_e\right) - T_{e,min}\left(\omega_e\right)\right) u_d, \tag{2.20}$$

where the time constant of the lag equals $\tau_e = 0.5\,\mathrm{s}$. The parameters $T_{e,max}\left(\omega_e\right)$ and $T_{e,min}\left(\omega_e\right)$ describe the maximum and minimum torque that can be generated by the

engine at its speed ω_e. The relation between engine and vehicle speed is given by $\omega_e = i_{fj}\, i_g \frac{v v_x}{r_j}$.

The brake torque at one wheel equals

$$T_{bj} = r_{bj}\; c_j^*\; p_j(u_b)\; A_{bj}, \tag{2.21}$$

where r_{bj} is the effective brake radius, and c_j^* describes the quotient of the clamping force and the friction force at the brake [GOR07]. The brake pressure p_j is a function of the actuation u_b of the driver, and A_{bj} is the brake piston area.

2.4.2. Lower Level Controller

The lower level controller converts the error in the vehicle acceleration $e_a = a_{des} - _v a_x$ into the throttle position of the combustion engine u_d or the brake actuation u_b. As mentioned above, Isermann showed in [Ise02] that the dynamics of the combustion engine can be approximated by a first-order lag element with non-constant parameters, see eq. (2.20). This leads to problems in the parametrization of a *Proportional-Integral Controller* (PI) (k_{Pd} and k_{Id}) or *Proportional-Integral-Derivative Controller* (PID) (k_{Pd}, k_{Id} and k_{Dd}). If the controller is optimized for high loads, the closed loop may become unstable at low loads, due to the high gain k_{Pd} of the controller. On the other hand, if the controller is optimized for low loads, the settling time will be very high, due to the low gain. There is a trade-off between these two extreme examples. In [Ise02], Isermann proposed using a load of 30 to 40 % in order to gain an acceptable performance of the closed loop. Gächter showed in [Gäc12] that a sufficient performance can be reached with a PI controller. He added an anti-windup functionality (k_{AWd}) to limit the output of the integral term of the controller. This is important when the vehicle cannot meet the desired acceleration (e. g. at very high speeds). Another possible way to achieve a better controller performance is to use a method called gain scheduling, [Ise02]. One possibility is shown in [XZ12]. There, a fuzzy system is used to adjust the k_{Id} and k_{Pd} components of a PID controller. The component k_{Dd} is constant. It is important to limit the parameters to the stable range of the closed loop. In [XZ12], the verification stability method of Ziegler-Nichols is used. Additionally, the acceleration controller has to control the gear box because it scales the drive torque, see parameter i_g in eq. (2.19). The combination of a PID controller with gain scheduling and an anti-windup functionality will deliver effective acceleration control, see fig. 2.17.

If the deceleration using the drag torque of the engine is not enough, the lower level controller actuates the brake to meet the desired deceleration. Using eqs. (2.18) and (2.21), the required bake pressure p_{des} and therefore the required actuation u_b can be determined. The only problem is that the parameter c^*, which describes the friction at the brake, is not precisely known. Wallner and Tonchev showed in their investigations [Wal12] and [Ton08] that the friction strongly depends on the temperature, the brake pressure and the velocity. They discovered that with organic brake pads the friction coefficient varies in the range of 0.25 to 0.6, and for sintered pads between 0.4 and 0.8. To compensate for
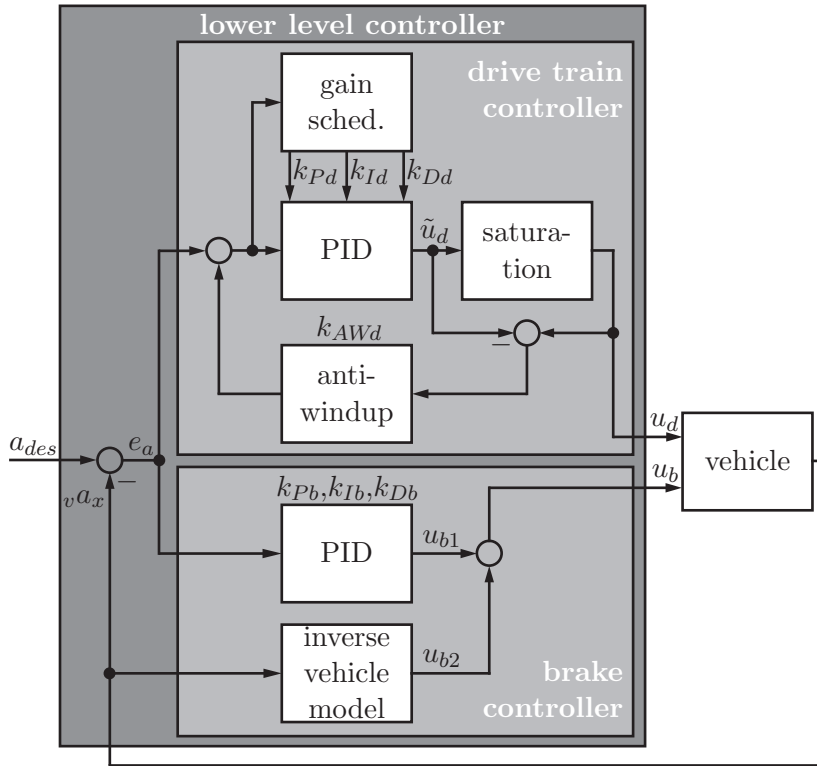
Figure 2.17.: Drive train and brake controller, adapted from [XZ12], and extended with an anti-windup functionality, [HD04]

these effects, the brake controller contains a feedback loop. The PID controller generates the output u_{b1}, which is superimposed by the output u_{b2} of the inverse vehicle model. In [XZ12], Xia et al. demonstrated the good performance of this controller combination.

2.4.3. Upper Level Controller

The upper level controller itself consists of two different parts. The first part is the speed controller, which adjusts the vehicle speed to the set speed v_{set} if no other proceeding vehicle is in front of the ego vehicle or if the proceeding vehicle is driving faster than the ego vehicle. This function is called *Cruise Control* (CC). Gächter showed in [Gäc12], that a PI controller delivers sufficient performance for this function.

The second function is the distance controller, which adjusts the vehicle speed to maintain a distance to the proceeding vehicle defined by

$$s_{set} = s_0 + {}_v v_x \, \tau_{set}. \tag{2.22}$$

Thus, the error signal for the inter-vehicle distance reads

$$e_r = {}_sr_{OTF} - s_{set} \tag{2.23}$$

and the error for the inter-vehicle range rate reads

$$e_{\dot{r}} = {}_s\dot{r}_{OTF}, \tag{2.24}$$

where ${}_s\dot{r}_{OTF}$ is the relative velocity between ego vehicle and OTF. Both should be controlled to zero. Notice that eq. (2.24) is not the derivative with respect to time of eq. (2.23). The derivative $\dot{e}_r$ is given in eq. (2.29) below.

For the design of the lower level controller, a simplified vehicle model is used, which reads

$$\tau_{long}\dddot{x}(t) + \ddot{x}(t) = u(t), \tag{2.25}$$

where $\ddot{x}$ is the longitudinal vehicle acceleration, and $\dddot{x}$ is the longitudinal vehicle jerk. According to [Ise02], the time constant $\tau_{long} = 0.5\,\text{s}$ and the control variable describe the desired acceleration generated by the lower level controller $u(t) = a_{des}$. For the controller design, eq. (2.25) can be rewritten as

$$\dot{\mathbf{x}} = \underbrace{\begin{bmatrix} 0 & 1 & 0 \\ 0 & 0 & 1 \\ 0 & 0 & -\frac{1}{\tau_{long}} \end{bmatrix}}_{\mathbf{A}} \mathbf{x} + \underbrace{\begin{bmatrix} 0 \\ 0 \\ \frac{1}{\tau_{long}} \end{bmatrix}}_{\mathbf{b}} u, \tag{2.26}$$

where $\mathbf{x} = \begin{bmatrix} {}_vx_x & {}_vv_x & {}_va_x \end{bmatrix}^{\mathrm{T}}$. If the target vehicle is driving at a constant speed, eq. (2.26) can be transformed to

$$\dot{\mathbf{e}} = \underbrace{\begin{bmatrix} 0 & 1 & 0 \\ 0 & 0 & -1 \\ 0 & 0 & -\frac{1}{\tau_{long}} \end{bmatrix}}_{\mathbf{A_e}} \mathbf{e} + \mathbf{b}\,u \tag{2.27}$$

with the state vector $\mathbf{e} = \begin{bmatrix} e_r & e_{\dot{r}} & {}_va_x \end{bmatrix}^{\mathrm{T}}$.

The switch between the speed and distance controller is controlled by selecting the minimum of the outputs of the CC and ACC controllers.

2.4.3.1. Constant Time Gap Controller

In [Raj06], Rajamani describes the so-called *Continuous Time Gap* (CTG) controller. Its control law reads

$$a_{des} = \frac{1}{\tau_{set}}\left(e_{\dot{r}} + k\,e_r\right). \tag{2.28}$$

The time derivative from eq. (2.23) reads

$$\dot{e}_r = \underbrace{{}_s\dot{r}}_{e_{\dot{r}}} - {}_va_x\,\tau_{set}. \tag{2.29}$$

Assuming that the vehicle follows the desired acceleration without any delay, $\tau_{long} = 0$ in eq. (2.25), then ${}_va_x = a_{des}$. In this case, the ${}_va_x$ of eq. (2.29) can be inserted in eq. (2.28), which leads to $\dot{e}_r = -k\,e_r$. This differential equation shows that the distance error e_r will drive asymptotically to zero if $k > 0$, assuming that the vehicle can follow the desired acceleration without any delay. This boundary condition should be used to find the parameter k.

2.4.3.2. Model Predictive Control

Unless otherwise indicated, this chapter is based on [Ali10] and [CA07]. The *Model Predictive Control* (MPC) method uses the linear state space model, which describes the vehicle with eq. (2.27), to minimize a cost function to find the control variable u. The main advantage of MPC is that constraints for the control variable can be included in the optimization process. The continuous vehicle model of eq. (2.27) can be written as a discrete state-space model

$$\mathbf{e}_{k+1} = \underbrace{\begin{bmatrix} 1 & T & 0 \\ 0 & 1 & -T \\ 0 & 0 & 1 - \frac{T}{\tau_{long}} \end{bmatrix}}_{\mathbf{A_e}} \mathbf{e}_k + \underbrace{\begin{bmatrix} 0 \\ 0 \\ \frac{T}{\tau_{long}} \end{bmatrix}}_{\mathbf{b}} u_k, \tag{2.30}$$

where the parameter T is the sampling time of the controller. The output equation of the system reads

$$\mathbf{y}_k = \underbrace{\begin{bmatrix} 1 & 0 & 0 \\ 0 & 1 & 0 \end{bmatrix}}_{\mathbf{C}} \mathbf{e}_k, \tag{2.31}$$

where $\mathbf{C}$ is the output matrix. At time step k, the controller calculates the predicted N_p state vectors, which read

$$\mathbf{e}_{k+1|k} = \mathbf{A_e}\,\mathbf{e}_k + \mathbf{b}\,\Delta u_k$$
$$\mathbf{e}_{k+2|k} = \mathbf{A_e}\,\mathbf{e}_{k+1} + \mathbf{b}\,\Delta u_{k+1} =$$
$$= \mathbf{A_e^2}\,\mathbf{e}_k + \mathbf{A_e}\,\mathbf{b}\,\Delta u_k + \mathbf{b}\,\Delta u_{k+1}$$
$$\mathbf{e}_{k+3|k} = \mathbf{A_e^3}\,\mathbf{e}_k + \mathbf{A_e^2}\,\mathbf{b}\,\Delta u_k + \mathbf{A_e}\,\mathbf{b}\,\Delta u_{k+1} + \mathbf{b}\,\Delta u_{k+2}$$
$$\vdots$$
$$\mathbf{e}_{k+N_p|k} = \mathbf{A_e}^{N_p}\,\mathbf{e}_k + \mathbf{A_e}^{N_p-1}\,\mathbf{b}\,\Delta u_k + \mathbf{A_e}^{N_p-2}\,\mathbf{b}\,\Delta u_{k+1} + \cdots +$$
$$+ \mathbf{A_e}^{N_p-N_c}\,\mathbf{b}\,\Delta u_{k+N_c-1}. \tag{2.32}$$
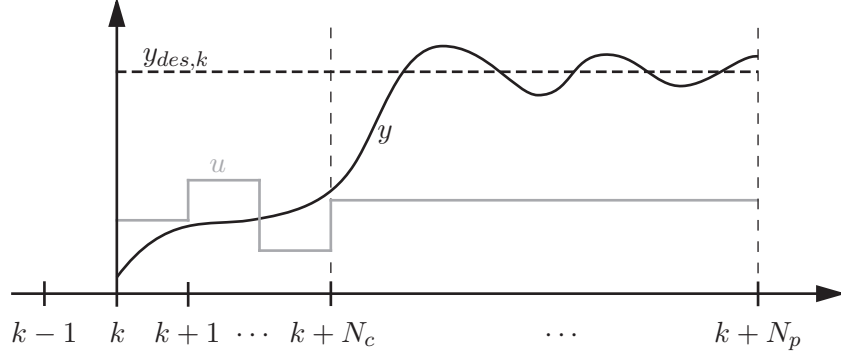
Figure 2.18.: MPC optimization at time step k, adapted from [Ali10]

Here, the symbol $e_{k+j|k}$ is the predicted state vector at time step $k+j$, generated at the present time step k. The same is done for the output equations

$$\mathbf{y}_{k+1|k} = \mathbf{C}\ \mathbf{A_e}\ \mathbf{e}_k + \mathbf{C}\ \mathbf{b}\ \Delta u_k$$

$$\mathbf{y}_{k+2|k} = \mathbf{C}\ \mathbf{A_e}\ \mathbf{e}_{k+1} + \mathbf{C}\ \mathbf{b}\ \Delta u_{k+1} =$$

$$= \mathbf{C}\ \mathbf{A_e^2}\ \mathbf{e}_k + \mathbf{C}\ \mathbf{A_e}\ \mathbf{b}\ \Delta u_k + \mathbf{C}\ \mathbf{b}\ \Delta u_{k+1}$$

$$\mathbf{y}_{k+3|k} = \mathbf{C}\ \mathbf{A_e^3}\ \mathbf{e}_k + \mathbf{C}\ \mathbf{A_e^2}\ \mathbf{b}\ \Delta u_k + \mathbf{C}\ \mathbf{A_e}\ \mathbf{b}\ \Delta u_{k+1} + \mathbf{C}\ \mathbf{b}\ \Delta u_{k+2}$$

$$\vdots$$

$$\mathbf{y}_{k+N_p|k} = \mathbf{C}\ \mathbf{A_e}^{N_p}\ \mathbf{e}_k + \mathbf{C}\ \mathbf{A_e}^{N_p-1}\ \mathbf{b}\ \Delta u_k + \mathbf{C}\ \mathbf{A_e}^{N_p-2}\ \mathbf{b}\ \Delta u_{k+1} + \cdots$$

$$+ \mathbf{C}\ \mathbf{A_e}^{N_p-N_c}\ \mathbf{b}\ \Delta u_{k+N_c-1}. \tag{2.33}$$

Figure 2.18 shows a graphical illustration of the process described above. The controller seeks to minimize the error $y_{des} - y$. Therefore, the output is calculated for N_p time steps, beginning at the present step k. The control variable u_k is predicted for N_c steps (note that $N_c \leq N_p$). In eqs. (2.32) and (2.33), the new control variable $\Delta u_j = u_j - u_{j-1}$ is introduced. Only the first control variable Δu_k is applied to the system. In the next step, the optimization starts from the beginning.

The column vectors

$$\mathbf{Y}_k = \begin{bmatrix} \mathbf{y}_{k+1|k}^{\mathrm{T}} & \mathbf{y}_{k+2|k}^{\mathrm{T}} & \cdots & \mathbf{y}_{k+N_p|k}^{\mathrm{T}} \end{bmatrix}^{\mathrm{T}} \tag{2.34}$$

and

$$\mathbf{\Delta U}_k = \begin{bmatrix} \Delta u_k & \Delta u_{k+1} & \Delta u_{k+2} & \cdots & \Delta u_{k+N_c-1} \end{bmatrix}^{\mathrm{T}} \tag{2.35}$$

are introduced to have a more compact notation of eqs. (2.32) and (2.33), which reads

$$\mathbf{Y}_k = \mathbf{F}\ \mathbf{e}_k + \mathbf{\Phi}\ \mathbf{\Delta U}_k. \tag{2.36}$$

Here, the new matrices are defined as

$$\mathbf{F} = \begin{bmatrix} \mathbf{C}\,\mathbf{A_e} \\ \mathbf{C}\,\mathbf{A_e^2} \\ \mathbf{C}\,\mathbf{A_e^3} \\ \vdots \\ \mathbf{C}\,\mathbf{A_e}^{N_p} \end{bmatrix} \text{ and} \tag{2.37}$$

$$\mathbf{\Phi} = \begin{bmatrix} \mathbf{C}\,\mathbf{b} & \mathbf{0} & \mathbf{0} & \cdots & \mathbf{0} \\ \mathbf{C}\,\mathbf{A_e}\,\mathbf{b} & \mathbf{C}\,\mathbf{b} & \mathbf{0} & \cdots & \mathbf{0} \\ \mathbf{C}\,\mathbf{A_e^2}\,\mathbf{b} & \mathbf{C}\,\mathbf{A_e}\,\mathbf{b} & \mathbf{C}\,\mathbf{b} & \cdots & \mathbf{0} \\ \vdots & \vdots & \vdots & \ddots & \vdots \\ \mathbf{C}\,\mathbf{A_e}^{N_p-1}\,\mathbf{b} & \mathbf{C}\,\mathbf{A_e}^{N_p-2}\,\mathbf{b} & \mathbf{C}\,\mathbf{A_e}^{N_p-3}\,\mathbf{b} & \cdots & \mathbf{C}\,\mathbf{A_e}^{N_p-N_c}\,\mathbf{b} \end{bmatrix}. \tag{2.38}$$

The cost function is defined as

$$J_k = \left(\mathbf{Y}_{des,k} - \mathbf{Y}_k\right)^{\mathrm{T}} \left(\mathbf{Y}_{des,k} - \mathbf{Y}_k\right) + \mathbf{\Delta U}_k^{\mathrm{T}}\,\mathbf{R}\,\mathbf{\Delta U}_k, \tag{2.39}$$

where the vector containing the desired output reads

$$\mathbf{Y}_{des,k} = \begin{bmatrix} \mathbf{I}_{(m\times m)} & \mathbf{I}_{(m\times m)} & \cdots \end{bmatrix}^{\mathrm{T}} \mathbf{y}_{des,k}. \tag{2.40}$$

The size of the identity matrix $\mathbf{I}$ is $(m \times m)$, where m is the number of outputs of the system (i.e. the number of rows of y). The matrix $\mathbf{R}$ weights the right part of eq. (2.39), which contains the change of the control variable to the left part, which describes the error of the output. Entering eq. (2.36) in the cost function of eq. (2.39), the optimal solution can be found by minimizing J. Therefore, the necessary condition is that the first derivative of J with respect to $\mathbf{\Delta U}_k$ equals 0. Solving this equation, the optimal control variable reads

$$\mathbf{\Delta U}_k = \left(\mathbf{\Phi}^{\mathrm{T}}\mathbf{\Phi} + \mathbf{R}\right)^{-1} \mathbf{\Phi}^{\mathrm{T}} \left(\mathbf{Y}_{des,k} - \mathbf{F}\,\mathbf{e}_k\right). \tag{2.41}$$

Performing this optimization by solving eq. (2.41) is fast compared to a numerical optimization. The first component of $\mathbf{\Delta U}_k$ is passed to the lower level controller.

As already mentioned above, the MPC is able to include constraints, such as limiting the desired acceleration to a minimum and a maximum, $a_{min} \leq u_k \leq a_{max}$. This limitation results in a system of $2\,N_c$ inequalities because they have to be a function of the components of $\mathbf{\Delta U}_k$. This optimization problem, which cannot be solved analytically, increases the computation time.

2.4.3.3. Fuzzy Control

The main advantage of the *Fuzzy Controller* is that it can be designed without exact knowledge of the plant, [Ada09a]. As a first step, linguistic labels are assigned to fuzzy
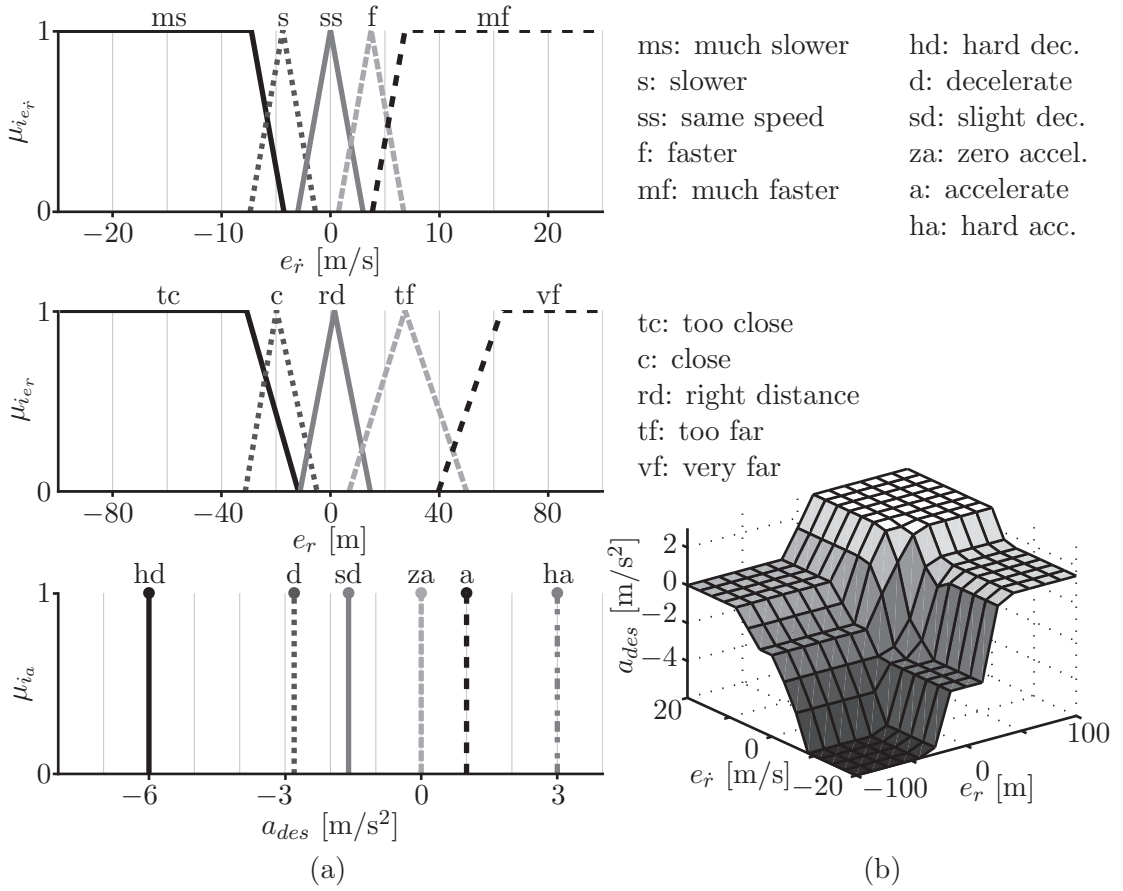
Figure 2.19.: (a) Membership functions μ and (b) resulting output a_{des} for a fuzzy ACC lower level controller of [Gäc12]

variables. For ACC systems, the fuzzy variables are the inter-vehicle distance and speed errors, e_r and $e_{\dot{r}}$ of eqs. (2.23) and (2.24), and the desired acceleration a_{des}. In his thesis [Gäc12], Gächter defined a set of membership functions μ, which are depicted in fig. 2.19(a). An error of $e_r = -30\,\text{m}$ cannot be clearly assigned to one membership function $\mu_{i_{e_r}}$, see fig. 2.19(a). It results in $\mu_{tc}(-20) = 0.396$ and $\mu_c(-20) = 1$. All the other membership functions of the position error $\mu_{i_{e_r}}$ equal zero. This fuzzy assignment (i.e. all the values between zero and one are possible for each membership function) gives the method its name, [Ada09a]. The membership function for a speed error of $e_{\dot{r}} = 4\,\text{m/s}$ is $\mu_f(4) = 1$. The operation, called aggregation, provides a logical connection between $\mu_{i_{e_r}}$ and $\mu_{i_{e_{\dot{r}}}}$. Gächter used the logical *and*, which can be mathematically described as minimum function, $\mu_{tc,f} = \min\{\mu_{tc}(-20), \mu_f(4)\} = 0.396$ and $\mu_{c,f} = \min\{\mu_c(-20), \mu_f(4)\} = 1$. This operation is carried out for all possible 25 combinations of $\mu_{i_{e_r}}$ and $\mu_{i_{e_{\dot{r}}}}$. Table 2.2 shows the control rules in matrix form. There, it can be seen that both membership functions $\mu_{tc,f}$ and $\mu_{c,f}$ correspond to the slight

Table 2.2.: Fuzzy control rules, according to [Gäc12]

		e_r				
		tc	c	rd	tf	vf
	ms	hd	d	d	d	a
	s	d	d	d	sd	a
$e_{\dot{r}}$	ss	sd	sd	za	a	ha
	f	sd	sd	a	ha	ha
	mf	za	za	a	ha	ha

deceleration of $a_{tc,f} = a_{c,f} = a_{sd} = -1.635\,\text{m/s}^2$. In general, the defuzzification reads

$$a_{des} = \frac{\sum\limits_{i_{e_r}} \sum\limits_{i_{e_{\dot{r}}}} a_{i_{e_r},i_{e_{\dot{r}}}} \; \mu_{i_{e_r},i_{e_{\dot{r}}}}}{\sum\limits_{i_{e_r}} \sum\limits_{i_{e_{\dot{r}}}} \mu_{i_{e_r},i_{e_{\dot{r}}}}}. \tag{2.42}$$

In the given example, the defuzzification results in $a_{des} = -1.635\,\text{m/s}^2$.

Figure 2.19(b) shows the output for the described fuzzy controller. The method used is just an example. There are many other possible ways to vary the steps carried out during the design process of the controller, as described in [Ada09a].

2.4.3.4. Sliding Mode Controller

Unless otherwise indicated, this chapter is based on [Ada09b] and [SEFL14]. With the *Sliding Mode Control* (SMC) method, the controller switches between two different laws. The main advantage is that they are very robust in terms of parameter uncertainties. One disadvantage is that the switching around the desired value generates chattering. For the design, the model

$$\dot{\mathbf{x}}_{SMC} = \mathbf{A}_{SMC}\,\mathbf{x}_{SMC} + \mathbf{b}\,u \tag{2.43}$$

is used, where $\mathbf{A}_{SMC} = \mathbf{A}$ of eq. (2.26). The state vector contains the components $\mathbf{x}_{SMC} = \begin{bmatrix} -e_r & -e_{\dot{r}} & _v a_x \end{bmatrix}^{\text{T}}$. The switching function, which is defined as a function of the state vector, reads

$$s(\mathbf{x}_{SMC}) = \mathbf{r}^{\text{T}}\,\mathbf{x}_{SMC}, \tag{2.44}$$

where $\mathbf{r}^{\text{T}}\,\mathbf{x}_{SMC}$ describes the sliding surface. The control law, which is only defined for $s(\mathbf{x}_{SMC}) \neq 0$, reads

$$u(\mathbf{x}_{SMC}) = \begin{cases} u_+(\mathbf{x}_{SMC}) & \text{for } s(\mathbf{x}_{SMC}) > 0 \\ u_-(\mathbf{x}_{SMC}) & \text{for } s(\mathbf{x}_{SMC}) < 0. \end{cases} \tag{2.45}$$

The reachability condition means that the trajectory of $\mathbf{x}_{SMC}$ reaches the defined surface s within a finite time. Most literature uses

$$\dot{s} = -q\,\text{sign}(s(\mathbf{x}_{SMC})) - k\,s(\mathbf{x}_{SMC}) \tag{2.46}$$
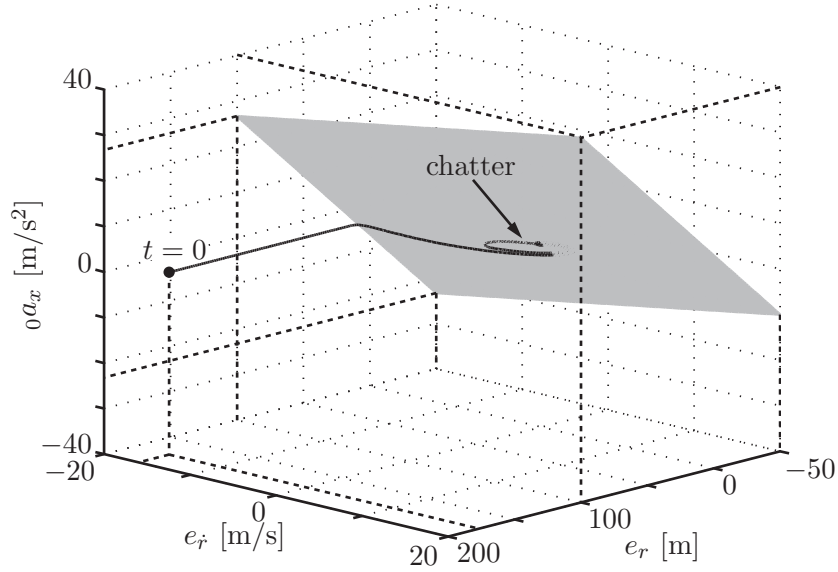
Figure 2.20.: Trajectory and sliding surface from the simulation in chapter 2.4.4

to meet this requirement, [Ada09b, SEFL14]. The parameters q and k have to be positive. The time derivative of the surface reads $\dot{s} = \frac{\partial s}{\partial \mathbf{x}_{SMC}} \dot{\mathbf{x}}_{SMC}$. Using this formulation, eqs. (2.44) and (2.46), the control law ends up as

$$a_{des} = -\frac{\mathbf{r}^{\mathrm{T}} \mathbf{A}_{SMC} \mathbf{x}_{SMC} + q \operatorname{sign}(\mathbf{r}^{\mathrm{T}} \mathbf{x}_{SMC}) + k \, \mathbf{r}^{\mathrm{T}} \mathbf{x}_{SMC}}{\mathbf{r}^{\mathrm{T}} \mathbf{b}}. \tag{2.47}$$

The vector $\mathbf{r}$ and the scalars q and k are used to tune the controller. Note that in the case of eq. (2.25), only the last component of $\mathbf{b}$ is not equal to zero. Therefore, the corresponding component of $\mathbf{r}$ also cannot be zero, or else a division by zero will occur. The term with the signum function mainly causes the chatter around the defined surface. If eq. (2.44) is changed to $\dot{s} = -k \, s$, meaning $q = 0$, the chatter can be minimised, as Drew did in [Dre02]. It will not work in general because the error will not drive to zero in finite time. Nevertheless, he achieved satisfying results. Instead of setting $q = 0$, the signum function may be replaced by a sigmoid function. This minimises chatter, but there is the same problem of asymptotic convergence towards zero. Therefore a real sliding on the defined surface is not possible. However, its performance is close to the system with the input of eq. (2.47), and therefore it is called *Quasi Sliding Mode*.

Figure 2.20 shows the trajectory and the sliding surface for the simulation done in chapter 2.4.4. When the trajectory is near the surface and runs through it, it changes the side of the plane very often, which leads to the aforementioned chatter.

2.4.4. Comparison of the Upper Level Controllers

This chapter compares simulations carried out with the upper level controllers of chapters 2.4.3.1 to 2.4.3.4. The control laws are given in eqs. (2.28), (2.41), (2.42) and (2.47), and the controller parameters are listed in appendix C.1. The ego vehicle was simulated with eq. (2.26) with the initial condition $\mathbf{x}_0 = \begin{bmatrix} 0 & 30 & 0 \end{bmatrix}^{\mathrm{T}}$. The target vehicle model reads

$$\dot{\mathbf{x}}_T = \begin{bmatrix} 0 & 1 \\ 0 & 0 \end{bmatrix} \mathbf{x}_T + \begin{bmatrix} 0 \\ 1 \end{bmatrix} u_T, \tag{2.48}$$

with the state vector $\mathbf{x}_T = \begin{bmatrix} {}_0x_x & {}_0v_x \end{bmatrix}^{\mathrm{T}}$ describing the position and velocity in the global coordinate system. The initial condition of the target vehicle was set to $\mathbf{x}_{T,0} = \begin{bmatrix} 200 & 14 \end{bmatrix}^{\mathrm{T}}$. The acceleration of the target u_T was held constant to zero for the first $20\,\mathrm{s}$ of the simulation. It then accelerated with $1\,\mathrm{m/s^2}$ for $10\,\mathrm{s}$, followed by driving at constant speed for another $10\,\mathrm{s}$. The target then decelerated with $-3\,\mathrm{m/s^2}$ for $5\,\mathrm{s}$, followed again by constant driving for $15\,\mathrm{s}$.

Figure 2.21 shows the output for this manoeuvre. From fig. 2.21, it is clear that the fuzzy controller has the worst performance. It has an undershoot in the velocity ${}_vv_x$ and is not really able to settle the distance error e_r. The simulation with the lowest acceleration ${}_va_x$ was the MPC, which controls the vehicle very smoothly. The CTG and the SMC methods have similar results, but the low complexity of the CTG control law leads to a better evaluation of the CTG than the SMC approach. Of course, all four controllers could have better performances if more suitable parameters were identified. The performance of the MPC could be improved if constraints were included in the control law. In this way, the big negative slope at the beginning could be avoided by limiting the change of a_{des} between two time steps.

2.5. Actuators

The following two sections focus only on the functional requirements of the ACC system. The actuators have to fulfil many additional requirements regarding functional safety and fault detection.

2.5.1. Drive Actuators

As shown in eq. (2.19), among other factors, the drive torque depends on the gear ratio i_g of the selected gear. For the drive actuators, the engine and the gear box form one unit. The actuation is performed with the accelerator pedal position u_d. To ensure the required comfort of the ACC vehicle, gear shifting operations during controller oscillations should be prevented, [WDS09]. In some cases, it might be possible that the lower level controller (chapter 2.4.2) generates the sum of the drive torque at all wheels of eq. (2.19). In such
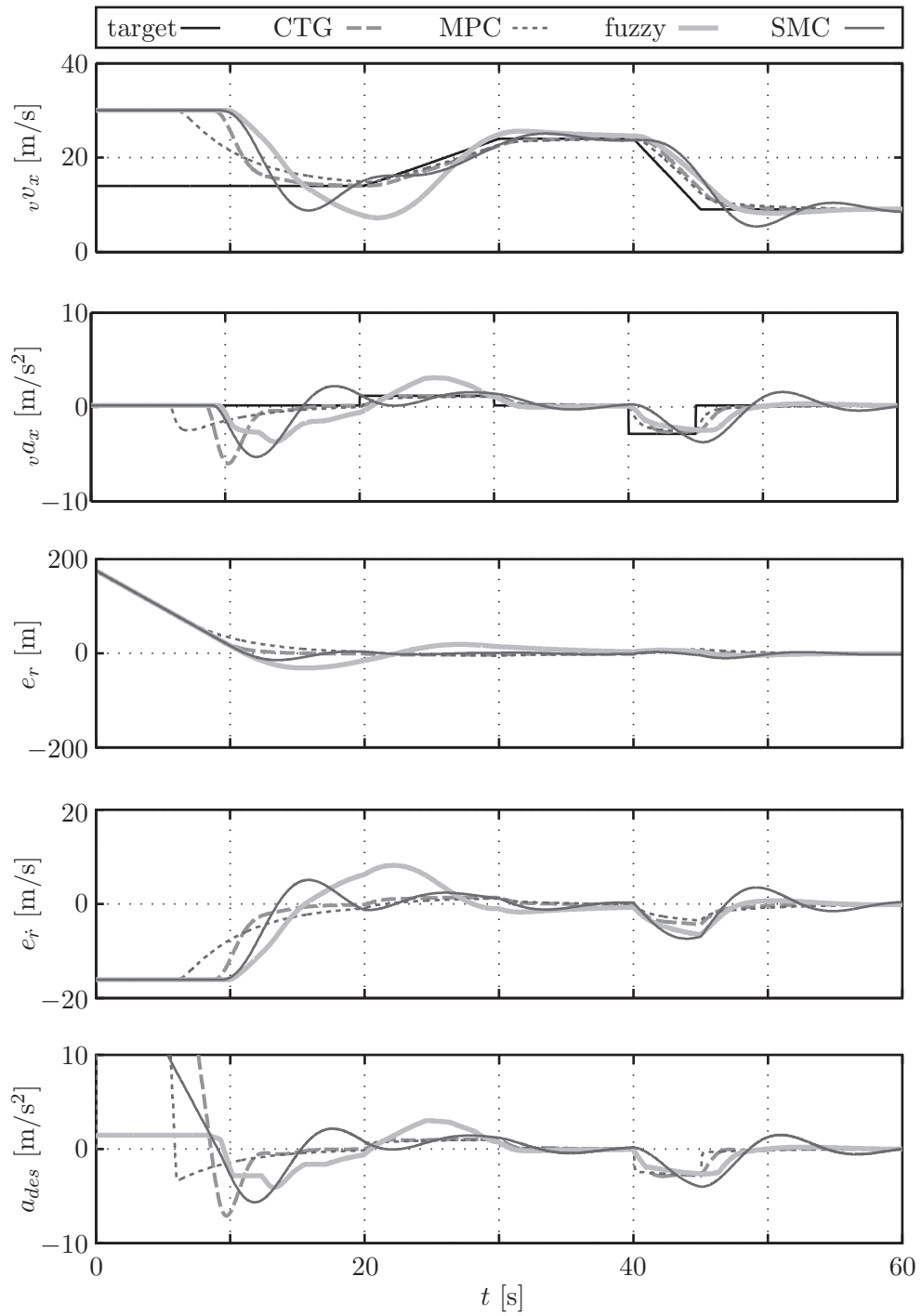
Figure 2.21.: Simulation results

cases, the u_d is calculated in the engine and gear controller and is not part of the ACC, [WDS09].

2.5.2. Brake Actuators

In most of the vehicles, the brake actuation is done via the ESC. Although it is possible to do this with the brake booster, this is not common due to higher costs and much higher delay for building up brake pressure, [Fei13]. For the following considerations, which actuation is used is not relevant.

In eq. (2.21), it is evident that the brake torque T_b and therefore the longitudinal acceleration $_v a_x$ of the vehicle are proportional to the brake pressure p. Winner et al. mentioned in [WDS09] that a change in the brake pressure of 1 bar will lead to a change in the longitudinal acceleration of 0.07 to $0.14 \, \mathrm{m/s^2}$ for a standard vehicle. Regarding comfort, the brake actuation should be able to control the pressure in steps smaller than 0.5 bar, and a pressure overshoot has to be avoided. For FSRA, the task of preventing movement when the vehicle has stopped is very important. To meet this requirement, Laiou et al. showed in [LP08] that this is possible by increasing the brake pressure at a vehicle speed near 0 m/s. If the brakes are applied too early, there will be high accelerations, which will not satisfy the driver. On the other hand, if the brakes are applied too late, the vehicle might move backwards, which must be prevented under all circumstances. When the FSRA starts to move from zero speed, the wheel torque has to be increased before the brake is released, [LP08]. The coordination of these operations places high demands on both the brakes and the drive controllers.

3

Development Process

The development and validation of *Advanced Driver Assistance System* (ADAS) are a challenging tasks, especially because it is a combination of the disciplines of *electric/electronics*, *vehicle dynamics* and *human factors engineering*. In the automotive industry, the *V-Model*, adopted from software engineering, is the basis for the development of complex electronic functions, [Mau09], [Rei12]. Figure 3.1 shows the main stages of the development process. The V-Model can be divided into two parts: the left branch, where the requrirements are set and the development is done, and the right branch for the validation, [Rei12]. It is important that all the requirements must lead to a test case, which is assessed during the validation process. Therefore, the requirements have to be set clearly, [Mau09], [Rei12]. For *Adaptive Cruise Control* (ACC) systems, the formulation that the vehicle equipped with such a system should be able to follow another vehicle that decelerates is not sufficient. It should be added that the vehicle in front decelerates with a_{dec}, the initial conditions have to be defined $(_v v_0, _s r_0, _s \dot{r}_0)$, and evaluation criteria have to be set (e. g. the distance between the two vehicles must not fall below a defined limit of $_s r_{min}$). Additionally, the environmental conditions have to be set (e. g. the manoeuvre has to be carried out on a straight road with no other vehicles and no buildings near the road in clear weather).

This method works properly if all of the requirements are known at the beginning of the development process, [Mau09]. With new functions or very complex systems, there will be iterations. For example, if one test cannot be passed due to the performance of an actuator, the requirements on the performance have to be adjusted, and the actuator has to be redesigned. On the component level, the process shown in fig. 3.1 is divided into the sub-processes for the components involved, [Rei12]. In the development process for an ACC system, the environmental-recognition sensors, the controller hardware and
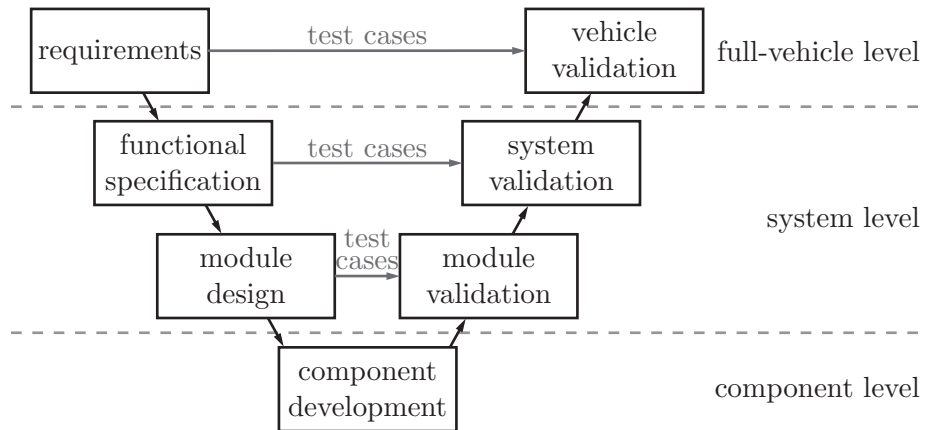
Figure 3.1.: V-Model, adapted from [Mau09] and [Rei12]

software, the actuators and the *Human-Machine Interface* (HMI) are parts of the system, see fig. 2.1. Each of them has its own sub-processes.

3.1. Full-Vehicle Level

There are different ways to perform tests on the *full-vehicle level*. Since maintaining the safety of the people involved is the most important task, tests conducted in driving simulators are the safest choice. The advantage is that the repeatability is very good, and safety-critical situations can be simulated with no risk. The disadvantage is that the probands know that they are not really driving a car, so they may behave differently than they would in real traffic, [Bre09].

The second possibility is to perform test drives on closed test tracks. Here, the probands are driving real cars, but complex traffic situations cannot be simulated or require a very high effort, [Bre09]. Examples are given by Bock in [Boc09] and Schwab et al. in [SLZB14]. There, the probands drove on test tracks and wore a special device, an *Optical See Through Head-Mounted Display*, which projects the traffic on the road in front of the vehicle. The position of the ego vehicle, which must be measured precisely, is sent to a simulation software. There, the relative movement between the virtual traffic and the ego vehicle is calculated by a multi-body simulation. Thereby, a sensor model measures the required quantities and sends them to the real ADAS controller. This method is suitable for evaluating safety-oriented systems, such as the *Automatic Emergency Brake* (AEB). One main disadvantage is that no real environmental-recognition sensor is used, which has a significant influence on the performance of the system.

One method for performing tests on the full-vehicle level is described by Gietelink et al. in [GPSV06]. They built up a facility where the ego vehicle is driven on a dynamometer. The motion of the other vehicles is simulated by moving robot cars in front of the ego

vehicle. The major advantages of this method are that the real environmental sensor is used and safety-critical situations can be carried out without any risk. The disadvantage is that the subjective evaluation of probands cannot be performed because there will be no accelerations acting on them. One idea to solve this problem might be to couple the chassis dyno with a moving base driving simulator.

The most realistic way to asses ADAS is to conduct test drives in real traffic. The disadvantage is that no defined manoeuvres can be performed, but the results are the most realistic that can be generated, [Bre09]. However, critical situations cannot be assessed.

The above mentioned tests on the full-vehicle level are usually subjective evaluations of the probands. These are very important because it is the way a customer would evaluate the system. For the development process, it is very important to use objective measures. Examples are given in [Hol12], [SBB$^+$07] and [BHLSE13]. In his diploma thesis [Hol12], Holl defined a list of manoeuvres which are used to evaluate a vehicle equipped with ACC or *Stop-and-Go Adaptive Cruise Control* (FSRA). The test driver has to provide subjective evaluations of defined criteria. The vehicle is also equipped with a measurement system, which records such data as the longitudinal vehicle speed and acceleration $_vv_x$, $_va_x$ and, if available, the relative distance and speed to the target vehicle, $_sr$, $_s\dot{r}$. The subjective and objective evaluations lead to an overall assessment in the categories of

- function,

- comfort,

- sensor function,

- disturbing noise inside the car,

- geometric integration of the sensor(s),

- operability and

- false positives.

The term *false positives* describes situations in which the system performs an unnecessary intervention. This might occur when the environmental-recognition sensor detects a ghost object and the ADAS begins to decelerate, leading to dangerous situations, which has to be prevented under all circumstances. Holl's method helps to compare the behaviour of different systems or different parametrizations of systems in the above-mentioned categories. Despite the attempt to asses the systems in an objective way, the feeling of the test driver influences the output and therefore yields a subjective evaluation. This method works very well for comparing systems, but it will not work for absolute evaluation of individual systems.

Schrauf et al. described in [SS13] a method for objectively evaluating automated and autonomous driving vehicles. In this method, many test drives with probands are conducted and recorded, and each of the probands then evaluates the system's performance.
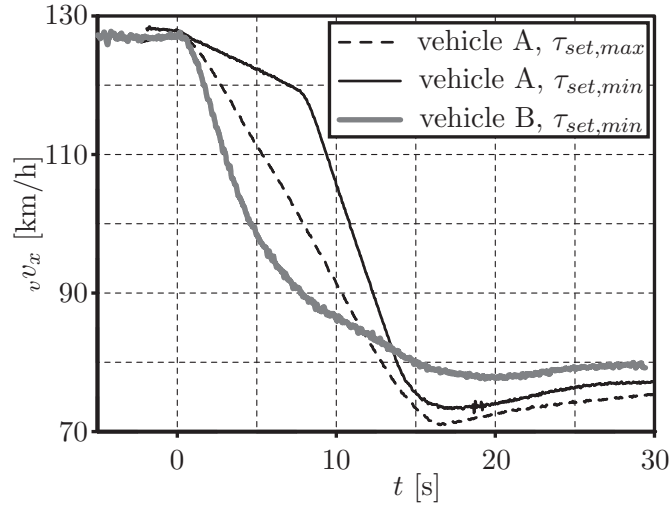
Figure 3.2.: Measurements for manoeuvre "Approach on slower moving target in the same lane", adapted from [Hol12] and [BHLSE13]

This huge database is used to train neural networks. To validate the tests, data that is fed into the neural network has to be recorded. The output should be the same as if probands asses the system. It is a promising approach because they have already used it extensively to evaluate the driveability of drive trains, and it has performed quite well.

Figure 3.2 shows an example for the manoeuvre called "Approach on slower moving target in the same lane". Here, the ego vehicle is driving at a constant speed of $_vv_x = 130\,\mathrm{km/h}$ and is approaching a target with a speed of $_0v_T = 80\,\mathrm{km/h}$. The manoeuvre is conducted three times, two times with vehicle A and one time with vehicle B. For vehicle A, the time gap is set to $\tau_{set,min} = 1\,\mathrm{s}$ and $\tau_{set,max} = 2.3\,\mathrm{s}$. The measurement with vehicle B is made with the setting $\tau_{set,min} = 1\,\mathrm{s}$. It is evident that the behaviours in this manoeuvre differ significantly, even between the two measurements of vehicle A. Some of the test drivers rate vehicle A better than vehicle B, although vehicle B has less undershoot in speed, [BHLSE13]. The different evaluations demonstrate why an objective assessment is very difficult. From the point of view of control theory, less undershoot is better, but drivers may assess it in another way.

3.2. System and Component Levels

For the development and validation on the *system* and *component levels*, simulation tools, module and component test benches are used. Often, a module test bench is used for the validation and development of camera-based ADAS. In this case, a camera faces a monitor where the *Field of View* (FOV) of the sensor is simulated. Such a setup is called *Hardware-in-the-Loop* (HIL). The picture on the monitor is an animation of a simulation

or a recorded video of a real situation. An example for such an application is given in [GS11]. There, *Lane-Departure Warning* (LDW) and *Lane-Keeping Assistant* (LKA) systems are tested. The advantage of HIL is that complicated situations can be tested in a time and cost-efficient way. Nevertheless the correct behaviour of the system has to be defined in advance. Another example for HIL testing is given in [ABF$^+$03]. One significant disadvantage of the HIL method in general is that for tests of an automotive *Electronic Controller Unit* (ECU), the whole data bus has to be simulated. Otherwise, the ECU will not work.

Another challenge is the significant diversity of variants a system is developed for. The aim of vehicle manufacturers is to use the same system in many different vehicles or derivates, [WSSR10]. This leads to a very high number of combinations of different systems or modules with which the ADAS should work. Therefore, a structured development and test plans are needed to design a stable, affordable and innovative system. To accomplish these goals, *Model-in-the-Loop* (MIL) and HIL methods are used. With HIL tests, the device being tested is a physical component. In contrast, MIL tests assess software. The advantage is that MIL tests can be performed before any physical part is available.

In [WSSR10], Wehner et al. show that a time and cost-efficient development process requires realistic sensor data, even in the early development phase. The challenge is that the right sensors may not be available at that time. Magosi describes in [Mag13] a method for dealing with this problem. Commercially available simulation packages provide optimal sensors as environmental recognition sensors, meaning they make no errors and have no delays. Magosi developed a phenomenological sensor model that applies noise and random signal losses to the optimal data. Thus, the components in the simulation can be trained to handle such special situations. In [BMLSE13], this sensor model was compared to a commercially available sensor model by simulating a frequently occurring motorway situation. The ego vehicle, equipped with an AEB system, is travelling at 130 km/h and overtakes a platoon of different vehicles travelling at 90 km/h. At a certain distance, one of the vehicles of the platoon moves into the lane of the ego vehicle. The driver of the ego vehicle does not react to the emerging object, and the AEB system applies the brakes. The outcomes of the simulations with the two different sensor models were completely different. If the optimal sensor model is used, the AEB system prevents the crash. The simulation with the proposed model leads to a speed reduction of the ego vehicle, but the AEB system does not prevent the collision. The main difference between the two simulations is that the phenomenological model requires a certain time from the appearance of the object until the data processing passes the information to the ADAS. This realistic behaviour can be used to improve the simulation quality and to find ways to deal with realistic data.

4

Measurements

4.1. Measurement Setup

All the quantities are measured in the coordinate systems of fig. 4.1. There, the origin of the vehicle coordinate system is located at the *Center of Gravity* (CG) of the ego vehicle with its axes $(_vx, _vy, _vz)$, in accordance with the *Deutsches Institut für Normung* (DIN) standard 70000, [Deu94]. The environmental-recognition sensor coordinate system $(_sx, _sy, _sz)$ with the origin S is shifted to the front bumper of the vehicle. The transformation from the sensor to the vehicle coordinate system reads

$$\begin{bmatrix} _vx \\ _vy \\ _vz \end{bmatrix} = \underbrace{\begin{bmatrix} _v^Ss_x \\ _v^Ss_y \\ _v^Ss_z \end{bmatrix}}_{_v^S\mathbf{s}} + \begin{bmatrix} _sx \\ _sy \\ _sz \end{bmatrix}, \tag{4.1}$$

where the vector $_v^S\mathbf{s}$ gives the position of the sensor in the vehicle coordinate system. The global coordinate system $(_0x, _0y, _0z)$ is placed on the road surface. Each of the wheels has its own coordinate system $(_cx, _cy, _cz)$ with its origin C at the centre of the wheel. The $_cy$-axis is the rotation axis of the wheel, and the $_cx$-axis is parallel to the $(_0x, _0y)$-plane. Figure 4.1 shows the coordinate system for the front left (fl) wheel. Figure 2.15(b) depicts the wheel coordinate systems in detail.

For the measurements, a vehicle called the *ego vehicle* is equipped with an environmental-recognition sensor, a camera and a measurement system. The same equipment is placed in another vehicle, called the *target vehicle*. These two vehicle measurement systems are
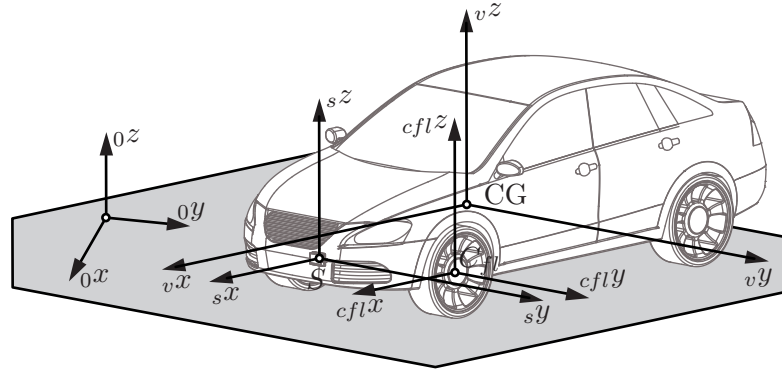
Figure 4.1.: Coordinate systems for the measurements

connected via *Wireless Local Area Network* (WLAN), see fig. 4.2. As an environmental-recognition sensor, a production *Radio Detection and Ranging* (RADAR) sensor of type Continental ARS 308 is used. Additionally, the vehicle is equipped with a camera, which is mounted behind the windscreen. The recorded video data is not directly used in data processing. It should only support in the data processing process to help understand what happened in the recorded situation.

The RADAR sensor requires the vehicle velocity $_vv_x$ and the yaw rate $_v\omega_z$ in order to classify the detected objects as standing, stopped, moving or oncoming, as well as for the target selection. Stopped means that the object has moved before it stopped, and standing means that it has never moved during the detection time. The outputs of the RADAR sensor include the kinematic quantities describing the position and relative speed of the objects in the sensor coordinate system, the dimensions and the probability of existence of the detected objects. The RADAR sensor combines the detected reflection points to objects, but errors may occur during this process. The quantity probability of existence p_{ex} describes the likelihood that the detected object actually exists.

To measure the relative distance between the ego and target vehicle, both are equipped with an *Automotive Dynamic Motion Analyser* (ADMA) from Genesys, [Gen13]. It consists of three acceleration sensors, three fibre-optic gyros and a *Global Positioning System* (GPS) receiver with position correction using the *Real-Time Kinematic* (RTK) method, [Gen13]. For position correction, the rough position is sent to a service via a *Global System for Mobile Communications* (GSM) connection. The service has a net of base stations at known coordinates with a distance of about $50\,\mathrm{km}$ between them and generates a virtual base station near the GPS device. There, virtual measurements are generated and sent to the GPS system via GSM. The GPS device is then able to calculate its position with an accuracy of a few centimetres using the RTK method, [Kah06]. This is done in both the ego and the target vehicle. The relative position of the target vehicle to the ego vehicle is calculated in the measurement system, which receives the position of the target vehicle via WLAN connection.
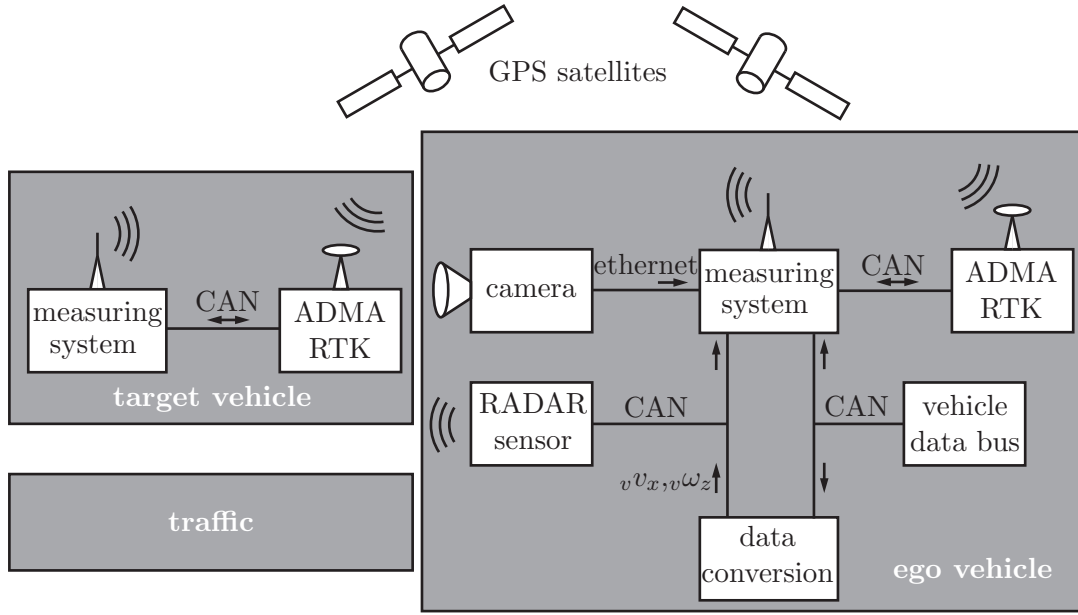
Figure 4.2.: Schematic measurement setup

At the vehicle data bus, many different signals are available (e. g. the steering wheel angle δ_{SW}, the wheel speeds $_cv_x$). Table 4.1 lists the recorded channels and their sources. It should be mentioned that data from the vehicle data bus is not as accurate as data from the ADMA equipment. Therefore, the data from the ADMA serves as an accurate reference measurement system. Figure D.1 in appendix D illustrates the position of the sensors in the ego and target vehicles.

4.2. Side Slip Angle Estimation

One important quantity in vehicle dynamics is the side slip angle β at the CG of the vehicle, which is defined in eq. (B.7). Since it cannot be directly measured, an observer is used to estimate β. The challenge is that the observer should work without measuring the lateral acceleration $_va_y$. In the literature, such as [BCLT08], [ZLC11] and [Kol13], the lateral acceleration is typically used to estimate the lateral tyre forces, which is the input for their vehicle model.

The observer used here is based on the work of Kiencke et al., [KD97]. They use a linear *Single-Track Model* (STM), which is described in eq. (B.8). The output-matrix of the pant representing the measurements reads

$$y = \underbrace{\begin{bmatrix} 0 & 1 \end{bmatrix}}_{\mathbf{c}^{\mathrm{T}}} \mathbf{x}, \tag{4.2}$$

Table 4.1.: Recorded channels

Channel description	Symbol(s)	Source
video data	-	camera
vehicle speed	$_vv_x$	
vehicle yaw rate	$_v\omega_z$	vehicle data bus
wheel speed	$_{clf}v_x,_{crf}v_x,_{crr}v_x,_{clf}v_x$	
steering wheel angle	δ_{SW}	
position of object	$_sx,_sy$	
relative speed of object	$_sv_x,_sv_y$	RADAR sensor
probability of existence of object	p_{ex}	
length, width of object	$_sl,_sw$	
position of target	$_vx,_vy,_vz$	
longitudinal, lateral, vertical speed	$_vv_x,_vv_y,_vv_z$	
longitudinal, lateral, vertical acceleration	$_va_x,_va_y,_va_z$	ADMA
rotational speeds around axis $_vx,_vy,_vz$	$_v\omega_x,_v\omega_y,_v\omega_z$	
relative heading of target to ego	$_v\psi$	
position of the ego vehicle	$_0x,_0y,_0z$	
side slip angle at CG	β	calculated, eq. (4.13)

with $\mathbf{x} = \begin{bmatrix} \beta & _v\omega_z \end{bmatrix}^{\mathrm{T}}$. Föllinger showed in [Föl08] that a single output system is observable if the observability matrix reading

$$\mathbf{Q}_B = \begin{bmatrix} \mathbf{c}^{\mathrm{T}} \\ \mathbf{c}^{\mathrm{T}}\mathbf{A} \\ \vdots \\ \mathbf{c}^{\mathrm{T}}\mathbf{A}^{n-1} \end{bmatrix} \tag{4.3}$$

for a system with the state vector consisting of n components is non-singular, meaning

$$\det \mathbf{Q}_B \neq 0. \tag{4.4}$$

For a more compact notation, the system matrix $\mathbf{A}$ of the linear STM of eq. (B.8) is denoted as

$$\mathbf{A} = \begin{bmatrix} a_{11} & a_{12} \\ a_{21} & a_{22} \end{bmatrix}. \tag{4.5}$$

This leads to a observability matrix of

$$\mathbf{Q}_B = \begin{bmatrix} 0 & 1 \\ a_{21} & a_{22} \end{bmatrix}. \tag{4.6}$$

The requirement described in eq. (4.4) leads to $_rc_y \ l_r \neq \ _fc_y \ l_f$, which is fulfilled for a vehicle in general.

According to [DB06], the estimated state variable $\hat{\mathbf{x}}$ can be determined using the expression

$$\dot{\hat{\mathbf{x}}} = \mathbf{A}\,\hat{\mathbf{x}} + \mathbf{b}\,\delta + \mathbf{L}\left(\underbrace{y - \mathbf{c}^{\mathrm{T}}\,\hat{\mathbf{x}}}_{v\omega_z - v\hat{\omega}_z}\right), \tag{4.7}$$

where $\mathbf{A}$ is the system matrix and $\mathbf{b}$ is the input vector of the system, both of which are described in eq. (B.8). The variable δ is the measured steering angle of the front wheel. The measurement of the vehicle yaw rate is described in eq. (4.2). The vector $\mathbf{L}$ is the observer gain vector that has to be found. For a robust observer, the real part of the poles of the characteristic equation of the observer must be negative. The characteristic equation reads

$$\det\left(\lambda^*\,\mathbf{I} - \left(\mathbf{A} - \mathbf{L}\,\mathbf{c}^{\mathrm{T}}\right)\right) = 0, \tag{4.8}$$

where the vector λ^* consists of the desired Eigenvalues of the observer, and $\mathbf{I}$ is the identity matrix. According to [KD97], the poles are placed at $\lambda^* = \begin{bmatrix} -200 & -2.4\,\frac{{}_fc_y + {}_rc_y}{m\,{}_vv_x} \end{bmatrix}^{\mathrm{T}}$, where ${}_fc_y$ and ${}_rc_y$ are the lateral stiffnesses of one front and one rear wheel including influences of the suspension, m is the vehicle mass, and ${}_vv_x$ is the longitudinal vehicle speed. The vector $\mathbf{L}$ can be determined using the method of Ackermann, [DB06]. The equation reads

$$\mathbf{L} = \left(p_0\,\mathbf{I} + p_1\,\mathbf{A} + \cdots + p_{n-1}\,\mathbf{A}^{n-1} + \mathbf{A}^n\right)\mathbf{Q}_B^{-1}\begin{bmatrix} 0 \\ \vdots \\ 0 \\ 1 \end{bmatrix}, \tag{4.9}$$

where p_i are the coefficients of the desired characteristic polynomial reading

$$p_0 + p_1\,\lambda + \cdots + p_{n-1}\,\lambda^{n-1} + \lambda^n = \prod_{i=1}^{n}\left(\lambda - \lambda_i^*\right). \tag{4.10}$$

For the given system, the observer gain vector results in

$$\mathbf{L} = \begin{bmatrix} \frac{1}{a_{21}}\left(a_{11}^2 + a_{12}a_{21} - a_{11}\left(\lambda_1^* + \lambda_2^*\right) + \lambda_1^*\lambda_2^*\right) \\ a_{11} + a_{22} - \lambda_1^* - \lambda_2^* \end{bmatrix}. \tag{4.11}$$

For a good observer performance, the parameters have to be tuned to achieve a good correlation between the measured and simulated data. In the described algorithm for the side slip angle observer, the tuning parameters are the two constants in the definition of λ^* (200 and 2.4), and the lateral tyre stiffnesses ${}_fc_y$ and ${}_rc_y$. The test vehicle has the same tyres mounted on the front and rear axles. Therefore, the pure tyre stiffness has to be the same for the front and the rear tyres, assuming equal wheel loads. In general, the kinematics and elasto-kinematics of the vehicle suspension make the front tyres steer out of the curve while the rear tyres steer into the curve, thereby producing an understeering behaviour during cornering, [MW04]. This results in a smaller absolute
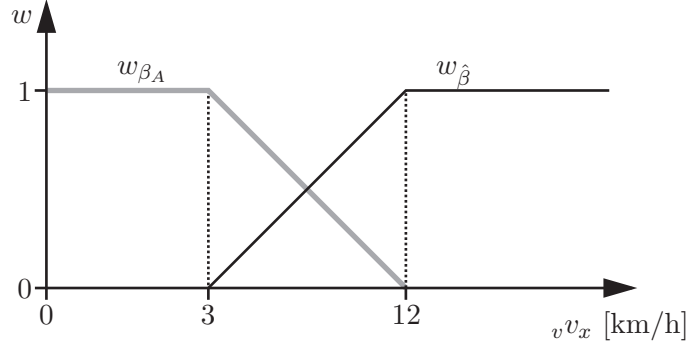
Figure 4.3.: Weight functions w_{β_A} and $w_{\hat{\beta}}$ for the combined side slip angle β

value of the front steering angle δ and a steering of the rear axle towards the inside of the curve. In the model used, the steering angle is not modified, but the lateral tyre stiffness is modified reading $_f c_y = {}_f c_{y,0} - c_{y,e}$ for the front axle, where $_f c_{y,0}$ is the basic cornering stiffness, and $c_{y,e}$ is the influence of the kinematics and elasto-kinematics of the suspension on the cornering stiffness. The same approach is used at the rear axle, but there the basic stiffness is increased by $c_{y,e}$ reading $_r c_y = {}_r c_{y,0} + c_{y,e}$.

The linear STM of eq. (B.8), which is used for the estimation of side slip angle, does not work at $_v v_x = 0$. Therefore, another algorithm is used to find β at low vehicle speeds. It is based on the assumption that at low speeds the side slip angles at the wheels are small, $\alpha_f \ll 1\,\text{rad}$ and $\alpha_r \ll 1\,\text{rad}$. In general, the vehicle moves around the *Instantaneous Centre of Rotation* (ICR). With the assumption of small side slip angles, the ICR has nearly the same position as ICR-A, where A means Ackermann, see fig. B.1. Thus, for low vehicle speeds, the side slip angle is estimated by

$$\beta_A = \arctan\left(\frac{l_r \, \tan\left(\delta\right)}{l_f + l_r}\right). \tag{4.12}$$

The combination of $\hat{\beta}$ and β_A is performed using the velocity-dependent weight function $w\left(_v v_x\right)$ depicted in fig. 4.3. The equation for the combined side slip angle reads

$$\beta = w_{\beta_A} \, \beta_A + w_{\hat{\beta}} \, \hat{\beta}. \tag{4.13}$$

For the validation of the observer, test drives with a specially equipped vehicle were carried out. One additional sensor was mounted at the front bumper of the vehicle, which measures the longitudinal $_v^A v_x$ and lateral speed $_v^A v_y$ in the vehicle coordinate system at sensor position A with its position vector $_v^A \mathbf{s} = \begin{bmatrix} _v^A x & _v^A y \end{bmatrix}^{\mathrm{T}}$ in the vehicle coordinate system. The transformation of the measured speed from the speed sensor point A to the CG is done using

$$_v\mathbf{v} = \begin{bmatrix} _v^A v_x \\ _v^A v_y \\ 0 \end{bmatrix} + \begin{bmatrix} 0 \\ 0 \\ _v\omega_z \end{bmatrix} \times {}_v^A \mathbf{s}, \tag{4.14}$$

Table 4.2.: Test route in and around the city of Graz

Start	End	Overall length [km]	City [%]	Inter-urban [%]	Motorway [%]	Purpose
A	B	9	100	0	0	adaptation to vehicle
B	C	4.4	17	83	0	data recording
C	B	4.4	17	83	0	data recording
B	C	4.4	17	83	0	data recording
C	D	12	0	0	100	data recording
D	A	5.4	100	0	0	data recording

omitting the roll and pitch movement of the vehicle body. Figure 4.4 shows a comparison of this measurement and the observer output illustrating the side slip angle β, the vehicle yaw rate $_v\omega_z$, the steering angle of the front wheel δ, the lateral accelerations $_va_y$ and the vehicle speed $_vv_x$ over time t. The upper two graphs show the measured side slip angle and yaw rate (grey) and the output of the observer (black). It is impressive that the estimation of the side slip angle works very well, even at high accelerations and at combined lateral and longitudinal accelerations.

4.3. Test Drives

The test drives were conducted in and around the city of Graz, Austria. First, test drives without precisely defined routes and no target vehicle were made, which were called the *basic study*. These measurements were made with just two different drives with an overall distance of 139.5 km.

Next, test drives with ten different probands were made, each on a defined route. These tests are called the *proband study*. Figure 4.5 shows an illustration of the route. Each test starts at point A at the Institute of Automotive Engineering of Graz University of Technology. To get familiar with the test vehicle, the probands drive to point B, the church of the village Autal, without recording the data. At B, the data recording starts, and the route leads to point C, Laßnitzhöhe. The probands then drive from C to B, and again from B to C. The next part of the test route goes from Laßnitzhöhe to point D, the motorway exit Graz-Puchwerke using the A2 motorway. From D, the route leads back to A (i. e. the institute) using the L370 and L311 through the city of Graz. This route results in a travelled distance of 16.64 km in the city, 10.96 km inter-urban and 12.00 km on motorways. Each proband travelled a distance of 39.6 km, but only 30.6 km were recorded. This leads to an overall distance of 306.2 km of recorded data. Table 4.2 lists the distribution of city, inter-urban and motorway for the different parts of the route.

Table 4.3 provides an overview of the main parameters of the test drives. At the beginning of the test drives, the probands were asked whether they would describe themselves as *comfort-oriented drivers* or *dynamic drivers*. Two female and ten male drivers drove
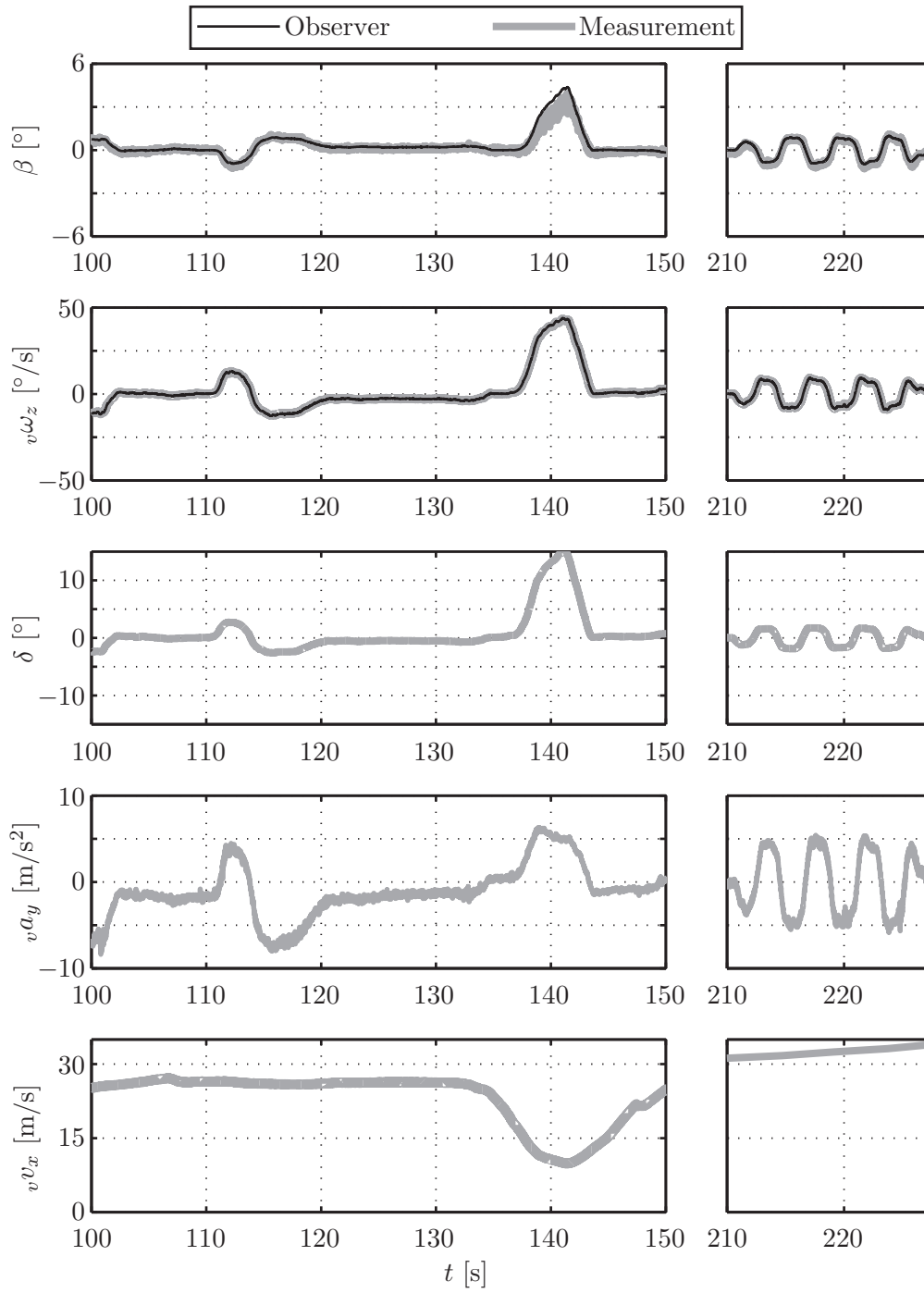
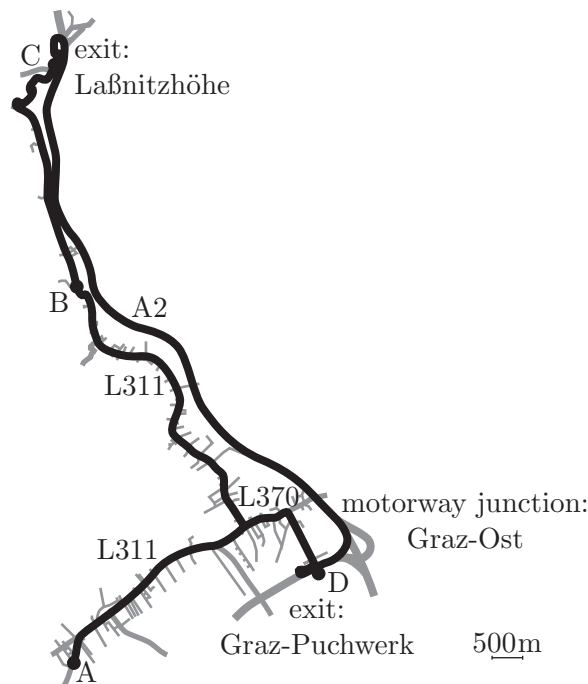Figure 4.4.: Comparison of observer results and measurements

Figure 4.5.: Test route

Table 4.3.: Parameters of the test drives

		Basic study	Proband study	Overall
Distance travelled	[km]	139.2	306.2	445.4
Recorded time	[s]	7922.6	22290.3	30212.9
Mean velocity	[km/h]	63.3	49.5	53.1
Number of drivers	[-]	2	10	12
Mean age of drivers	[year]	34.5	30.9	31.5
Standard deviation of driver age	[year]	6.4	6.5	6.3
Female drivers	[%]	0	30	25
Male drivers	[%]	100	70	75
Comfort-oriented driving style	[%]	50	70	67
Dynamic driving style	[%]	50	30	33

the tests, with a mean age of 31.5 and a standard deviation of 6.3 years. Overall, a distance of 445.4 km was recorded, with a mean velocity of 53.1 km/h. Figure 4.6(b) shows the histogram of the longitudinal vehicle speed for all the measurements. It can be seen that there is a peak at the speed range of 0 to 10 km/h and at 40 to 50 km/h. As already mentioned in table 4.3, the mean velocity is 53.1 m/s.

Figure 4.6(a) shows that the acceleration density is higher for pure longitudinal or lateral accelerations. This result is comparable to the results of Wegscheider, [Weg09]. The
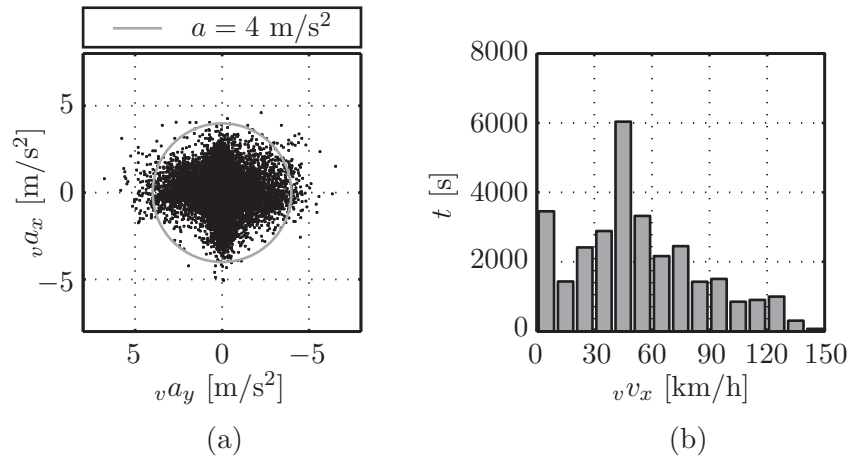
Figure 4.6.: (a) Combined longitudinal and lateral accelerations and (b) velocity distribution for the measurements of the basic and the proband studies

combined longitudinal and lateral accelerations read $a = \sqrt{{}_v a_x^2 + {}_v a_y^2}$. The share of 99.26 % of the combined accelerations fulfil the condition $a \leq 4\,\text{m/s}^2$ which is depicted as the grey circle in fig. 4.6(a). The limit was chosen with respect to simplification number 3 of the linear STM on page 97. The large amount of the measurements fulfilling this limit shows that nearly all accelerations are within the linear range of the tyre characteristics, see linear area near the origin in fig. B.2(a).

5

Selection of the Object to Follow

One of the main challenges in designing *Adaptive Cruise Control* (ACC) systems is to find a reliable algorithm for the selection of the target, the *Object to Follow* (OTF). For this task, the ACC system has to predict the ego vehicle path with the available sensor information. Based on the predicted trajectory, the OTF is selected. For this chapter, simple algorithms were chosen intentionally. Despite their simplicity, they lead to good outputs.

5.1. Path Prediction

This chapter describes different state-of-the-art path prediction algorithms and evaluates them based on the measurements made in chapter 4.

The path prediction must be performed using the sensor data that is available in the vehicle. Caveney uses digital maps that deliver the expected road curvature, [Cav09]. This data is used in combination with the dynamic state of the vehicle to predict the vehicle path. Since these maps are not currently available for all roads, they were not used in this investigation. Additionally, the use of digital maps may pose a problem at locations where the vehicle localization does not work (e. g. in tunnels or in cities, where the high buildings obscure the *Global Navigation Satellite System* (GNSS) satellites). In such locations, other technologies such as *Vehicle-to-Vehicle Communication* (V2V) or *Vehicle-to-Infrastructure Communication* (V2I) may be used to obtain the necessary data. Another approach was used by Yim et al. in [YSZS10]. They described a system in which the information is stored in the lane markings as binary code and is detected

by the camera mounted in the vehicle. They demonstrated that this method even works at high vehicle speeds.

Another approach is to use additional environmental-recognition sensors, such as camera systems, to detect the lane markings on the road, [WDS09]. This works properly if the vehicle is not changing lanes and if simple situations concerning the lane markings occur. For camera systems, it is very difficult to detect which lane the vehicle is driving in when more potential possible solutions can be found (e.g. at road construction zones or at road intersections). To handle such situations, the work of Yim et al. could also be used, [YSZS10]. In general, direct measurement of the lane markings places high demands on the accuracy of the optical system. Additionally, detecting the ego vehicle driver's intention to change lanes by sensing the indicator usage will help to increase the quality of the predicted path. This could also be done for vehicles travelling in front of the ego vehicle, and the data could be sent to the ego vehicle via V2V technologies or by analysing the video data recorded by the camera. The ability to detect the front vehicle's intention to change lanes via camera strongly depends on how often the front vehicle's turn signal flashes. The research of Fröhlich et al. in [FEF14] showed that if the turn signals flashes at least three times, the system generates very reliable information, with a very low number of wrong detections. In modern vehicles, the indicator flashes three times even if it is activated by the driver for a very short time. This function is called *one-touch indicator* and helps to fulfil the requirements of Fröhlich et al..

These are all promising technologies, [WDS09], but for the current investigations, they were excluded to reduce the complexity of the system. In this chapter, the described algorithms are based on vehicle dynamics data, which is available in every modern vehicle equipped with an *Electronic Stability Control* (ESC) system.

5.1.1. Path Prediction Using Constant Curvature Hypothesis

The *Constant Curvature Hypothesis* predicts the vehicle path based on the assumption that the corner radius the vehicle is driving will remain constant in the future, [WDS09]. For the present model, the radius is not used because the radius for straight driving runs towards infinity. Instead, the reciprocal value, called curvature, $\kappa = \frac{1}{R}$ is used. The radius R is the distance between the vehicle's *Center of Gravity* (CG) and the *Instantaneous Centre of Rotation* (ICR), see fig. 5.1. The following paragraphs describe how to estimate the actual curvature. All algorithms use the assumption that only small lateral velocities occur $_v v_y \ll 1\,\text{m/s}$, resulting in $_v v_x \approx \,_v v$.

In [WDS09], Winner et al. showed that the curvature can be estimated by

$$\kappa_{\omega_z} = \frac{_v \omega_z}{_v v_x} \tag{5.1}$$

at higher vehicle speeds.

Another approach described by Winner in [WDS09] based on the lateral acceleration $_v a_y$
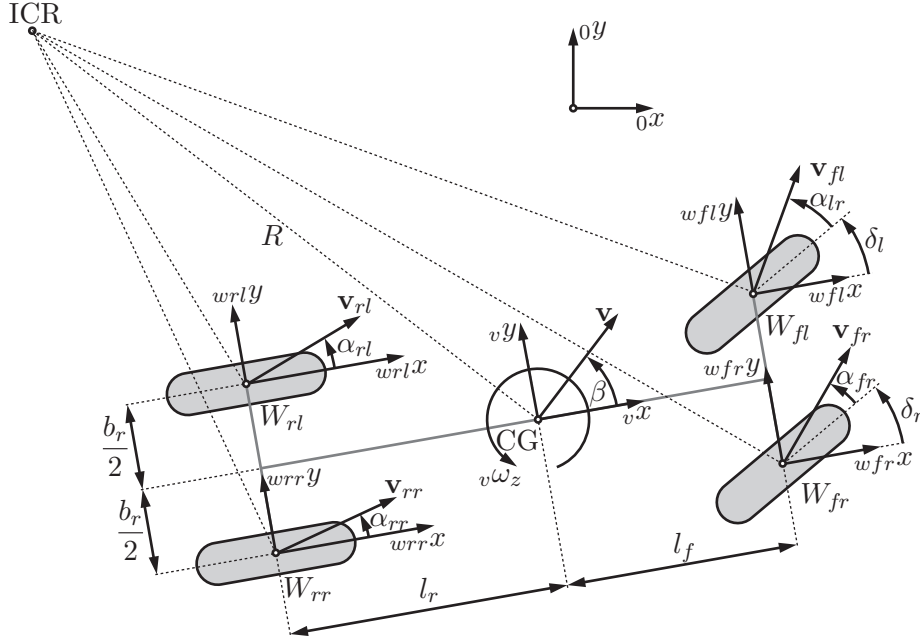
Figure 5.1.: Coordinate systems at all four wheels of the vehicle

reads

$$\kappa_{a_y} = \frac{_v a_y}{_v v_x^2}. \tag{5.2}$$

If the wheel speeds are available, the curvature can be estimated using the difference between the wheel speeds of the left and right wheel at a non-driven axle. This method only works if the longitudinal slip and the side slip angle at the considered wheels are small. Figure 5.1 shows the speeds at the four wheel points and the corresponding coordinate systems. Assuming small side slip angles, the speeds at the wheel points equal the speed in the x-direction of the corresponding coordinate system, e.g. $\alpha_{rl} \ll 1\,\mathrm{rad}$ leads to $\|\mathbf{v}_{rl}\| \approx {_{wrl}v_x}$. The longitudinal speeds of the rear wheels and the CG read

$$_{wrl}v_x = {_v v_x} - \frac{b_r}{2}{_v\omega_z}, \tag{5.3}$$

$$_{wrr}v_x = {_v v_x} + \frac{b_r}{2}{_v\omega_z} \text{ and} \tag{5.4}$$

$$_v v_x = R\,{_v\omega_z}. \tag{5.5}$$

The variables $_{wrl}v_x$ and $_{wrr}v_x$ are the longitudinal speeds at the W_{rl} and W_{rr}-points, $_v v_x$ is the longitudinal vehicle speed at CG, $_v\omega_z$ is the yaw rate of the vehicle, and b_r is the track width at the rear axle, which is the non-driven axle. Solving eqs. (5.3) to (5.5) for $\frac{1}{R}$ leads to

$$\kappa_{\Delta v} = \frac{2\left(_{wrl}v_x - {_{wrr}v_x}\right)}{b_r\left(_{wrl}v_x + {_{wrr}v_x}\right)}. \tag{5.6}$$

Table 5.1.: Comparison of the different curvature estimation algorithms according to [WDS09]

Situation	κ_{ω_z}	κ_{a_y}	$\kappa_{\Delta v}$	κ_δ
Robust at low vehicle speeds	$\circ$	$--$	$-$	$++$
Robust at high vehicle speeds	$\circ$	$++$	$-$	$-$

Another possible way to calculate the curvature is to use the linear *Single-Track Model* (STM), as described in appendix B.1. According to [HW10], the required lateral tyre forces can be calculated out of the second and third line of eq. (B.1) for quasistatic cornering when $_v\omega_z = \frac{vv}{R}$. Due to simplifications 3 and 4 in appendix B.1, eq. (B.2) can be rewritten as

$$_{wf}F_y = -_fc_y\left(-\delta + \beta + \frac{l_f}{R}\right) \tag{5.7}$$

for the front tyres and

$$_{wr}F_y = -_rc_y\left(\beta - \frac{l_r}{R}\right) \tag{5.8}$$

for the rear tyres. Therefore, the required steering angle δ for a given vehicle speed $_vv$ can be calculated using

$$\delta\left(_vv\right) = \underbrace{\frac{l_f + l_r}{R}}_{\delta_A} + \frac{m\,_vv^2}{(l_f + l_r)R}\left(\frac{l_r}{2_fc_y} - \frac{l_f}{2_rc_y}\right), \tag{5.9}$$

where δ_A is the linearisation of the Ackermann steering angle describing the steering angle at low speeds, when the vehicle moves around ICR-A. According to [WDS09], eq. (5.9) can be solved to

$$\kappa_\delta = \frac{\delta}{\left(l_f + l_r + \frac{m\,v_x^2}{l_f+l_r}\left(\frac{l_r}{2_fc_y} - \frac{l_f}{2_rc_y}\right)\right)}. \tag{5.10}$$

Table 5.1 shows a comparison of the different algorithms described in eqs. (5.1), (5.2), (5.10) and (5.10) and evaluates them for high and low vehicle speeds. Since the selected algorithm should work in both speed ranges, the algorithm based on the yaw rate described in eq. (5.1) is the best compromise.

For a given curvature, the predicted trajectory should be calculated in the vehicle coordinate system at time step k, $(_{vk}x, _{vk}y)$. To this end, two different approaches are available. The first one, described in [WDS09], is to calculate the trajectory using the parabola

$$_\beta\hat{y} = \frac{\kappa}{2}d^2, \tag{5.11}$$

where $_\beta\hat{y}$ is the y-coordinate of the trajectory at a given distance $d = \sqrt{_\beta\hat{x}^2 + _\beta\hat{y}^2}$ in the $(_\beta x, _\beta y)$-coordinate system. Figure 5.2 shows the newly introduced $(_\beta x, _\beta y)$-coordinate

system, which has its origin at CG and its $_\beta x$ axis parallel to the speed vector $\mathbf{v}_k$ in the CG. The transformation from the $(_\beta x, {}_\beta y)$ to the vehicle coordinate system at time step k is done using

$$\begin{bmatrix} _{vk}\hat{x} \\ _{vk}\hat{y} \end{bmatrix} = \underbrace{\begin{bmatrix} \cos\beta & -\sin\beta \\ \sin\beta & \cos\beta \end{bmatrix}}_{\mathbf{T}_{vk,\beta}} \begin{bmatrix} _\beta\hat{x} \\ _\beta\hat{y} \end{bmatrix}. \tag{5.12}$$

The second option is to estimate the trajectory using a circle reading

$$_\beta\hat{x}^2 + \left(_\beta\hat{y} - \frac{1}{\kappa}\right)^2 = \frac{1}{\kappa^2}. \tag{5.13}$$

The circle has its centre at $_\beta x = 0$ and $_\beta y = \frac{1}{\kappa}$ with the radius $R = \frac{1}{\kappa}$.

Figure 5.2 illustrates the differences between eqs. (5.11) and (5.13). The big advantage of the parabola (black dashed) is that every $_\beta\hat{x}$ coordinate has its $_\beta\hat{y}$ coordinate. For the circle (grey), eq. (5.13) could only be solved for $-\frac{1}{\kappa} \leq {}_\beta\hat{x} \leq \frac{1}{\kappa}$. For the transformation from the $(_\beta x, {}_\beta y)$ to the $(_{vk} x, {}_{vk} y)$-coordinate system, eq. (5.12) is also used for the circle.

5.1.2. Path Prediction Using Linear Single-Track Model

For the prediction of the trajectory, the linear STM described in eq. (B.8) is used. The prediction is done at time step t_k, and the output is a number of i predicted state vectors $\hat{\mathbf{x}}_{i|k} = \begin{bmatrix} \hat{\beta}_{i|k} & _v\hat{\omega}_{z,i|k} \end{bmatrix}^\mathrm{T}$. The index k means that the prediction is done at time t_k, and i indicates the i-th time step within the prediction. The steering angle δ_k is held constant for the whole simulation. The initial condition for the integration reads $\mathbf{x}_{0|k} = \begin{bmatrix} \beta_k & _v\omega_{z,k} \end{bmatrix}^\mathrm{T}$, where β_k is the estimated side slip angle at time t_k, as described in chapter 4.2, and $_v\omega_{z,k}$ is the measured yaw rate. The lateral vehicle speed is predicted as

$$_v\hat{v}_{y,i|k} = {}_v v_{x,k} \tan\left(\hat{\beta}_{i|k}\right), \tag{5.14}$$

where $_v v_{x,k}$ is the measured longitudinal vehicle speed at t_k. The heading of the vehicle can be found using

$$_{vk}\hat{\psi}_{i|k} = \int\limits_{t_k}^{t_k+i\Delta t} {}_v\hat{\omega}_{z,i|k} \, dt, \tag{5.15}$$

where the index vk means the vehicle coordinate system at time step k, and Δt is the time step size for the prediction. The transformation of the other state variables is done using the expression

$$\begin{bmatrix} _{vk}\dot{\hat{x}}_{i|k} \\ _{vk}\dot{\hat{y}}_{i|k} \end{bmatrix} = \begin{bmatrix} \cos\left(_{vk}\hat{\psi}_{i|k}\right) & -\sin\left(_{vk}\hat{\psi}_{i|k}\right) \\ \sin\left(_{vk}\hat{\psi}_{i|k}\right) & \cos\left(_{vk}\hat{\psi}_{i|k}\right) \end{bmatrix} \begin{bmatrix} _v v_{x,k} \\ _v\hat{v}_{y,i|k} \end{bmatrix}. \tag{5.16}$$
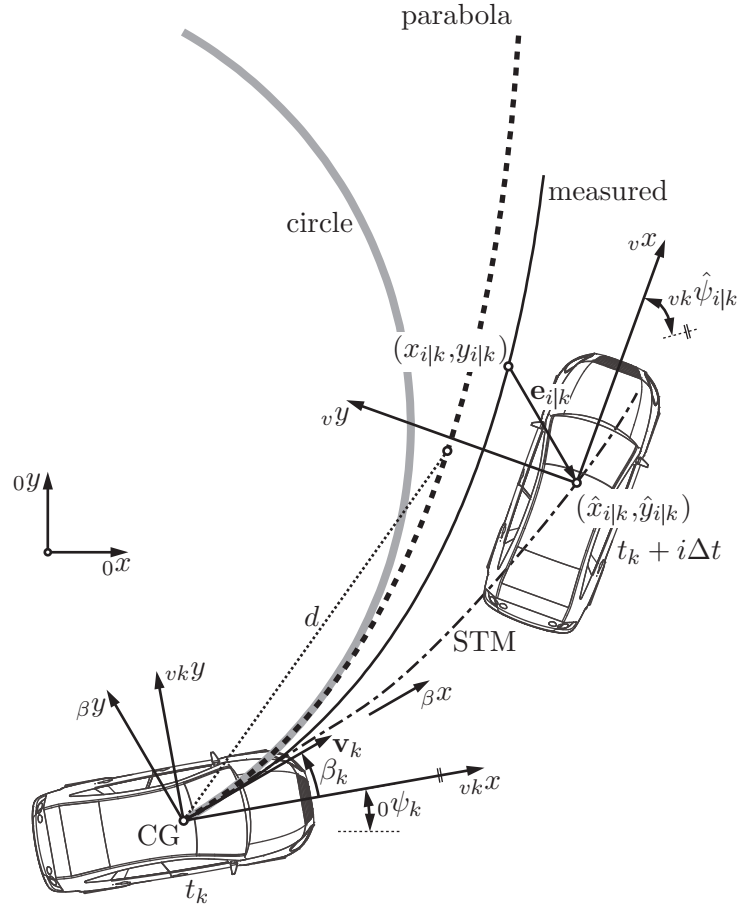
Figure 5.2.: Estimated trajectories using a parabola, a circle, a linear STM and the measured path at the initial time t_k and at time $t_k + i\Delta t$

For the predicted trajectory in the vehicle coordinate system at time step k, the integration

$$\begin{bmatrix} vk\hat{x}_{i|k} \\ vk\hat{y}_{i|k} \end{bmatrix} = \int\limits_{t_k}^{t_k+i\Delta t} \begin{bmatrix} vk\dot{\hat{x}}_{i|k} \\ vk\dot{\hat{y}}_{i|k} \end{bmatrix} \, dt \tag{5.17}$$

has to be solved.

5.1.3. Path Prediction the Using Non-Constant Steering Angle Hypothesis

The *Non-Constant Steering Angle Hypothesis* uses the vehicle model described in chapter 5.1.2. The only difference from the prediction algorithm of chapter 5.1.2 is that the steering angle δ, which is the input for the linear STM, is not constant. It is predicted

as

$$
\delta_{i|k}\left(i\right) = \begin{cases} \delta_k \, \mathrm{e}^{\frac{\dot{\delta}_k}{\delta_k} i \Delta t} & \text{for} \ \ \dot{\delta}_k \, \delta_k \leq 0 \text{ and} \\ \delta_k \left[1 + q \left(1 - \mathrm{e}^{-\frac{\dot{\delta}_k}{q \, \delta_k} i \Delta t} \right) \right] & \text{for} \ \ \dot{\delta}_k \, \delta_k > 0, \end{cases} \tag{5.18}
$$

where q is a tuning parameter. The condition $\dot{\delta}_k \, \delta_k \leq 0$ means that the steering wheel angle δ_k and its velocity $\dot{\delta}_k$ have opposite signs. This could be interpreted as "*steering out of the corner*". The other condition $\dot{\delta}_k \, \delta_k > 0$ means that both quantities have the same sign, meaning "*steering in the corner*". For long prediction horizons, meaning the limit $i \to \infty$, the function values read

$$
\lim_{i \to \infty} \delta_{i|k} = \begin{cases} 0 & \text{for} \ \ \dot{\delta}_k \, \delta_k \leq 0 \text{ and} \\ (1 + q) \, \delta_k & \text{for} \ \ \dot{\delta}_k \, \delta_k > 0. \end{cases} \tag{5.19}
$$

In eq. (5.19) it can be seen that q scales the maximum value of the steering angle. Aditionally, eq. (5.18) ensures a smooth transition from the measured to the predicted values for δ and $\dot{\delta}$, meaning for $i = 0$, $\delta_{0|k} = \delta_k$ and $\dot{\delta}_{0|k} = \dot{\delta}_k$. Figure 5.3 shows an example of a measurement for the steering wheel angle δ_{SW} and the steering wheel velocity $\dot{\delta}_{SW}$. Both graphs show the measurement until the time $t_k = 56 \, \mathrm{s}$ as solid black graphs and the predicted values in grey. Additionally, the future measurements are displayed as dashed graphs. However, at the time of the prediction, they were not available. It is impressive that the predicted values for δ and $\dot{\delta}$ seem to be a good input for the algorithm. In chapter 5.1.2, the input for the linear STM is the steering wheel angle δ_k for the whole path prediction. In comparison, the predicted values depicted in fig. 5.3 match the measured data very well, which leads to the conclusion that the prediction algorithm for the steering wheel angle delivers good results. If the parameter q of eq. (5.18) is set to small values, then the steering angle will stay nearly constant for the case $\dot{\delta}_k \, \delta_k > 0$. For $q = 0.05$, it will only increase $5\,\%$ from the initial value of δ_k, for the limit $i \to \infty$. The parameter q has to be found iteratively with simulations, which shows that low values give the best results.

5.1.4. Evaluation of Path Prediction Algorithms

To evaluate the different path prediction algorithms, the predicted trajectory has to be transformed into the global coordinate system. The transformation reads

$$
\underbrace{\begin{bmatrix} {}_0\hat{x}_{i|k} \\ {}_0\hat{y}_{i|k} \\ {}_0\hat{\psi}_{i|k} \end{bmatrix}}_{{}_0\hat{\mathbf{z}}_{i|k}} = \underbrace{\begin{bmatrix} {}_0 x_k \\ {}_0 y_k \\ {}_0 \psi_k \end{bmatrix}}_{{}_0\mathbf{z}_k} + \begin{bmatrix} \cos\left({}_0\psi_k\right) & -\sin\left({}_0\psi_k\right) & 0 \\ \sin\left({}_0\psi_k\right) & \cos\left({}_0\psi_k\right) & 0 \\ 0 & & 1 \end{bmatrix} \underbrace{\begin{bmatrix} {}_{vk}\hat{x}_{i|k} \\ {}_{vk}\hat{y}_{i|k} \\ {}_{vk}\hat{\psi}_{i|k} \end{bmatrix}}_{{}_{vk}\hat{\mathbf{z}}_{i|k}} +, \tag{5.20}
$$

where ${}_0\psi_k$ is the vehicle heading in the global coordinate system at time t_k, as illustrated in fig. 5.2. The vector ${}_0\hat{\mathbf{z}}_{i|k}$ describes the predicted position and orientation of the vehicle
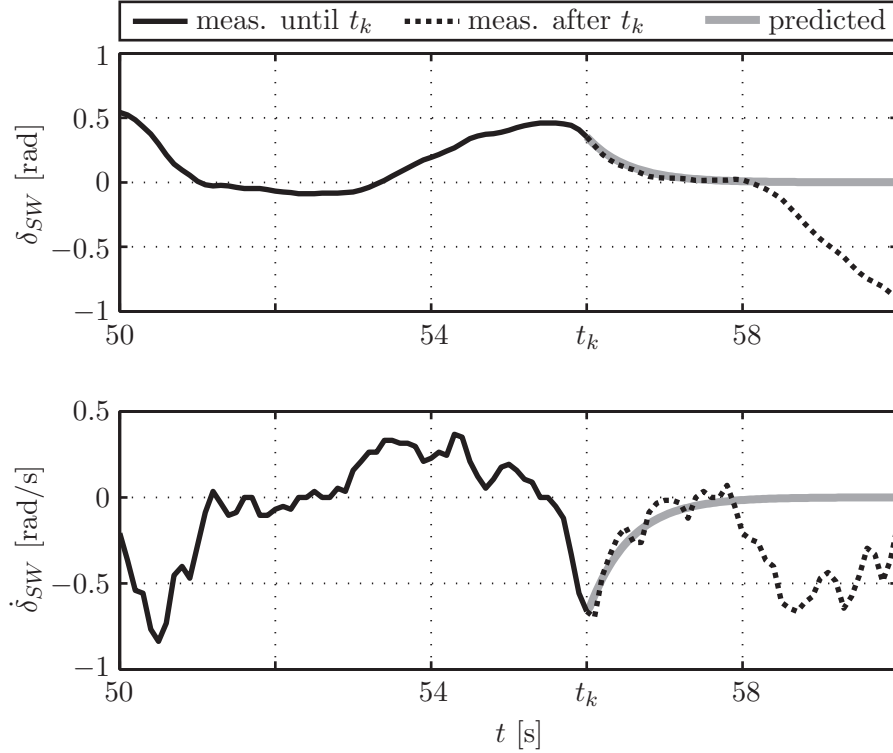
Figure 5.3.: Steering wheel angle δ_{SW} and steering wheel velocity $\dot{\delta}_{SW}$ measurements and predicted values

in the global coordinate system at time $t_k + i\Delta t$, the vector $_0\mathbf{z}_k$ is the position and orientation the the beginning of the prediction at time t_k, and the vector $_{vk}\hat{\mathbf{z}}_{i|k}$ is the predicted path in the vehicle coordinate system at time step k for the i-th predicted time step.

To evaluate the algorithms, the error vector between measurement and predicted trajectory is defined as

$$\mathbf{e}_{i|k} = \begin{bmatrix} _0x_{i|k} \\ _0y_{i|k} \end{bmatrix} - \begin{bmatrix} _0\hat{x}_{i|k} \\ _0\hat{y}_{i|k} \end{bmatrix}, \tag{5.21}$$

with its norm reading

$$e_{i|k} = \sqrt{\mathbf{e}_{i|k}^{\mathrm{T}}\mathbf{e}_{i|k}}. \tag{5.22}$$

For a more compact notation, all the i norms of the error vectors of the prediction performed at time t_k are combined to form the error vector

$$\mathbf{e}_k = \begin{bmatrix} e_{1|k} \\ e_{2|k} \\ \vdots \\ e_{n_k|k} \end{bmatrix}, \tag{5.23}$$

Table 5.2.: Evaluation of different path prediction algorithms

$n_k \Delta t$ [s]	J_{par} [m]	J_{cir} [m]	J_{STM} [m]	J_{STS} [m]
3	11.9388	11.9492	11.8913	11.8222
10	26.0606	26.1204	26.3586	25.5326

where n_k is the number of predictions done at t_k, meaning the number of i. All these $\mathbf{e}_k$ form the error vector reading

$$\mathbf{e} = \begin{bmatrix} \mathbf{e}_1 \\ \mathbf{e}_2 \\ \vdots \\ \mathbf{e}_N \end{bmatrix}, \tag{5.24}$$

where N is the number of time steps when the prediction is done, meaning the number of t_k. The vector $\mathbf{e}$ has a length of

$$p = \sum_{k=1}^{N} n_k, \tag{5.25}$$

which is equivalent to the number of errors used in the investigation. The evaluation is done with the cost function, which is defined as

$$J = \frac{1}{p} \sum_{k=1}^{N} \sum_{i=1}^{n_k} e_{i|k}. \tag{5.26}$$

It can be interpreted as the mean value of the distances between the measured and predicted trajectories for n_k predictions at N different time steps.

The comparison is done for four path prediction algorithms. The first one uses the curvature calculated by eq. (5.1) and predictes the path using eq. (5.11). The resulting cost function is called J_{par}. The second one uses the same curvature but estimates the path with eq. (5.13), leading to a cost function named J_{cir}. The third evaluation is done with the linear STM described in chapter 5.1.2, with its cost function J_{STM}. The last evaluation is based on the hypothesis described in chapter 5.1.3. Its cost function is called J_{STS}. The evaluation was done for two different prediction horizons. The first one was set to $n_k \Delta t = 3$ s, and the second one to $n_k \Delta t = 10$ s, with the corresponding prediction distances $s_{n_k} = {}_v v_x\, n_k \Delta t$. For low vehicle speeds, the prediction distance was limited to a minimum of $s_{min} = 10$ m, and for high speeds to $s_{max} = 150$ m. The upper limit was set with respect to the maximum detection range of the environmental-recognition sensor. The number of predictions at t_k was set to $p_k = 100$. This results in the evaluation of about $p = 28.5\ 10^6$ points for both cases. Table 5.2 shows the results for the two cases.

5.2. Natural Coordinates

This chapter introduces natural coordinates that are beneficial in the mathematical treatment of the object selection algorithms in chapter 5.3.

For the selection of the OTF, the position of each object relative to the predicted path has to be found. Figure 5.4 illustrates a situation with two target objects, a truck and a car. The reference point is measured by the *Radio Detection and Ranging* (RADAR) sensor in the sensor coordinate system with the position vector $_s\mathbf{s}_j = \begin{bmatrix} _sx_j & _sy_j \end{bmatrix}^\mathrm{T}$ for the j-th object. The same point has the coordinates $_n\mathbf{s}_j = \begin{bmatrix} s_j & u_j \end{bmatrix}^\mathrm{T}$ in the natural coordinate system (s, u) with its origin in the CG of the ego vehicle. The s-component is measured along the predicted path, and the u-component is measured perpendicular to the predicted path. In general, the predicted path is given with a number of i points in the vehicle coordinate system.

Figure 5.5 illustrates the predicted path at time t_k with four points $\left(\hat{x}_{i-1|k}, \hat{y}_{i-1|k}\right)$ to $\left(\hat{x}_{i+2|k}, \hat{y}_{i+2|k}\right)$ and three measured points $(_vx_j, _vy_j)$, $(_vx_r, _vy_r)$ and $(_vx_t, _vy_t)$ in the vehicle coordinate system. For the calculation of the natural coordinates of that point, the point $(_vx_{q,j}, _vy_{q,j})$ has to be found first. In the presented case, it does not matter if the calculation is done in the vehicle, sensor or global coordinate system. Hence, the index for the coordinate system is left for further considerations. The equations for two straight lines are set up that read

$$\sigma_i: \begin{bmatrix} x_{q,j} \\ y_{q,j} \end{bmatrix} = \begin{bmatrix} \hat{x}_{i|k} \\ \hat{y}_{i|k} \end{bmatrix} + k_{i,j}\, \mathbf{p_i} \text{ and} \tag{5.27}$$

$$\eta_i: \begin{bmatrix} x_{q,j} \\ y_{q,j} \end{bmatrix} = \begin{bmatrix} x_1 \\ y_1 \end{bmatrix} + m_{i,j}\, \mathbf{n_i}, \tag{5.28}$$

where the scalar quantities $k_{i,j}$ and $m_{i,j}$ are the unknowns. The straight line σ_i is parallel to the longitudinal coordinate for the i-th path element, and η_i corresponds to the lateral coordinate. The vectors $\mathbf{p}_i$ and $\mathbf{n}_i$ are defined by

$$\mathbf{p}_i = \begin{bmatrix} p_{i,x} \\ p_{i,y} \end{bmatrix} = \begin{bmatrix} \hat{x}_{i+1|k} - \hat{x}_{i|k} \\ \hat{y}_{i+1|k} - \hat{y}_{i|k} \end{bmatrix} \text{ and} \tag{5.29}$$

$$\mathbf{n}_i = \begin{bmatrix} -p_{i,y} \\ p_{i,x} \end{bmatrix}. \tag{5.30}$$

Equations (5.27) to (5.30) can be solved for $k_{i,j}$. If $k_{i,j} \in [0, 1]$, then the coordinates $(x_{q,j}, y_{q,j})$ could be found using eq. (5.27). The lateral distance to the path reads

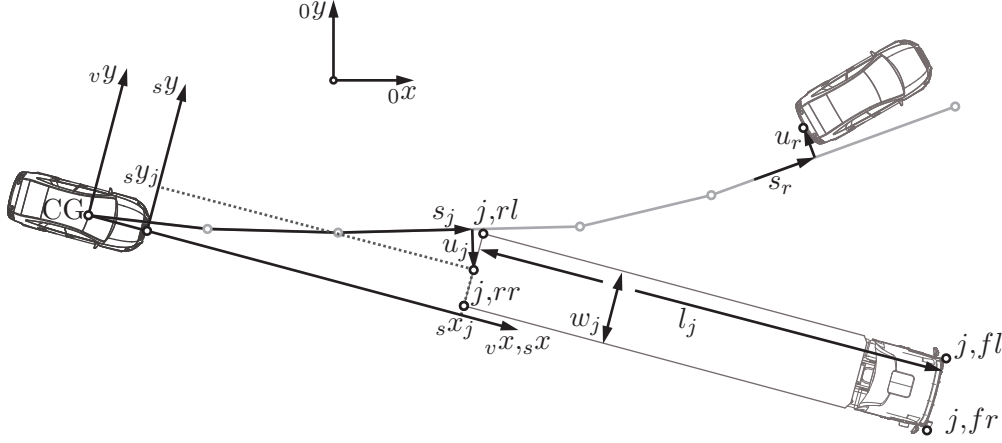$$d_j = \sqrt{(x_j - x_{q,j})^2 + (y_j - y_{q,j})^2}. \tag{5.31}$$

Figure 5.4.: Natural coordinates

The sign of u_j can be found using

$$u_j = d_j \qquad \text{for} \qquad \mathbf{n}_i^{\mathrm{T}} \begin{bmatrix} x_j - x_{q,j} \\ y_j - y_{q,j} \end{bmatrix} > 0 \text{ and} \tag{5.32}$$

$$u_j = -d_j \qquad \text{for} \qquad \mathbf{n}_i^{\mathrm{T}} \begin{bmatrix} x_j - x_{q,j} \\ y_j - y_{q,j} \end{bmatrix} < 0. \tag{5.33}$$

The condition in eq. (5.32) shows that the vector $\mathbf{n}_i$ and the vector from the point $(x_{q,j}, y_{q,j})$ to (x_j, y_j) have the same direction, while in the condition of eq. (5.33) they have opposite directions. In the example given in fig. 5.4, the lateral coordinates are $u_j < 0$ and $u_r > 0$. The longitudinal coordinate s_j is the distance along the predicted path from CG to the point $(x_{q,j}, y_{q,j})$. There is a special case if $k_{i,r} > 1$ and $k_{i+1,t} < 1$, see points (x_r, y_r) and (x_t, y_t) in fig. 5.5. For this case, the coordinates are found using $k_{i,r} = 1$ for the point (x_r, y_r) and $k_{i+1,t} = 0$ for the point (x_t, y_t), if the points are within the left part of the grey marked area. Using $k_{i+1,t} = 0$ means that the straight lines σ_{i+1} and η_{i+1} are used to find the coordinates for the point (x_t, y_t). To check if the points are within the grey area, the angle between the i-th and $i + 1$-th trajectory segment have to be found using

$$\alpha_i = \arccos\left(\frac{\mathbf{p}_i^{\mathrm{T}} \mathbf{p}_{i+1}}{\|\mathbf{p}_i\| \|\mathbf{p}_{i+1}\|}\right). \tag{5.34}$$

The following conditions describe how to choose whether the point is in the left part of the grey area or in the right part.

$$\arctan\left(\frac{(k_{i,r} - 1) \|\mathbf{p}_i\|}{|u_r|}\right) < \frac{\alpha_i}{2} \tag{5.35}$$

leads to the left part, and

$$\arctan\left(\frac{-k_{i+1,t} \|\mathbf{p}_{i+1}\|}{|u_t|}\right) < \frac{\alpha_i}{2} \tag{5.36}$$
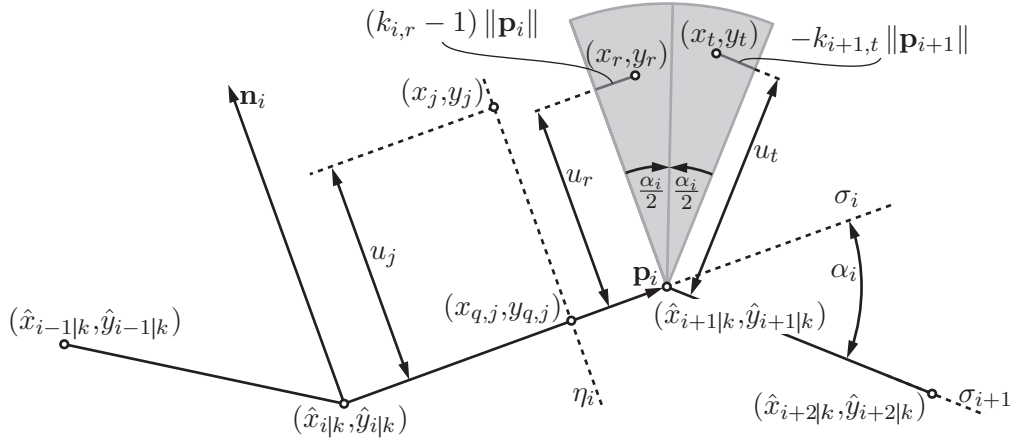
Figure 5.5.: Calculation of natural coordinates

leads to the right part.

Figure 5.4 shows that the RADAR sensor estimates the width w_j and length l_j of all the measured objects. For further investigations, each object is represented as a list of four points that read

$$_s\mathbf{s}_{j,fl} = \begin{bmatrix} _sx_j + l_j \\ _sy_j + \frac{w_j}{2} \end{bmatrix}, \qquad _s\mathbf{s}_{j,fr} = \begin{bmatrix} _sx_j + l_j \\ _sy_j - \frac{w_j}{2} \end{bmatrix},$$

$$_s\mathbf{s}_{j,rl} = \begin{bmatrix} _sx_j \\ _sy_j + \frac{w_j}{2} \end{bmatrix} \text{and } _s\mathbf{s}_{j,rr} = \begin{bmatrix} _sx_j \\ _sy_j - \frac{w_j}{2} \end{bmatrix}, \tag{5.37}$$

as illustrated in fig. 5.4.

5.3. Object Selection

The selection of the right OTF strongly depends on the accuracy of the predicted path, the accuracy of the position of the detected objects and their predicted paths. Chapters 5.3.1 and 5.3.2 give examples for two different object selection algorithms.

5.3.1. In-Path Algorithm

With the *In-Path Algorithm*, the nearest object in the predicted path is selected as the OTF. Therefore, the predicted trajectory is superimposed by a path with a certain width. Chapters 5.3.1.1 and 5.3.1.2 describe two different path width algorithms in detail.

5.3.1.1. Constant Path Width

With the *Constant Path Width Algorithm*, the trajectory is superimposed by a path with a constant width of b_0, which is the simplest way to describe the predicted path, [WDS09]. A point is within the path if the condition

$$|u_j| \leq b_0 \tag{5.38}$$

is fulfilled, where u_j is the lateral coordinate of the point in the natural coordinate system.

As already mentioned in eq. (5.37), an object is represented by a list of four points. There is a special case if a number of the points are outside the left path boundary and the rest of the points are outside the right boundary, e. g.

$$|u_{j,fl}| > b_0, \qquad |u_{j,fr}| > b_0, \qquad |u_{j,rl}| > b_0 \text{ and } \qquad |u_{j,rr}| > b_0 \text{ with}$$
$$u_{j,fl} < 0, \qquad u_{j,fr} < 0, \qquad u_{j,rl} > 0 \text{ and } \qquad u_{j,rr} > 0. \tag{5.39}$$

Figure 5.6(a) gives an example of the special case of eq. (5.39). In such cases, an additional fifth point is added to the list of eq. (5.37) reading

$$_n\mathbf{s}_{j,5} = \begin{bmatrix} \min\left(s_{j,fl}, s_{j,fr}, s_{j,rl}, s_{j,rr}\right) \\ 0 \end{bmatrix}, \tag{5.40}$$

which can be described as the point with the minimum s-coordinate of the other four points and a zero u-coordinate in the natural coordinate system, see fig. 5.6(a). In this case, object j is in the predicted path. The OTF is the object with the smallest s-coordinate in the predicted path.

5.3.1.2. Non-Constant Path Width

Another option is to use a *Non-Constant Path Width*, which should compensate for errors in the path prediction, [WDS09]. The function used is a polynomial of second order which reads

$$b\left(s\right) = a_1\,s^2 + a_2\,s + a_3, \tag{5.41}$$

where the coefficients a_1 to a_3 could be found using the definitions

$$\begin{aligned} b\left(0\right) &= b_0, \\ b\left(s_{max}\right) &= b_{max} \text{ and} \\ \left.\frac{db}{ds}\right|_{s_{max}} &= 0. \end{aligned} \tag{5.42}$$

Figure 5.6(b) gives an example of $b\left(s\right)$ for the parameters $b_0 = 2.2\,\text{m}$, $b_{max} = 3\,\text{m}$ and $s_{max} = 45\,\text{m}$. As shown in chapter 5.3.1.1, the OTF contains the point with the minimum s-coordinate fulfilling the condition $|u_j| < b\left(s\right)$.
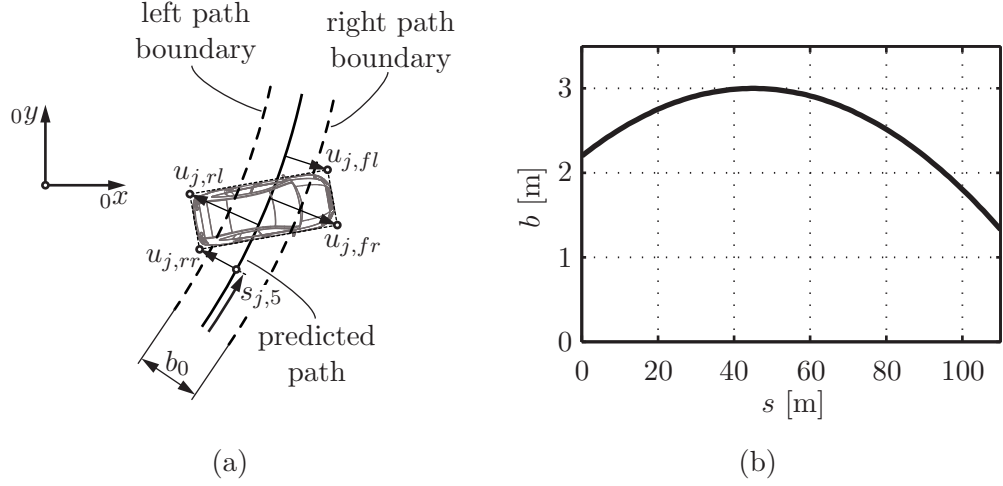
Figure 5.6.: (a) Special case of eq. (5.39) and (b) non-constant path width b as function of s, as described in eq. (5.41)

5.3.2. Priority Algorithm

The *Priority Algorithm* is another possible way to select the OTF. As described in eq. (5.37), every object is represented as a list of four points. In the special case where eq. (5.39) is fulfilled, a fifth point is added to the list, as described in eq. (5.40). Each of these points has a corresponding priority P, which is calculated using the equation

$$P\left(s,u\right) = \left(b_1\,s^2 + b_2\,s + b_3\right)\mathrm{e}^{-c(s)\,u^n}, \tag{5.43}$$

where the coefficients b_1 to b_3 and $c\left(s\right)$ are determined using the boundary conditions

$$\begin{aligned} P\left(0,0\right) &= P_0, \\ P\left(L,0\right) &= P_L, \\ \left.\frac{\partial P}{\partial s}\right|_{\substack{s=0\\u=0}} &= 0 \text{ and} \\ P\left(s,\pm\frac{b\left(s\right)}{2}\right) &= P_b. \end{aligned} \tag{5.44}$$

This results in a polynomial of second order in the longitudinal direction s of the natural coordinate system. In the lateral direction u, the function is described by a *Gaussian Bell Curve* if the parameter $n = 2$. If n is increased (e. g. $n = 4, 6, \cdots$), the shape of the function becomes increasingly rectangular. The parameter $c\left(s\right)$ is a function of the longitudinal coordinate, if the path width is a function of s. If the path width is set to a constant value of b_0, then c is constant for all s. Figure 5.7 shows $P\left(s,u\right)$ of eq. (5.43) for the two cases $n = 2$ and $n = 8$. For the path width, the function and parameters given in chapter 5.3.1.2 are used.
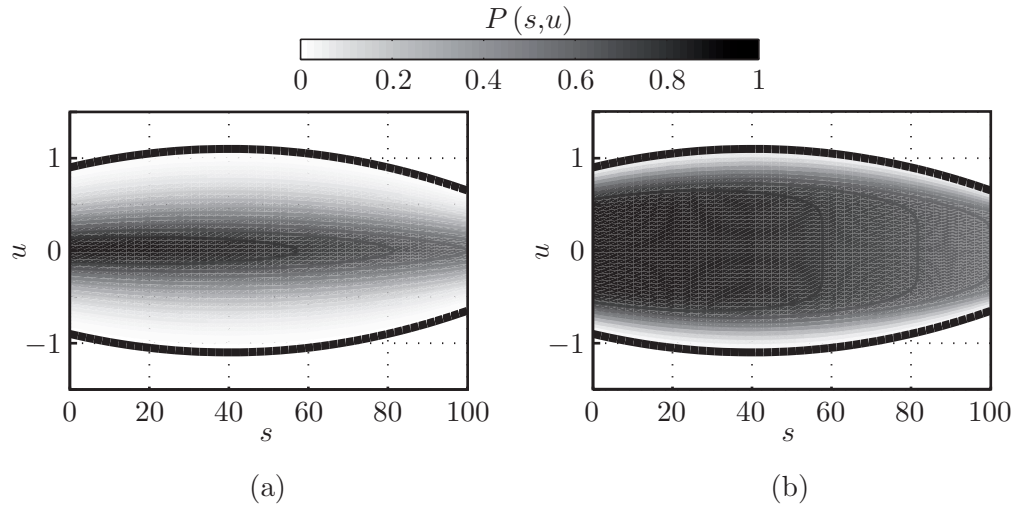
Figure 5.7.: Priority $P(s, u)$ of eq. (5.43) for parameters $P_0 = 1$, $P_L = 0.7$ and $P_b = 0.01$ for the two cases (a) $n = 2$ and (b) $n = 8$

5.3.3. Comparison of Object Selection Algorithms

Figure 5.8 shows an example with two objects and the lane markings for a curved two-lane road. Here, the ego vehicle is following object 1, both of which are in the left lane overtaking object 2, which is travelling in the right lane at a lower speed than those of the ego and object 1. The grey marked area depicts the predicted path. If the *in-lane algorithm* of chapter 5.3.1.1 is used, object 2 will be selected as the OTF because is has a smaller s-coordinate than object 1, $s_{2,fl} < s_{1,rr}$. However, when using the *priority algorithm* described in 5.3.1.2, object 1 will be selected because $P(s_{1,rr}, u_{1,rr}) < P(s_{2,fl}, u_{2,fl})$. The situation in fig. 5.8 shows the significant advantage of the priority algorithm. When overtaking wide vehicles (e. g. commercial vehicles), the OTF of the in-lane algorithm jumps to the vehicle in the neighbouring lane, which in most situations is the wrong decision. This is the result of the error in the path prediction. If the error is almost zero, both algorithms would select object 1, which is the right decision. However, the predicted path would rarely be identical with the real driven path in the future. Therefore, the use of additional information will help to increase the quality of the object selection algorithms.

If n in eq. (5.43) is set to very high values, the priority algorithm results in the selection of the nearest object in the predicted path, as described in chapter 5.3.1. This is because the shape of the priority function in the lateral u-direction degenerates to a rectangular function, where all points at the same s coordinate have the same priority P. For further investigations in this work, the priority algorithm with $n = 2$ is used.
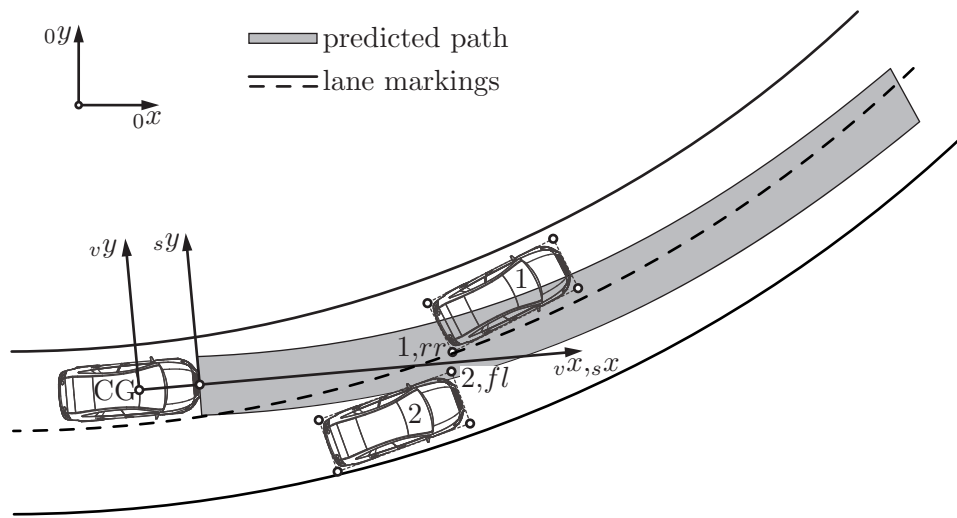
Figure 5.8.: Situation with two objects

6

Upper Level Controller Parameter Identification

6.1. Non-Linear Time Gap Controller

The investigated *Adaptive Cruise Control* (ACC) controller is based on the *Continuous Time Gap* (CTG) controller of eq. (2.28). For comfort reasons, small errors in the position or velocity of eq. (2.23) and eq. (2.24) should lead to small desired accelerations a_{des}. This may lead to problems when a platoon of vehicles, each equipped with the same CTG controller, is travelling at steady state and the first vehicle decelerates. Figure 6.1 illustrates this situation for the vehicles with the number 1 and $i - 1$ to $i + 1$.

According to [LP99], the vehicle motion of the $i - 1$-th and and i-th vehicle are described by

$$\tau_{long} \dddot{x}_{i-1} + \ddot{x}_{i-1} = P_3 \left[\dot{r}_{i-1} + P_4 \left(r_{i-1} - s_0 - v_{i-1} \, \tau_{set} \right) \right] \text{ and} \tag{6.1}$$

$$\tau_{long} \dddot{x}_i + \ddot{x}_i = P_3 \left[\dot{r}_i + P_4 \left(r_i - s_0 - v_i \, \tau_{set} \right) \right], \tag{6.2}$$

using the vehicle model of eq. (2.25) and the general CTG controller of eq. (2.28) reading

$$a_{des} = P_3 \left(e_{\dot{r}} + P_4 \, e_r \right). \tag{6.3}$$

The inter-vehicle distance and velocity are defined by $r_i = x_{i-1} - l_{veh,i-1} - x_i$ and its
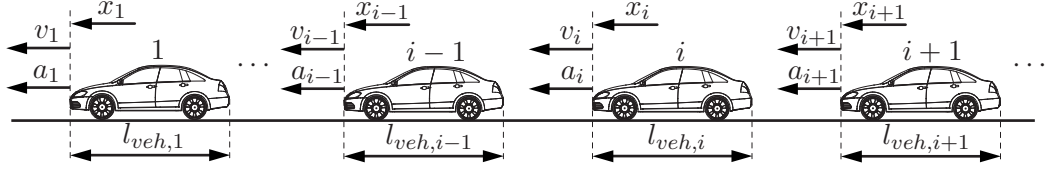
Figure 6.1.: Platoon of vehicles

time-derivative. The difference between eq. (6.1) and eq. (6.2) reads

$$
\tau_{long} \underbrace{(\dddot{x}_{i-1} - \dddot{x}_i)}_{\dddot{r}_i} + \underbrace{(\ddot{x}_{i-1} - \ddot{x}_i)}_{\ddot{r}_i} =
$$
$$
P_3 \Big[(\dot{r}_{i-1} - \dot{r}_i) + P_4 \big[\underbrace{(v_i - v_{i-1})}_{-\dot{r}_i} \tau_{set} + r_{i-1} - r_i \big] \Big]. \tag{6.4}
$$

If all the initial conditions of r_i and its derivatives are set to zero, the transfer function for the complex variable $s \in \mathbb{C}$ reads

$$
\frac{R_i(s)}{R_{i-1}(s)} = \frac{s\, P_3 + P_3\, P_4}{s^3\, \tau_{long} + s^2 + s\, (P_3 + P_3\, P_4\, \tau_{set}) + P_3\, P_4}, \tag{6.5}
$$

where the Laplace transform of the inter-vehicle distance $\mathcal{L}\{r_i(t)\} = R(s)$ is used. According to [WDS09], [LP99], [dWB99] and [Raj06], the platoon is string stable if

$$
\left| \frac{R_i(j\omega)}{R_{i-1}(j\omega)} \right| \leq 1,\ \forall\ \omega. \tag{6.6}
$$

In other words, the spacing errors should decrease moving back in the platoon, meaning $e_{i-1} \geq e_i$,[dWB99]. This leads to the two constraints for choosing P_3 and P_4 reading

$$
P_3 + P_3\, P_4\, \tau_{set} \leq \frac{1}{2\, \tau_{long}} \quad \text{and} \quad P_3\, P_4\, \tau_{set}^2 + 2\, P_3\, \tau_{set} \geq 2 \text{ or} \tag{6.7}
$$

$$
P_3 + P_3\, P_4\, \tau_{set} > \frac{1}{2\, \tau_{long}} \quad \text{and} \quad \left(P_3 - \frac{1}{2\, \tau_{long}} \right)^2 < \left(\frac{\tau_{set}}{\tau_{long}} - 2 \right) P_3\, P_4. \tag{6.8}
$$

Simulations were carried out in which the parameters were set to $\tau_{set} = 1.5\,$s and $\tau_{long} = 0.5\,$s. In this case, the leading vehicle has an input for a desired acceleration of $a_{des} = -2\,$m/s^2 during the time $t = 1$ to $4\,$s. With an initial vehicle speed of $30\,$m/s the manoeuvre ends at a vehicle speed of about $24\,$m/s. Most often, these manoeuvres are carried out to adjust the vehicle speed to a certain speed limit. Thus, it is a very slight deceleration. Figure 6.2(a) shows the output of a simulation with the parameters $P_4 = \frac{1}{\tau_{set}}$ and $P_3 = 2.5$. These parameters satisfy the condition of eq. (6.7), and the simulations show that the platoon of vehicles is stable. In [WDS09], Winner proposed

using $P_3 = 0.25$ and $P_4 = 0.2$ for small errors to create a comfort-oriented system. However, these parameters cannot satisfy either eq. (6.7) or eq. (6.8), and therefore this set of parameters is not string stable. This could be proven by the simulations of fig. 6.2(b). The applied disturbance of vehicle 1 results in very high accelerations of the proceeding vehicles. At vehicle 18, the inter-vehicle distance $_s r$ reaches nearly zero, meaning a very dangerous situation occurs between vehicle 17 and 18. At vehicle 19, the inter-vehicle distance reaches zero, meaning vehicle 19 crashes into 18. This situation shows why a non-string-stable ACC controller is dangerous.

To handle this trade-off between comfort and safety, the control law of eq. (6.3) is extended with another term. The resulting control law for the upper level controller reads

$$a_{des} = P_1 \sinh\left[P_2 \left(e_{\dot{r}} + P_4 \, e_r\right)\right] + P_3 \left(e_{\dot{r}} + P_4 \, e_r\right), \qquad (6.9)$$

which is used for the further investigations in this work. To meet the string stability and comfort requirements, the controller should output very small desired accelerations at small errors and high accelerations at high errors. These requirements lead to the extension with the trigonometric function. Winner et al. used a similar approach in [WDS09]. Figure 6.3 shows the comparison between the segmented controller of Winner et al. and the control law described in eq. (6.9). For both functions, the argument $e_{syn} = e_{\dot{r}} + P_4 \, e_r$ was used.

6.2. ACC Controller Parameter Identification

To identify the parameter of the ACC controller, the scenarios have to be extracted from the measurements described in chapter 4. Therefore, the condition is defined that the index of the *Object to Follow* (OTF) should not change for a minimum time of ten seconds. Additionally, the probability of existance (see chapter 4 for a description of the quantity) of the selected object must satisfy the condition $p_{ex} \geq 99\,\%$. This leads to a list of 505 scenarios with a minimum length of $T_{min} = 10\,\mathrm{s}$, a maximum length of $T_{max} = 253.5\,\mathrm{s}$, a mean length of $\bar{T} = 45.4\,\mathrm{s}$, and a standard deviation of $\sigma_T = 39.53\,\mathrm{s}$. Figure 6.4 shows the steps of the parameter identification. The selected scenarios are divided into two main groups. The first group is the *standstill situation*, when the ego velocity and the velocity of the OTF equal zero, $_v v_x = 0$, and $_s v_{OTF} = 0$, see chapter 6.2.1. The output of these manoeuvres is the inter-vehicle standstill distance s_0. The second group of scenarios are the driving manoeuvres when $_v v_x \geq 1.5\,\mathrm{m/s}$. If the condition $\frac{1}{TTC_{OTF}} \leq 0.05\,\mathrm{s}^{-1}$ is also satisfied, it is called a *constant following manoeuvre*, see also chapter 6.2.2. The output of these scenarios is the selected time gap τ_{set}. With the rest of the scenarios, the so-called *dynamic following manoeuvres*, the controller parameters P_1 to P_4 of the ACC controller of eq. (6.9) are identified. The following chapters describe the steps of the identification in detail.
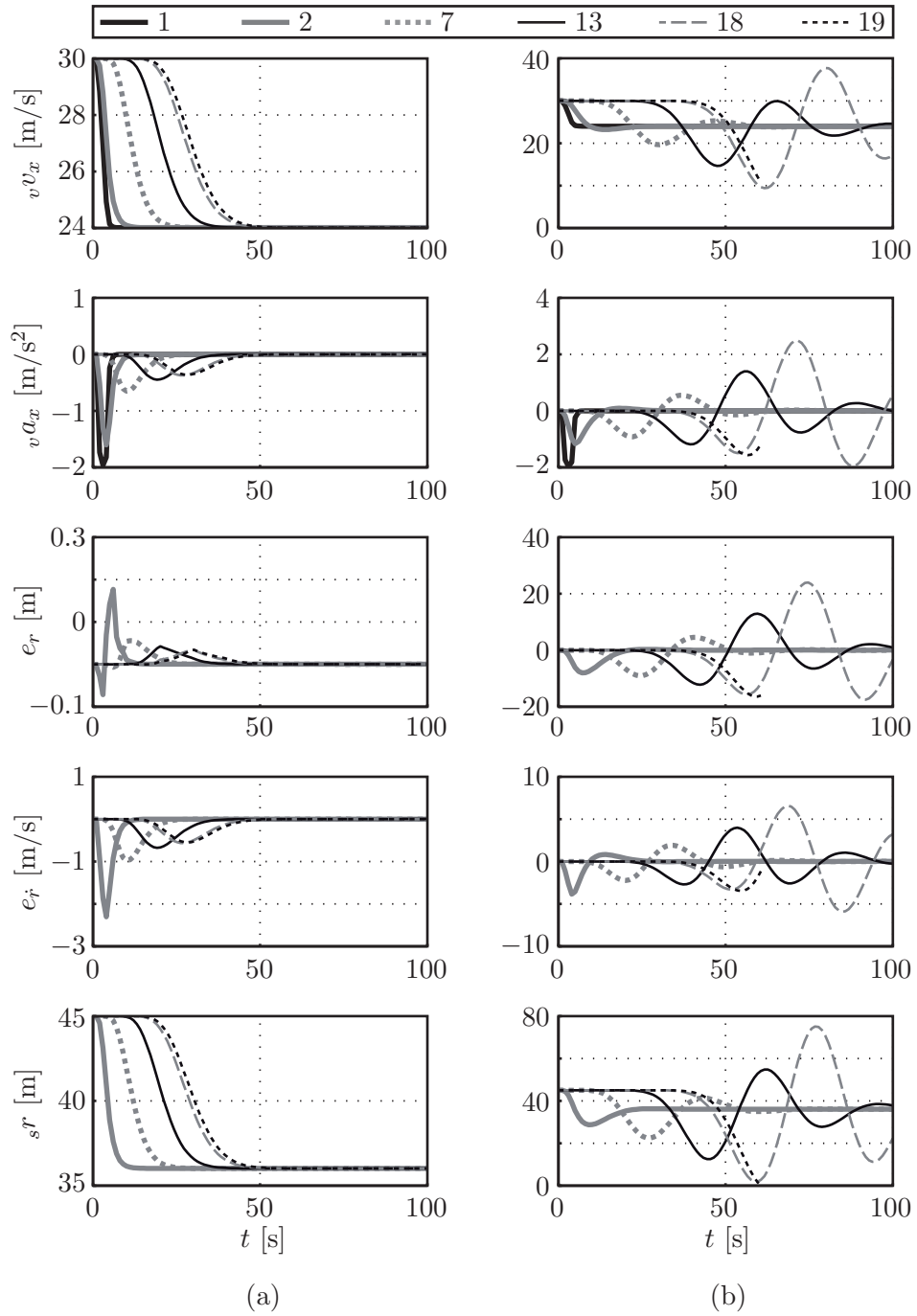
Figure 6.2.: Simulations for a platoon of 24 vehicles with the parameters (a) $P_4 = \frac{1}{1.5}$ and $P_3 = 2.5$ and (b) $P_3 = 0.25$ and $P_4 = 0.2$
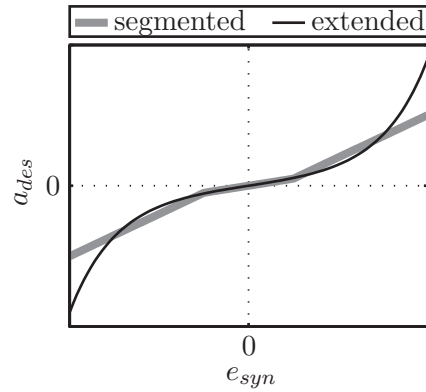
Figure 6.3.: Comparison of the segmented controllers proposed in [WDS09] and eq. (6.9)
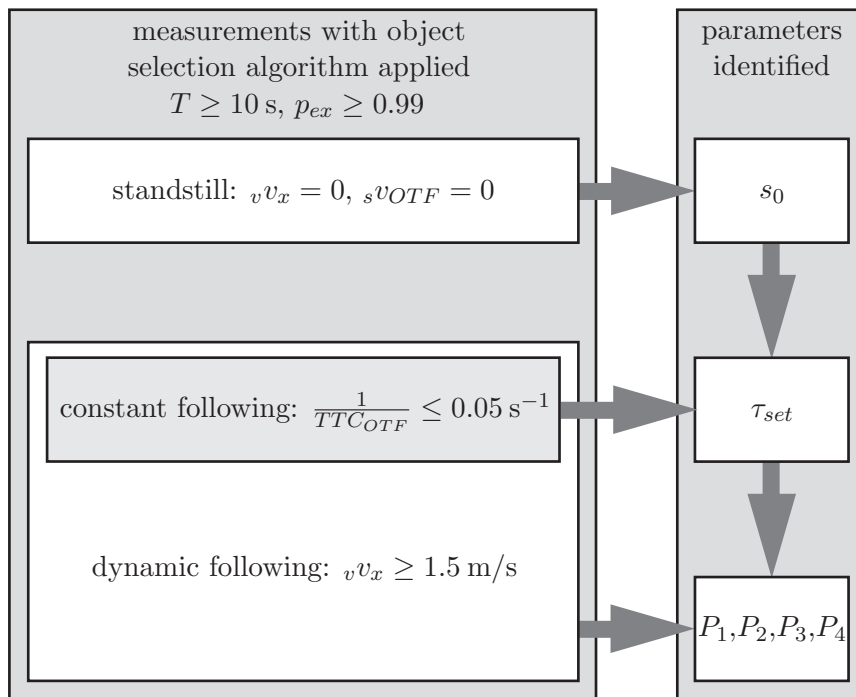

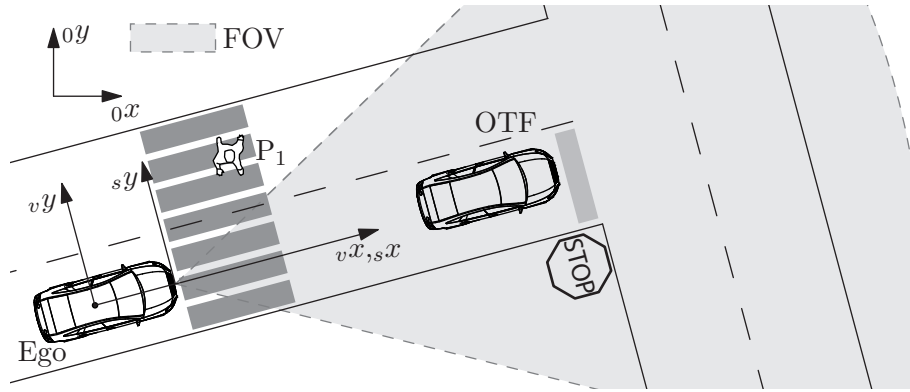Figure 6.4.: Steps in parameter identification

Figure 6.5.: Example of an incorrectly identified standstill situation

6.2.1. Standstill Situation

As already mentioned, the conditions for the standstill situation are that the ego vehicle and the OTF velocities equal zero, $_v v_x = 0$, and $_s v_{OTF} = 0$. There may be situations when all these conditions are satisfied, but the ego vehicle is not actually following the OTF. Figure 6.5 shows such an example. Here, the ego vehicle is following the OTF. The ego vehicle stops at a cross-walk because a pedestrian P1 crosses the road, and the OTF stops at a stop sign at a bigger inter-vehicle distance. With the conditions mentioned above, this situation is defined as a standstill situation, which is not true. Therefore, another condition has to be introduced, which is described by Kreyszig in [Kre99]. He defined that the sample x is an outlier if one of the conditions

$$x < IQR - 1.5\, q_l \qquad\qquad \text{or} \qquad\qquad x > IQR + 1.5\, q_u \qquad (6.10)$$

is satisfied, whereby q_l is the lower quartile, q_u is the upper quartile, and IQR is the interquartile range reading $IQR = q_u - q_l$ for the data set of x. Figure 6.6 shows the histogram for the unfiltered s_0 and the filtered s_0 according to eq. (6.10). There, it can be seen that inter-vehicle distances up to 35 m may occur. Situations with such large distances are similar to fig. 6.5. The filtering reduces the number of standstill situations from 533 to 441. For further investigations, the filtered data set for s_0 is used with its mean value of $\bar{s}_0 = 1.978$ m, which correlates very well with the values mentioned in literature. In [MY08], Moon et al. identified a clearance at zero speed of 1.98 m. Both values nearly meet the requirements out of standard [Tec09], which stipulates that the inter-vehicle distance should not fall below 2 m.

6.2.2. Constant Following Scenario

For the constant following scenario, the ego vehicle velocity must fulfil $_v v_x \geq 1.5$ m/s, and the inverse of the *Time to Collision* (TTC) must be less than a certain limit of
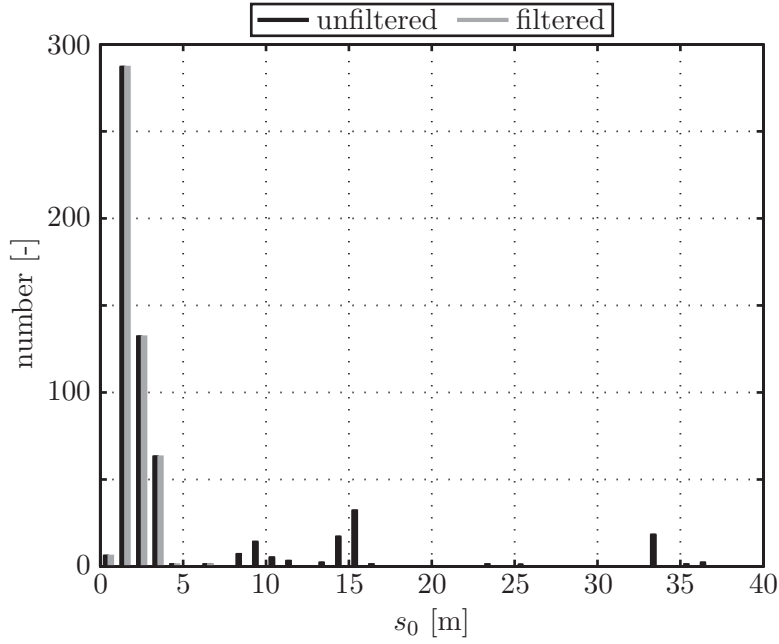
Figure 6.6.: Histogram for filtered and unfiltered s_0

$TTC_{OTF}^{-1} \leq 0.05\,\mathrm{s}^{-1}$. This limit was set according to Moon et al., [MY08]. The TTC is defined by the equation

$$TTC_i = -\frac{{}_s r_i}{{}_s \dot{r}_i}. \tag{6.11}$$

This describes the time it will take until the i-th object will collide with the ego vehicle, if neither vehicle accelerates or decelerates. According to Fancher et al., the TTC is a good measure for human-like range-rate estimation because humans approximate the relative velocity of any object at big distances by the so-called looming effect, [FBE01]. The looming effect is the change of the size of the projected picture of the object onto the retina of the human eye, see fig. 6.7. The relation $h = r\,\alpha$ is given for $\alpha \ll 1$, which is true for $r \gg h$. The derivative with respect to time reads $0 = \dot{r}\,\alpha + r\,\dot{\alpha}$. The definition of TTC in eq. (6.12) could be found by rearranging this equation to

$$\frac{\alpha}{\dot{\alpha}} = \underbrace{-\frac{r}{\dot{r}}}_{TTC}. \tag{6.12}$$

This relations shows why the TTC is a good measure for evaluating the relative velocity as humans would.

During constant following, the distance to the OTF should be described by eq. (2.22). To find the missing parameter τ_{set}, a least square problem is defined, where the squared error between the measured distance to the object ${}_s r_{OTF}$ and eq. (2.22) is minimized.
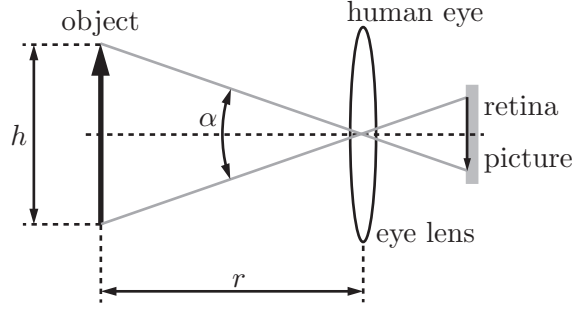
Figure 6.7.: Projection of an object onto the human retina, adapted from [FBE01]

The cost function is defined by

$$J_{CF} = \sum_{i=1}^{n_{CF}} \left({}_s r_{OTF,i} - s_0 - {}_v v_{x,i}\, \tau_{set}\right)^2 , \qquad (6.13)$$

where the n_{CF} is the number of available measured data sets fulfilling the required conditions for constant following. The necessary and sufficient conditions for finding the minimum read

$$\frac{\partial J_{CF}}{\partial \tau_{set}} = 0 \qquad \text{and} \qquad \frac{\partial^2 J_{CF}}{\partial \tau_{set}^2} > 0. \qquad (6.14)$$

These conditions lead to the very compact equation

$$\tau_{set} = \frac{{}_v\mathbf{v}_x^{\mathrm{T}} \left({}_s\mathbf{r}_{OTF} - s_0\, \mathbf{I}_{n_{CF}\times 1}\right)}{{}_v\mathbf{v}_x^{\mathrm{T}}\, {}_v\mathbf{v}_x}, \qquad (6.15)$$

where the vectors ${}_v\mathbf{v}_x$ and ${}_s\mathbf{r}_{OTF}$ contain all the measurements fulfilling the required conditions for constant following. Both vectors have a length of n_{CF}. The vector $\mathbf{I}_{n_{CF}\times 1}$ consists of ones at n_{CF} rows. For the given measurements, the number of data sets equals $n_{CF} = 138\,878$. Figure 6.8 shows the fitted straight according to eq. (2.22), with the parameter $s_0 = 1.978\,\mathrm{m}$ and the identified time gap $\tau_{set} = 1.174\,\mathrm{s}$. Moon et al. identified in [MY08] a time gap of $1.36\,\mathrm{s}$. Fancher et al. defined in [FBE01] that the selectable time gap should be in the range of 1 to $2\,\mathrm{s}$. In standard [Tec09], the minimum selectable time gap is set to $1\,\mathrm{s}$, while in standard [Tec10] it is limited by $0.8\,\mathrm{s}$. The identified time gap shows that the mean driver selects a time gap near the minimum regarding a safe vehicle following time of $1\,\mathrm{s}$. This suggests that there are many people who select time gaps below this limit. This could be proven by the fact that in the year 2007, $11.7\,\%$ of the accidents documented by the police in Germany were related to too close distances to other road users, including insufficient following distances, [Sta08]. Figure 6.8 also demonstrates that there is a wide variation in human driving behaviour.
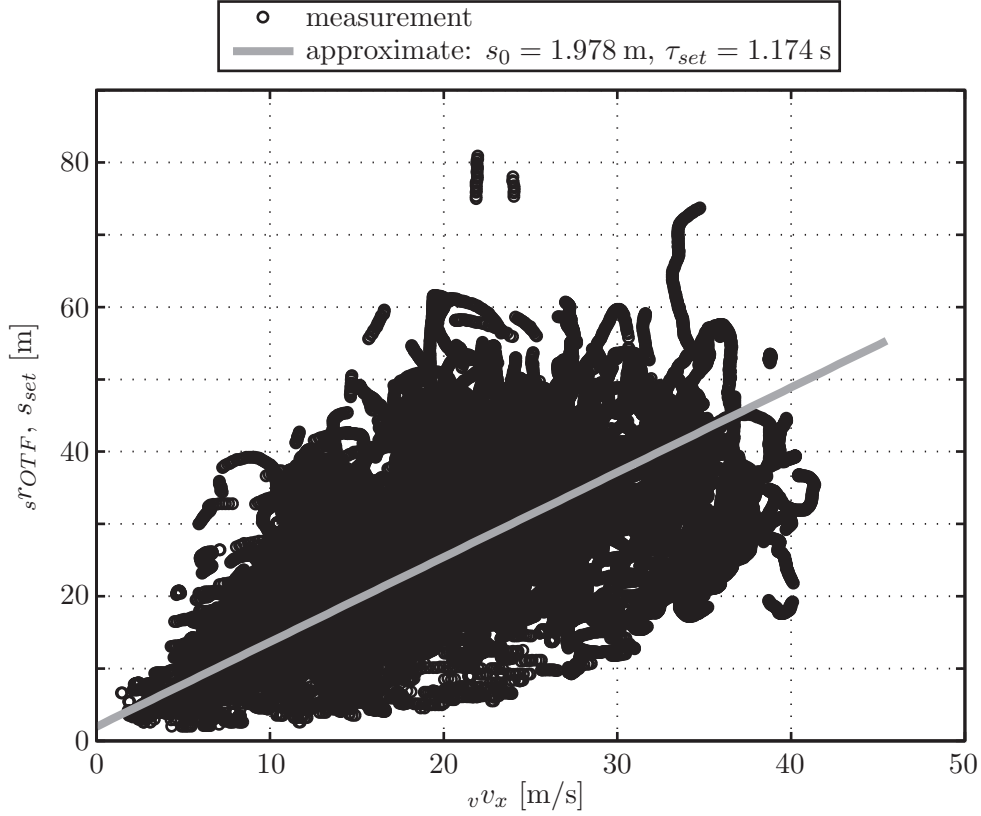
Figure 6.8.: Measured distances $_sr_{OTF}$ over vehicle velocity $_vv_x$ for the constant following scenario and identified distance law s_{set} according to eq. (2.22)

6.2.3. Dynamic Following Scenario

The rest of the scenarios are selected to identify the ACC controller parameters P_1 to P_4. To this end, an optimization problem is formulated using the simplified longitudinal vehicle model of eq. (2.26). The longitudinal motion of the OTF in the global coordinate system at time step t_k is determined from the measurements reading

$$\underbrace{\begin{bmatrix} _0s_{OTF,k} \\ _0v_{OTF,k} \end{bmatrix}}_{_0\mathbf{x}_{OTF,k}} = \begin{bmatrix} _vs_{x,k} \\ _vv_{x,k} \end{bmatrix} + \begin{bmatrix} _sr_{OTF,k} \\ _s\dot{r}_{OTF,k} \end{bmatrix}, \tag{6.16}$$

where the longitudinal position of the ego vehicle is calculated using the measured speed signal, $_vs_{x,k} = \int_0^{t_k} {_vv_x}\, dt$. The initial condition of the vehicle model of eq. (2.26) is generated out of the measurements reading

$$\tilde{\mathbf{x}}_0 = \begin{bmatrix} 0 \\ _vv_{x,0} \\ _va_{x,0} \end{bmatrix}. \tag{6.17}$$

The input for the ACC controller is calculated using eqs. (2.22) to (2.24). The parameters of eq. (2.22) are found in chapters 6.2.1 and 6.2.2. The inter-vehicle distance used at zero speed is set to $s_0 = 1.978\,\text{m}$ for all simulated manoeuvres. The parameter τ_{set} has to be determined for each manoeuvre, using the method described in chapter 6.2.2. This is necessary due to the significant variation of the following behaviour of different drivers.

The output of the simulations is the state vector at simulation time t_k reading

$$\tilde{\mathbf{x}}_k = \begin{bmatrix} v\tilde{s}_{x,k} \\ v\tilde{v}_{x,k} \\ v\tilde{a}_{x,k} \end{bmatrix}, \tag{6.18}$$

where the longitudinal position during the simulation is calculated using $v\tilde{s}_{x,k} = \int_0^{t_k} v\tilde{v}_x \, dt$. At time t_k, the error between measurement and simulation is defined by

$$\tilde{\mathbf{e}}_k = \begin{bmatrix} vs_{x,k} \\ vv_{x,k} \\ va_{x,k} \end{bmatrix} - \tilde{\mathbf{x}}_k. \tag{6.19}$$

The goal during the identification process is to minimize the cost function reading

$$J_{DF} = \sum_k \tilde{\mathbf{e}}_k^{\mathrm{T}} \, \tilde{\mathbf{e}}_k, \tag{6.20}$$

which is the sum of the squared errors over all time steps t_k between measurements and simulation. To perform the optimization, the *Nelder-Mead-Method* is used, which has the advantage that gradients of the cost function with respect to the searched parameters are not needed, [Obe12]. A detailed description of the algorithm used is given in appendix E. The output of this method is sensitive to the initial parameters $P_{1,0}$ to $P_{4,0}$.

In general, the Nelder-Mead-Algorithm performs an optimization with the output $P_i \in \Re$. For the special case that P_i has either an upper or a lower bound or both, a parameter transformation has to be performed to include this limitation in the optimization process. The transformation rules read

$$P_i = P_{i,min} + \frac{P_{i,max} - P_{i,min}}{1 + \mathrm{e}^{-P_i'}} \qquad \text{for} \qquad P_{i,min} < P_i < P_{i,max}, \tag{6.21}$$

$$P_i = P_{i,max} - \mathrm{e}^{-P_i'} \qquad \text{for} \qquad P_i < P_{i,max} \text{ and} \tag{6.22}$$

$$P_i = P_{i,min} + \mathrm{e}^{P_i'} \qquad \text{for} \qquad P_{i,min} < P_i. \tag{6.23}$$

Figure 6.9 illustrates the functions eqs. (6.21) to (6.23), where eq. (6.21) is a sigmoid function. The minimization can be solved by plugging eqs. (6.21) to (6.23) in the optimization problem and varying P_i' instead of P_i. At the end of the process, the back transformation has to be done with the help of eqs. (6.21) to (6.23). One important advantage of this transformation is that a certain step width at P_i' leads to small steps near the limits of $P_{i,max}$ or $P_{i,min}$.
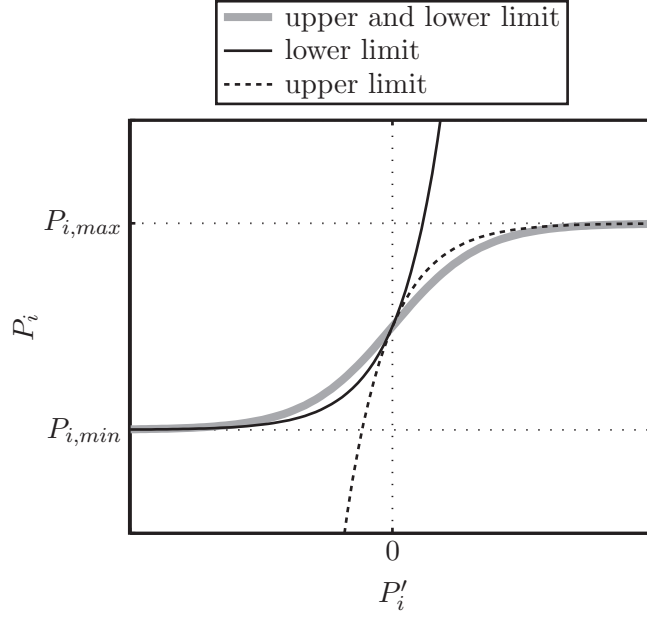
Figure 6.9.: Transformation rule for either upper or lower bounds or both upper and lower bounds of P_i

For further considerations, the term used in the trigonometric and the linear part of eq. (6.9) was replaced by a new variable defined as

$$e_{syn} = (e_{\dot{r}} + P_4\, e_r).$$ (6.24)

As mentioned above, the desired acceleration of the ACC controller should increase with an increasing error. This could be described by

$$\frac{\partial a_{des}}{\partial e_{syn}} = P_1\, P_2 \underbrace{\cosh\left(P_2\, e_{syn}\right)}_{\geq 1,\ \forall\, e_{syn}} + P_3 > 0.$$ (6.25)

The trigonometric function in eq. (6.25) is always equal to or larger than one for all $P_2\, e_{syn}$. Therefore, the conditions for the parameters P_1 to P_3 can be found reading

$$P_1\, P_2 > 0 \qquad \text{and} \qquad P_3 > 0 \text{ or}$$ (6.26)
$$P_1\, P_2 < 0 \qquad \text{and} \qquad P_3 = \lim_{x \to \infty} x.$$ (6.27)

Due to the fact that eq. (6.27) is impossible in reality, only the conditions of eq. (6.26) are used. The first condition $P_1\, P_2 > 0$ leads to $(P_1 > 0 \cap P_2 > 0) \cup (P_1 < 0 \cap P_2 < 0)$. These two parameters do not influence any part of the optimization other than the ACC controller. Therefore, it does not matter which of the two cases is used.

A negative inter-vehicle error $e_r < 0$ and no relative velocity error $e_{\dot{r}} = 0$ means that the ego vehicle is too close to the OTF. Therefore, the controller should output a negative

acceleration $a_{des} < 0$. This is guaranteed by eq. (6.26). If the inter-vehicle distance equals zero $e_r = 0$ and the relative velocity error is negative, $e_{\dot{r}} < 0$, meaning the vehicle is approachingg the OTF, the output should be a negative desired acceleration, $a_{des} < 0$. This can only be guaranteed if the conditions of eq. (6.26) and the parameter $P_4 > 0$ are satisfied.

To sum up, the boundary conditions and the initial conditions were set to

$$0 < P_1 < 0.5, \qquad 0 < P_2, \qquad 0 < P_3 < 0.5, \qquad 0 < P_4 \text{ and} \qquad (6.28)$$

$$P_{1,0} = 0.3, \qquad P_{2,0} = 0.5, \qquad P_{3,0} = 0.1, \qquad P_{4,0} = 0.1. \qquad (6.29)$$

The upper boundaries of P_1 and P_3 were set for comfort reasons. These limits should lead to small values for P_1 and P_3 in order to have small accelerations for small synthetic errors e_{syn}, defined in eq. (6.24). The parameter P_2 affects the desired acceleration for small errors as well, but it is not limited to an upper boundary to ensure string stability. These boundaries led to the results

$$P_1' = 0.9685, \qquad P_2' = -0.0983, \qquad P_3' = 0.3850 \text{ and} \qquad P_4' = -1.5967 \qquad (6.30)$$

after 205 iterations, which could be transformed back to

$$P_1 = 0.3624, \qquad P_2 = 0.9063, \qquad P_3 = 0.2975 \text{ and} \qquad P_4 = 0.2026 \qquad (6.31)$$

with the resulting cost function of $J_{DF} = 3\,769\,829$. Figure 6.10 shows the parameter histories for P_1 to P_4 and P_1' to P_4' with the corresponding cost function J_{DF}.

6.3. Validation of the Identified Parameters

The validation of the identified parameters is carried out in three steps. First, the string stability is checked. Next, simulations with the simplified longitudinal vehicle model are performed, and the output is compared with the measured data. For the third step, the performance of the controller is compared to measurements obtained with a production vehicle equipped with an ACC system. Chapters 6.3.1 to 6.3.3 provide a detailed description of the three steps.

6.3.1. String Stability

Figure 6.11 shows the time histories for a platoon of 100 vehicles, each equipped with the ACC controller of eq. (6.9) using the parameters of eq. (6.31). The first vehicle copies the movement of the leading vehicle in fig. 6.2, with a desired acceleration of $-2\,\text{m/s}^2$ in the timespan between 1 to 4 s. Figure 6.11 illustrates that the platoon is string stable due to the decreasing inter-vehicle error e_r going backwards in the platoon. String stability cannot be proven analytically because the Laplace-Transform of the control law of eq. (6.9) cannot be rearranged in the form of eq. (6.6), due to the trigonometric function in the control algorithm.
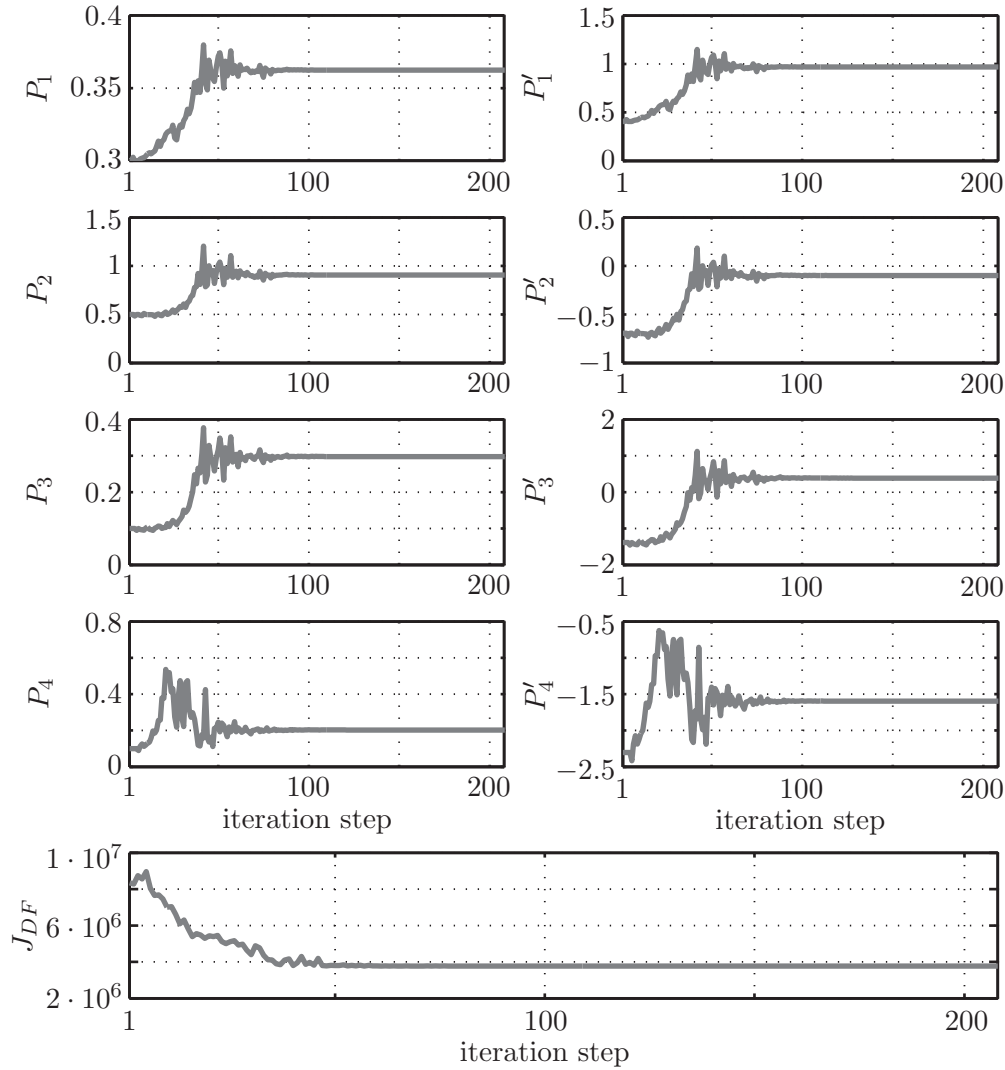
Figure 6.10.: Parameter histories for the executed iteration steps

6.3.2. Simplified Model

The parameter identification was performed with 456 manoeuvres with a minimum length of 10 s and an overall length of 20 679.6 s. For the validation, simulations with the simplified longitudinal vehicle model of eq. (2.26) and the parameters identified for the ACC controller of eq. (6.9) were carried out. Figure 6.12 compares measurement and simulation results of the longitudinal vehicle speed $_vv_x$, the acceleration $_va_x$, the range $_sr_{OTF}$, the range rate $_s\dot{r}_{OTF}$ and the inverse of the Time to Collision to the object to follow TTC_{OTF}^{-1} for a manoeuvre. The simulated vehicle speed and acceleration match the recorded data very well. It is remarkable that the peak accelerations in the simulation
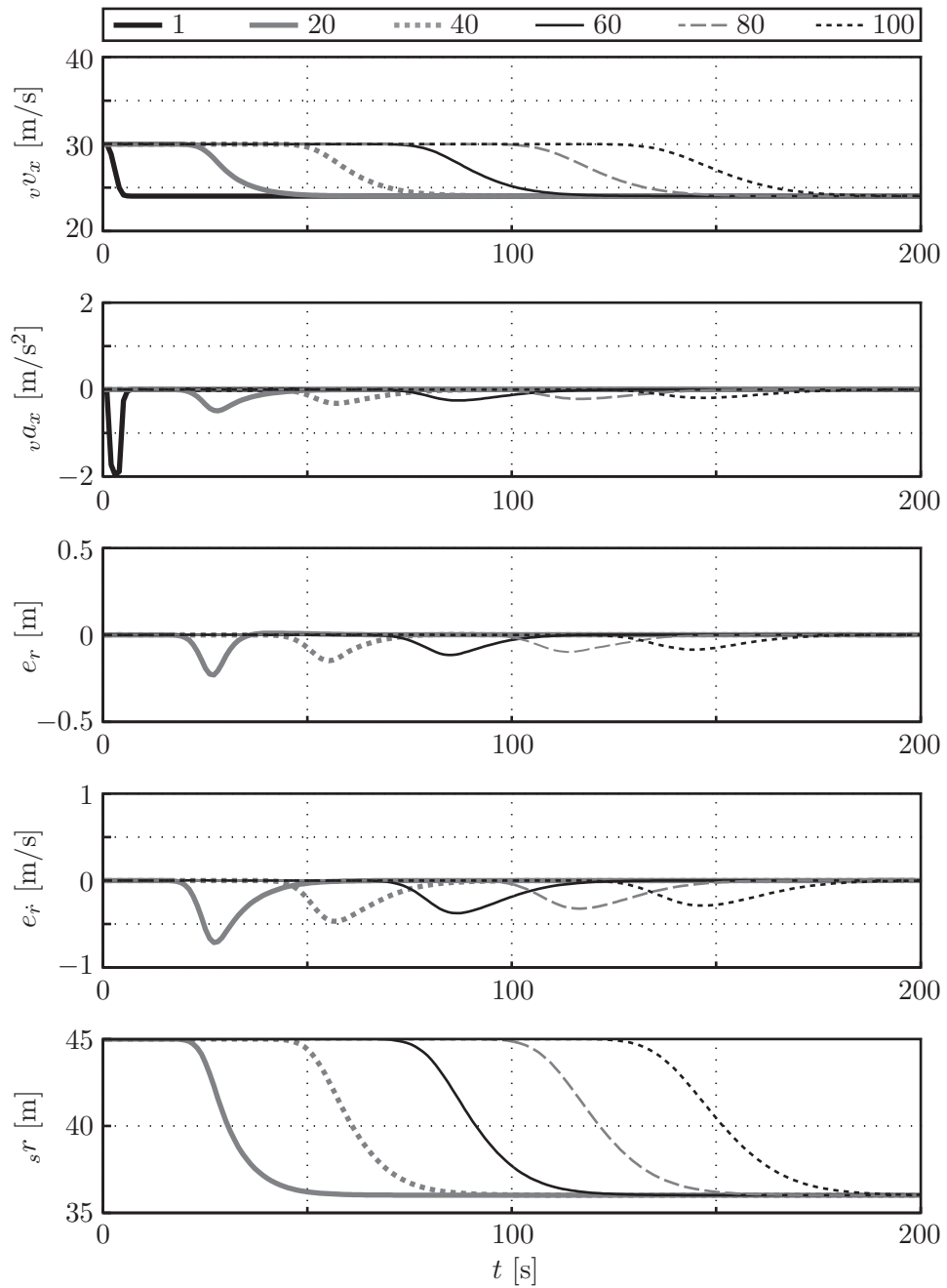
Figure 6.11.: Simulations for a platoon of 100 vehicles with the parameters listed in eq. (6.31)

are smaller than those in the measurements. This indicates that the vehicle movement will be more comfortable than the human driving in the measurement. The difference between measured and simulation is greater in the inter-vehicle distance $_sr_{OTF}$ than in the inter-vehicle range rate $_s\dot{r}_{OTF}$. This is due to the fact that the desired relative speed $_s\dot{r}_{OTF}$ should be controlled to zero. The desired inter-vehicle distance depends on the selected time gap τ_{set}, see eqs. (2.22) and (2.23), which could be chosen unbounded by the driver. An error in τ_{set} will lead directly to an error between measurements and simulation for the inter-vehicle distance. Since the identified parameter P_4 shows the weight of e_r to $e_{\dot{r}}$, it has the unit s^{-1}. This means that an error of $e_{\dot{r}} = 1\,\text{m/s}$ results in the same desired acceleration as $e_r \approx 5\,\text{m}$. This value correlates very well with the values mentioned in the literature. In [WDS09], Winner er al. shows that a weight of $P_4 = 0.2\,\text{s}^{-1}$ will lead to good results. Gächter determined that a good weight is in the range of $0.2\,\text{s}^{-1} < P_4 < 0.25\,\text{s}^{-1}$, where increasing the weight leads to a more sporty behaviour of the vehicle, [Gäc12]. Thus, small weights make the ACC-equipped vehicle decelerate earlier and have less undershoot in the inter-vehicle distance when approaching a slower OTF, compared to large values for P_4.

6.3.3. Full-Vehicle Model with ACC Measurements

In this chapter, the performance of the identified parameters is compared with measurements with a real ACC-equipped vehicle. The target of this comparison is not to achieve the identical system behaviours but rather for the recorded and simulated data to have similar shapes, especially for the longitudinal acceleration $_va_x$.

The ego vehicle travels behind the OTF at a set time gap of $\tau_{set} = 1.2\,\text{s}$. Both the ego vehicle and the OTF drive at $_vv_x \approx {_v}v_{OTF,x} \approx 58\,\text{km/h}$. At time $t = 47\,\text{s}$, the OTF begins to accelerate until it reaches the speed $_vv_{OTF,x} = 77\,\text{km/h}$, with a maximum longitudinal acceleration of $_va_{OTF,x,max} = 1.3\,\text{m/s}^2$. It starts to decelerate at time $t = 70\,\text{s}$ with a maximum deceleration $_va_{OTF,x,min} = -1.1\,\text{m/s}^2$ until it reaches the final speed of the OTF, $_vv_{OTF,x} = 58\,\text{km/h}$. The longitudinal speed $_vv_x$ and acceleration $_va_x$ of the ego vehicle and the inter-vehicle distance and range rate $_sr_{OTF}$ and $_s\dot{r}_{OTF}$ are recorded. Figure 6.13 shows the measured time histories for both the ego vehicle and the OTF.

The simulation is carried out using a commercially available software package called *CarMaker*, which is a product of *IPG Automotive GmbH*. It provides an interface in which custom controllers can be implemented. In addition, optimal environmental-recognition sensors and traffic objects are already available. For the simulation, the ACC controller of eq. (6.9) with the parameters of eq. (6.31) was implemented in the simulation. As an environmental-recognition sensor, the provided optimal *Radio Detection and Ranging* (RADAR) sensor was used with a *Field of View* (FOV) described by the maximum detection range $r_{FOV} = 200\,\text{m}$ and an aperture angle $\varphi_{FOV} = \pm 8°$. The whole simulation was done on a straight road.

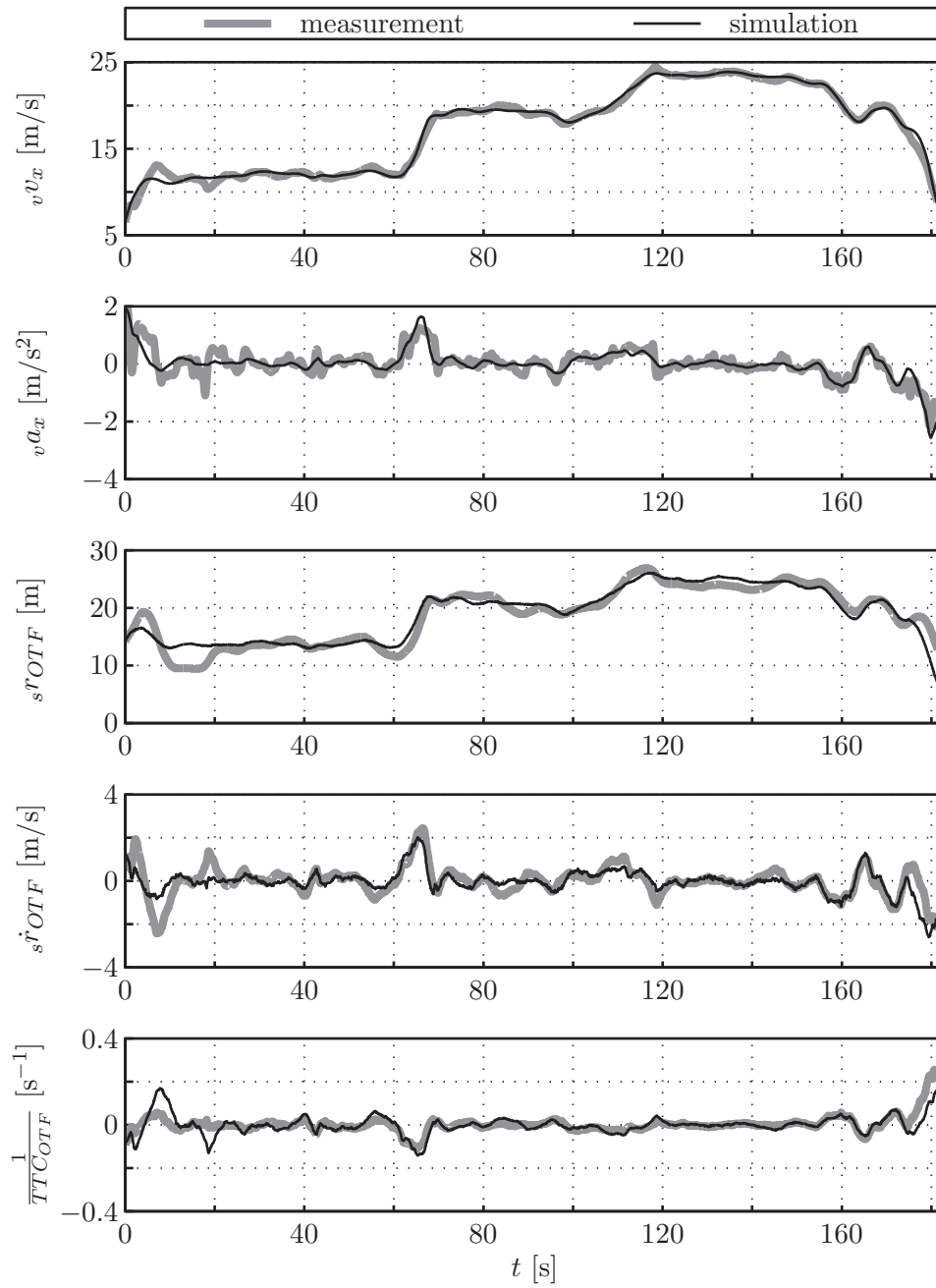The measured motion of the OTF was fed into the simulation tool CarMaker. The ego

Figure 6.12.: Comparison of measurements and simulation with parameters of eq. (6.31)
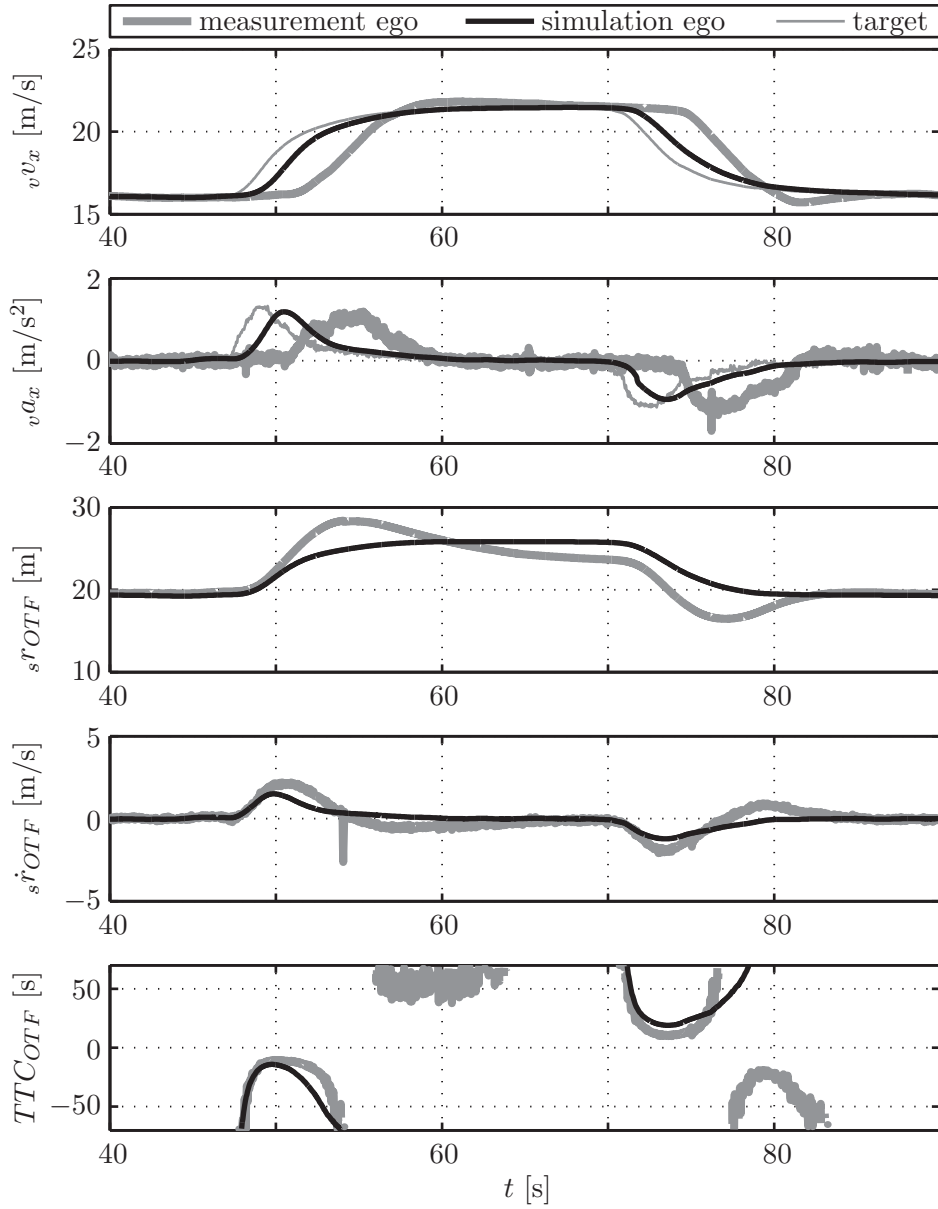
Figure 6.13.: Comparison of measurements of an ACC-equipped vehicle and simulation with parameters of eq. (6.31)

vehicle was positioned with its initial speed from the measurement at the measured distance behind the OTF. The desired speed is set to $v_{set} = 100\,\text{km/h}$, and the desired time gap to $\tau_{set} = 1.2\,\text{s}$, as recorded in the measurement. Figure 6.13 shows the comparison between the measurement and the simulation for the longitudinal vehicle speed $_v v_x$, the longitudinal vehicle acceleration $_v a_x$, and the inter-vehicle distance $_s r_{OTF}$ and range rate $_s \dot{r}_{OTF}$ and TTC_{OTF}. In the simulation, the ACC vehicle begins to accelerate earlier than in reality. As a result, with the same level of maximum acceleration, the vehicle in reality has an overshoot in speed and in the inter-vehicle distance signals. That is not the case in the simulation. Due to the small levels of acceleration and deceleration of the OTF, the overshoot in the real measured data may be critical. Dangerous situations may occur if the OTF performs a hard deceleration manoeuvre. The delay for the acceleration manoeuvre is not critical because it will never lead to a critical situation. For both manoeuvres, the difference in time is nearly the same at about $3\,\text{s}$. The measured ACC vehicle may suppress the deceleration command until a certain TTC is reached. At the measured vehicle, it begins to decelerate at $TTC_{OTF} \approx 10\,\text{s}$. Fancher et al. described in [FBE01] that drivers become anxious if the TTC falls below 9 to $10\,\text{s}$. Thus, the measured ACC vehicle is near the given boundary, and some drivers may feel scared. In comparison, the simulated ACC system begins to decelerate even at small inter-vehicle velocities, resulting in a $TTC_{OTF} \approx 69\,\text{s}$, see fig. 6.13. If it is necessary to delay the beginning of the deceleration, this could easily be implemented in the controller. The desired acceleration of the ACC controller should only be suppressed until the first time TTC falls below the defined limit.

Since simulations cannot answer questions about which of the two behaviours drivers prefer, simulator tests or real test drives have to be performed with both settings and a high number of probands. This will lead to the problem that even if most of the probands prefer one setting, there will still be drivers who prefer the other setting. A compromise for dealing with this problem is that both settings are made available in the vehicle, which has already been implemented in production vehicles. Drivers must select their preferred setting via the *Human-Machine Interface* (HMI).

To sum up, the identified parameters meet all the requirements. String stability is guaranteed, the motion of the ego vehicle in the measurements is nearly duplicated by the ACC-equipped vehicle, and the performance of the system is similar to a production vehicle equipped with an ACC system. The identification itself is fast, if the required measurements are available. The big advantage is that if the measurements have already been made, the data can be used to parametrize controller types other than the one used in this work. In the future, the identified parameters should be evaluated on a driving simulator.

7

Summary and Conclusion

This chapter provides a summary of the present thesis and a final statement.

Chapter 1: Introduction. In the first chapter, the term *Advanced Driver Assistance System* (ADAS) was defined. Additionally, different options for categorizing ADAS were listed. Not so long ago, ADAS were only available in upper vehicle segments. However, in 2010, the European Union set the goal to halve the road fatalities by the year 2020. They stated that this would only be possible if ADAS became standard vehicle equipment. Thus, ADAS have become available even in the lower vehicle segments, and cost and time-efficient development and validation methods are needed.

Chapter 2: Adaptive Cruise Control. The presented research focused on *Adaptive Cruise Control* (ACC) systems. This chapter described the main parts of such a system. ACC systems consist of sensors, actuators, controllers and the *Human-Machine Interface* (HMI). The performance of an ACC system depends strongly on the performance of the environmental-recognition sensors and the controllers. *Radio Detection and Ranging* (RADAR) sensors are frequently used as environmental-recognition sensors. There are different RADAR sensor concepts available on the market, which were described in detail. Additionally, other environmental-recognition sensors were described, such as *Light Detection and Ranging* (LIDAR), *video cameras*, *Vehicle-to-Vehicle Communication* (V2V) and *Vehicle-to-Infrastructure Communication* (V2I). The advantages of RADAR sensors are the detection range, the resistance to environmental influences, and the accurate measurement of the relative velocity of an object. Nevertheless, another sensor type might replace RADAR sensors if its performance becomes better. There are already vehicles that use camera systems instead of RADAR sensors due to lower costs. Furthermore, different upper level controllers out of the literature were compared in simulation, including the *Continuous Time Gap* (CTG) control, *Model Predictive Control*

(MPC), *fuzzy* control and *Sliding Mode Control* (SMC), each of which showed different behaviour. The best performance is delivered by the CTG controller and the SMC.

Chapter 3: Development Process. This chapter described the *V-Model*, which is the common development process for electric and electronic systems. The development of ADAS is a trade-off between shortening the development and validation time to save costs and delivering a system that satisfies the customer. The main problem is that not all situations that might occur can be tested. This may lead to an infinite number of test cases. To achieve a high number of tests within a short time, *Hardware-in-the-Loop* (HIL) and *Model-in-the-Loop* (MIL) tests were used. Although they cannot completely replace expensive, time-consuming real vehicle tests, they can reduce the number of such tests required.

Chapter 4: Measurements. Tests with non-professional test drivers and a specially equipped vehicle were carried out. The probands drove a vehicle called the ego vehicle, with a production RADAR sensor mounted on its front. Additionally, an extended vehicle dynamics measurement system was mounted on the ego vehicle and on another vehicle. With this measurement system, the relative motion between the ego vehicle and the other vehicle was measured with an accuracy of a few centimetres. With this measurement setup, a basic and proband study were conducted. Twelve different drivers travelled an overall distance of 445.4 km on a defined route in and around the city of Graz. Since the tests were done on public roads, the side slip angle could not be measured directly. Therefore, a linear observer was created, which delivered satisfying results.

Chapter 5: Selection of the Object to Follow. This chapter compared different path prediction and object selection algorithms. This study was based on the measurements made in chapter 4. The evaluated path prediction algorithms were *constant curvature algorithms* and algorithms based on the linear *Single-Track Model* (STM). The constant curvature algorithms predict the vehicle path with the hypothesis that the actual measured curvature of the path will stay constant in the future. The input for the linear STM was the steering angle, and the output was the predicted side slip angle and the vehicle yaw rate. First, the actual steering angle was set constant for the input of the STM. As a second option, a novel steering angle prediction algorithm was developed, which was used as an input for the STM. These path prediction algorithms were applied to all time steps of the measurement. The predicted paths were compared to the driven paths, using the measurement data recorded during the test drives described in chapter 4. The prediction was performed for two time horizons. For a short prediction time of three seconds, there was hardly any difference between the algorithms. Three seconds is a typical prediction time for safety systems, such as *Forward Collision Warning* (FCW) and *Automatic Emergency Brake* (AEB) systems. At the long prediction horizon of ten seconds, there were differences in the evaluation. The best option was the combination of the new steering algorithm and the linear STM. A prediction time of ten seconds is important for ACC systems.

The predicted path was used to select the *Object to Follow* (OTF). There, two different object selection algorithms were compared. The simplest one selects the nearest object

in the predicted path, while the second one assigns a priority to every object in the predicted path. The object with the highest priority is used as the OTF. This *priority algorithm* seemed to handle the error that arises during the path prediction better than the first algorithm, especially when passing another vehicle at low lateral distances. Thus, the novel steering prediction algorithm in combination with the linear STM was used to predict the ego vehicle's path. The OTF was selected by applying the priority algorithm.

Chapter 6: Upper Level Controller Parameter Identification. Based on the OTF selected in chapter 5, the parameters for a novel ACC algorithm based on the CTG controller were identified. The proposed parametrization of this controller led to the problem that if it was a string stable parametrization, the comfort did not satisfy the driver, and vice versa. Therefore, a new algorithm was developed to deal with this problem.

The parameter identification was performed in three steps. First the stopping distance behind an OTF was identified. The resulting constant correlates very well with the literature. As a second step, the time gap at which the driver was following the proceeding vehicle was identified. To this end, the appropriate parts of the measurements have to be selected. This is done with the inverse of the *Time to Collision* (TTC), which is an indicator for constant following manoeuvres. As a third and final part, the four parameters needed to parametrize the controller were identified. To this end, the *Simplex Method* of *Nelder-Mead* was modified to deal with limited solutions for the parameters.

The identified parameters were verified in simulation. First, string stability was proven. Due to the non-linear terms in the controller, it could not be proven analytically. Therefore, simulations were performed, and string stability was guaranteed. The performance of the controller was also checked by simulating the manoeuvres recorded with the probands. The comparison was done between the data recorded with a proband driver and the simulation with a simplified longitudinal vehicle model that was controlled by the ACC controller. The recorded and simulated data showed acceptable similarity. As a last step, simulations were compared to measurements made with a production vehicle equipped with an ACC system. The movement of the OTF was fed into a commercially available simulation tool. These simulations showed that the shape of the simulated movement was similar to the measured one. The only difference was that the production ACC vehicle began to decelerate and accelerate later than the newly developed controller. The aim of this comparison was not to achieve exactly the same behaviour, but rather to have similar signal shapes. In addition, the comparison showed that the real ACC vehicle had an undershoot in the inter-vehicle distance, while the simulated controller had none. The simulation cannot determine which of the two controllers people preferred. Therefore, simulator tests or real test drives have to be performed.

Final statement: The presented work provides a well-grounded analysis of existing ACC systems. The evaluation methods described could be used to further develop ADAS algorithms. One example for an improvement is the novel steering angle prediction algorithm, which showed the best results in combination with the linear STM in the evaluation of the path prediction algorithms. It is possible to use the predicted steering

angle with any other algorithm that requires such an input.

The proband study on public roads was a first step in building up a database that represents human driving behaviour, which could be used for future development of ADAS algorithms. The research has demonstrated that the new ACC controller showed the desired human-like behaviour in following another vehicle. This will increase driver acceptance, which, along with increased traffic safety, must be one of the primary goals of newly developed ADAS functionalities.

A

Description of Available Systems

This chapter provides a very rough description of the available *Advanced Driver Assistance System* (ADAS). The systems are grouped to form a short and clear list. Although car manufacturers may give their systems different names, the following paragraphs describe the basic concepts behind the different types of systems.

A.1. ACC and FSRA

Adaptive Cruise Control (ACC) and *Stop-and-Go Adaptive Cruise Control* (FSRA) are systems that support drivers in their driving tasks. The systems hold the vehicle at a set speed and ensure a set inter-vehicle distance from a proceeding slower moving vehicle. The difference between ACC and FSRA is that FSRA systems are able to control the vehicle to zero speed, whereas ACC system only work above a defined minimum speed. Both systems are comfort-oriented systems. A detailed description of ACC and FSRA systems is given in chapter 2.

A.2. FCW and AEB

Forward Collision Warning (FCW) and *Automatic Emergency Brake* (AEB) systems are safety-oriented systems that help to prevent accidents or mitigate the severity of accidents. FCW systems just warn the driver of a potential rear-end collision, while AEB systems also apply the brakes. There are already various versions of AEB systems available on the market. Some of them perform partial braking, some use full braking,

and others combine the two braking functions. One special system is the so-called *City Safety System*, which also reacts to pedestrians, which is normally not the case for AEB systems.

A.3. LDW, LKA and LKS

Lane-Departure Warning (LDW) and *Lane-Keeping Assistant* (LKA) systems help the driver prevent unintentional lane departures. Thus, these systems are primarily safety-oriented system. However, there are systems available that focus on increasing the comfort as well. LDW systems warn drivers if they are about to depart from the lane without using the turn indicator. LKA systems also apply the brakes or apply steering torque to the steering column to steer the vehicle back into its lane. The abovementioned comfort-oriented system is only possible if the intervention is done via the vehicle steering. This kind of system is called *Lane-Keeping Support* (LKS).

A.4. LSF

Low-Speed Following (LSF) systems control the vehicle in the longitudinal and lateral directions. They follow the proceeding vehicle at low speeds to support the driver in traffic jams. These systems can be seen as a combination of FSRA and LKS systems.

A.5. PA

Parking Assistant (PA) systems support the driver in parking the vehicle. There are different levels of PA systems available. The easiest one just provides acoustic or visual information about the distance between the vehicle and other objects. On the highest level available, systems park the vehicle semi-automatically. This means that the driver is still responsible for his vehicle, but the vehicle performs nearly all actions (e. g. steering, acceleration and deceleration). The driver has to monitor the system intervene if the system is about to fail.

A.6. BSM

Blind-Spot Monitoring (BSM) systems warn the driver against collisions that may occur due to lane change manoeuvres. The system can be divided into two different functionalities. The first one is pure BSM, where the system only warns if another object is driving in the blind spot of the vehicle and cannot be seen with the vehicle mirrors. The second one also detects closing vehicles that approach the driver's vehicle very quickly. Although

such vehicles are technically visible in the vehicle mirrors, the driver may overlook them due to the rapid approach.

A.7. PIS

Perception Improvement Systems (PIS) support the driver in cognition of the environment. Different systems are already available, such as automatic or adaptive headlights, marking objects with a light beam or night vision systems. For night vision systems, two different approaches are possible. One is the so-called residual light amplifier, which is a passive system. Here, very weak light that cannot be detected by the human eye is detected, and the resulting picture is displayed on a monitor in the vehicle. The second type is an active system, where near-infrared light is emitted by the vehicle. The reflected light is then detected and a picture is created, which is also displayed on a monitor.

A.8. DVM

Very often, long monotonous rides result in driver distraction. *Driver-Vigilance Monitoring* (DVM) systems warn drivers if their attention wanders. These assistance systems are very important for every system in which the driver is out of the loop, but is still responsible for the car and has to monitor it.

A.9. NS

Navigation Systems (NS) help the driver find the correct route to a desired destination. This leads to less stress during driving, which has the positive effect that the driver can focus on the driving tasks of guidance and stabilization, see chapter 1.

<div style="text-align: right; font-size: 4em; font-weight: bold; color: gray;">B</div>

Vehicle Dynamics

B.1. Lateral Vehicle Dynamics

The *Single-Track Model* (STM), illustrated in fig. B.1, is frequently used to model the lateral dynamics of the vehicle for controller design. It was introduced by Riekert et al. in the year 1940, [RS40]. According to [HW10], the simplifications for this model are that

1. both wheels of each axle are located at the centre line of the vehicle,

2. the *Center of Gravity* (CG) height equals zero $h_{CG} = 0$,

3. only small lateral accelerations $_va_y \leq 4\,\text{m/s}^2$ occur,

4. the steering angle is small $\delta \ll 1\,\text{rad}$, and

5. the longitudinal vehicle speed $_vv_x$ is constant.

In general, the equation of motion for the STM of fig. B.1 reads

$$\begin{bmatrix} m & 0 & 0 \\ 0 & m & 0 \\ 0 & 0 & _vI_{zz} \end{bmatrix} \begin{bmatrix} _v\dot{v}_x \\ _v\dot{v}_y \\ _v\dot{\omega}_z \end{bmatrix} = m \begin{bmatrix} _v\omega_z\,_vv_y \\ -_v\omega_z\,_vv_x \\ 0 \end{bmatrix} + 2 \begin{bmatrix} _{vf}F_x + _{vr}F_x \\ _{vf}F_y + _{vr}F_y \\ _{vf}F_y\,l_f - _{vr}F_y\,l_r \end{bmatrix}, \qquad \text{(B.1)}$$

where m describes the vehicle mass and $_vI_{zz}$ the moment of inertia of the vehicle around the $_vz$-axis. The state variables $_vv_x$, $_vv_y$ and $_v\omega_z$ are the translatoric and rotational speeds of the vehicle in the $(_0x, _0y)$ plane of the global coordinate system. The dimensions l_f and l_r are the distances between the CG and the front and rear axle. The wheel forces
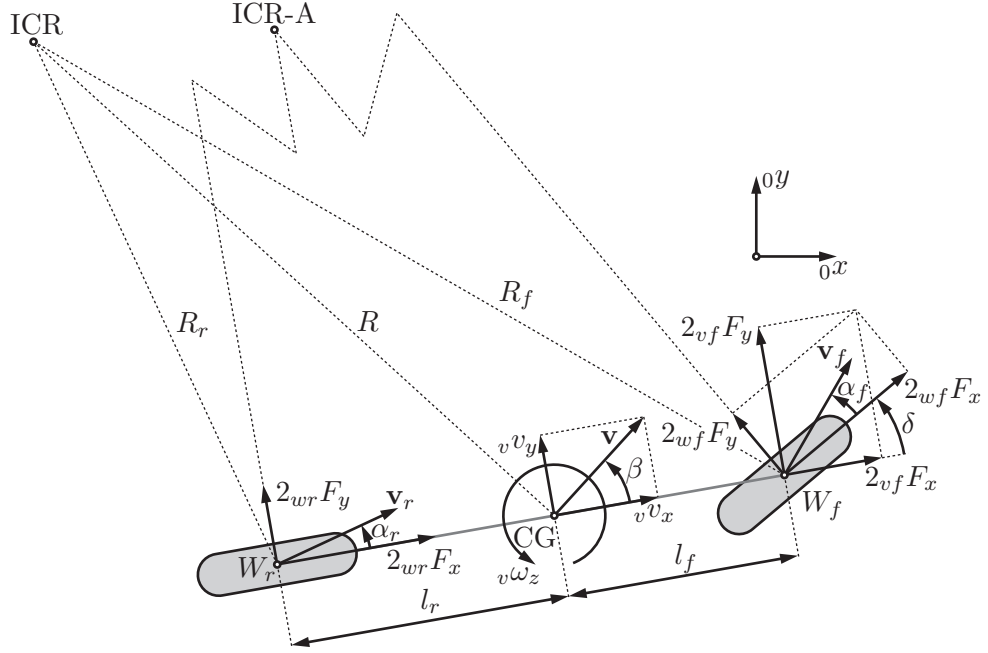
Figure B.1.: Single-Track Model, [HW10]

$_{vf}F_x$, $_{vf}F_y$, $_{vr}F_x$ and $_{vr}F_y$, measured in the vehicle coordinate system $(_vx, _vy)$, act in the patch between wheel and road surface, [HW10].

Assumptions 1 and 2 lead to constant wheel loads and no pitch or roll movement of the vehicle during the simulation.

Due to simplification 3, a linear tyre model that reads

$$_wF_y = -c_y\,\alpha \tag{B.2}$$

can be used. The side slip angle is defined as

$$\alpha = \arctan\left(\frac{_wv_y}{_wv_x}\right), \tag{B.3}$$

where the velocities in the front tyre coordinate systems are defined by

$$\underbrace{\begin{bmatrix} _{wf}v_x \\ _{wf}v_y \end{bmatrix}}_{_{wf}\mathbf{v}_f} = \underbrace{\begin{bmatrix} \cos\delta & \sin\delta \\ -\sin\delta & \cos\delta \end{bmatrix}}_{\mathbf{T}_{wf,v}} \underbrace{\begin{bmatrix} _vv_x \\ _vv_y + {}_v\omega_z\,l_f \end{bmatrix}}_{_v\mathbf{v}_f} \tag{B.4}$$

and the velocities for the rear tyres are given by

$$\underbrace{\begin{bmatrix} _{wr}v_x \\ _{wr}v_y \end{bmatrix}}_{_{wr}\mathbf{v}_r} = \underbrace{\begin{bmatrix} _vv_x \\ _vv_y - {}_v\omega_z\,l_r \end{bmatrix}}_{_v\mathbf{v}_r}. \tag{B.5}$$

The tyre stiffness equals the initial slope of the tyre characteristics $c_y = dF_0$, as illustrated in fig. B.2(a).

The transformation of the front tyre forces from the W_f to the vehicle-coordinate system can be done using the formulation

$$
\begin{bmatrix} {}_{vf}F_x \\ {}_{vf}F_y \end{bmatrix} = \underbrace{\begin{bmatrix} \cos\delta & -\sin\delta \\ \sin\delta & \cos\delta \end{bmatrix}}_{\mathbf{T}_{v,wf}=\mathbf{T}_{wf,v}^{-1}} \begin{bmatrix} {}_{wf}F_x \\ {}_{wf}F_y \end{bmatrix}.
\tag{B.6}
$$

Using assumption 4, the transformation described in eq. (B.6) can be simplified using $\cos\delta \approx 1$ and $\sin\delta \approx \delta$.

The constant longitudinal velocity of simplification 5 means ${}_v\dot{v}_x = 0$, and therefore the first row of eq. (B.1) is omitted.

The state variable ${}_vv_y$ in eq. (B.1) is substituted by the side slip angle in the CG, which reads

$$
\beta = \arctan\left(\frac{{}_vv_y}{{}_vv_x}\right).
\tag{B.7}
$$

Simplifications 3 and 4 lead to small side slip angles. Therefore eq. (B.7) can be redefined to $\beta \approx \left(\frac{{}_vv_y}{{}_vv_x}\right)$ for $\beta \ll 1\,\text{rad}$.

All these assumptions lead to the linear STM, which reads

$$
\underbrace{\begin{bmatrix} \dot{\beta} \\ \dot{\omega}_z \end{bmatrix}}_{\dot{\mathbf{x}}} = \underbrace{\begin{bmatrix} -\dfrac{2\left({}_fc_y+{}_rc_y\right)}{m\ {}_vv_x} & \dfrac{2\left({}_rc_y\ l_r-{}_fc_y\ l_f\right)}{m\ {}_vv_x^2} - 1 \\ \dfrac{2\left({}_rc_y\ l_r-{}_fc_y\ l_f\right)}{{}_vI_{zz}} & -\dfrac{2\left({}_fc_y\ l_f^2+{}_rc_y\ l_r^2\right)}{{}_vI_{zz}\ {}_vv_x} \end{bmatrix}}_{\mathbf{A}} \underbrace{\begin{bmatrix} \beta \\ \omega_z \end{bmatrix}}_{\mathbf{x}} + \underbrace{\begin{bmatrix} \dfrac{2{}_fc_y}{m\ {}_vv_x} \\ \dfrac{2{}_fc_y\ l_f}{{}_vI_{zz}} \end{bmatrix}}_{\mathbf{b}} \underbrace{\delta}_{u}.
\tag{B.8}
$$

B.2. Non-linear Tyre Model

The *TMsimple* tyre model is used to calculate the forces in the contact patch between tyre and road. The model described in this chapter is based on the publication [Hir09] of Hirschberg.

The tyre forces are a function of the slip between tyre and road surface in the contact patch. The longitudinal tyre force is a function of the longitudinal slip, which reads

$$
s_x = \frac{{}_c\omega_y\ r_e - {}_wv_x}{\max\left({}_wv_x,\ {}_c\omega_y\ r_e,\ {}_wv_{x\varepsilon}\right)},
\tag{B.9}
$$

where ${}_c\omega_y$ is the rotational speed of the tyre, r_e describes the effective tyre radius, and ${}_wv_x$ is the speed of the W-point in the x-direction of the tyre coordinate system. The tyre parameter ${}_wv_{x\varepsilon}$ avoids division by zero when ${}_c\omega_y = 0$ and ${}_wv_x = 0$, by limiting the denominator to a minimum value of ${}_wv_{x\varepsilon}$. The lateral slip is defined in eq. (B.3).
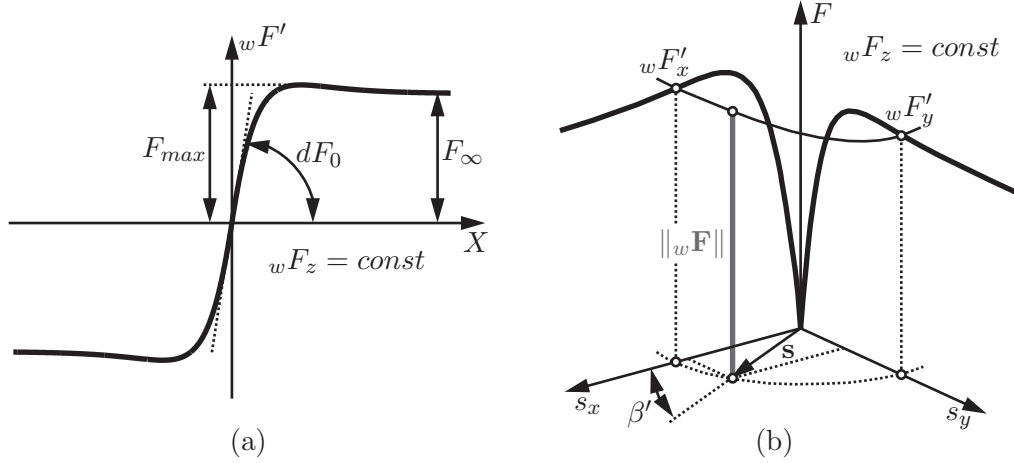
Figure B.2.: (a) Tyre characteristics for pure longitudinal or lateral tyre forces for constant tyre load $_wF_z$ and (b) combined longitudinal and lateral tyre forces with generalized slip **s**, both according to [Hir09]

In TMsimple, the pure longitudinal or lateral tyre force $_wF'$ is described by

$$_wF' = K \, \sin\left[B\left(1 - \mathrm{e}^{\frac{-|X|}{A}}\right) \mathrm{sign}\,(X)\right]. \tag{B.10}$$

The variable X in eq. (B.10) is the corresponding slip quantity. For the longitudinal force, the slip reads $X = s_x$, see eq. (B.9). In the lateral direction, the slip is defined as $X = \alpha$, according to eq. (B.3). The parameters K, B and A are described in eq. (B.11), and fig. B.2(a) shows the physical parameters F_{max}, F_∞ and dY_0.

$$K = F_{max}$$
$$B = \pi - \arcsin\left(\frac{F_\infty}{F_{max}}\right) \tag{B.11}$$
$$A = \frac{1}{dY_0} \, K \, B$$

For the combined lateral and longitudinal tyre forces, the side slip angle α is transformed to have the same unit as the longitudinal slip s_x reaching the same initial stiffnes of the characteristics. The transformation is done using

$$s_y = \frac{\alpha}{G\left(F_z\right)}, \tag{B.12}$$

where the weighting factor is defined as $G\left(F_z\right) = \frac{dF_{x0}(_wF_z)}{dF_{y0}(_wF_z)}$. Using the transformation described in eq. (B.12), the generalized slip vector is introduced, which reads $\mathbf{s} = \begin{bmatrix} s_x & s_y \end{bmatrix}^\mathrm{T}$,

with its norm $\|\mathbf{s}\| = \sqrt{s_x^2 + s_y^2}$. If the norm of the generalized slip $\|\mathbf{s}\|$ only acts in the longitudinal or lateral direction, the contact forces ${}_wF_x'$ and ${}_wF_y'$ will occur, see fig. B.2(b). These pure longitudinal or lateral forces are combined using the interpolation

$$\|{}_w\mathbf{F}\| = \frac{1}{2} \left[{}_wF_x' + {}_wF_y' + \left({}_wF_x' - {}_wF_y' \right) \cos\left(2\beta' \right) \right], \tag{B.13}$$

where $\beta' = \arctan\left(\frac{s_y}{s_x}\right)$, see fig. B.2(b). The $\cos\left(2\beta'\right)$ function is used to obtain a continuous interpolation with a horizontal tangent at ${}_wF_x'$ and ${}_wF_y'$. The resulting tyre force in the tyre coordinate system in the ${}_wx$ and ${}_wy$ directions reads

$$_w\mathbf{F} = \|{}_w\mathbf{F}\| \begin{bmatrix} \cos\left(\beta'\right) \\ \sin\left(\beta'\right) \end{bmatrix}. \tag{B.14}$$

All the calculations up to now were done using the nominal wheel loads ${}_wF_{z,nom}$. For other wheel loads ${}_wF_z$, the parameters described in B.2(a) are modified using the expressions

$$F_{max}\left({}_wF_z\right) = a_1 \frac{{}_wF_z}{F_{z,nom}} + a_2 \left(\frac{{}_wF_z}{F_{z,nom}} \right)^2,$$

$$dF_0\left({}_wF_z\right) = b_1 \frac{{}_wF_z}{F_{z,nom}} + b_2 \left(\frac{{}_wF_z}{F_{z,nom}} \right)^2 \text{ and}$$

$$F_\infty\left({}_wF_z\right) = c_1 \frac{{}_wF_z}{F_{z,nom}} + c_2 \left(\frac{{}_wF_z}{F_{z,nom}} \right)^2, \tag{B.15}$$

with

$$a_1 = 2\, F_{max} - \frac{1}{2} F_{max,2} \qquad\qquad a_2 = \frac{1}{2} F_{max,2} - F_{max},$$

$$b_1 = 2\, dF_0 - \frac{1}{2} dF_{0,2} \qquad\qquad b_2 = \frac{1}{2} dF_{0,2} - dF_0 \text{ and}$$

$$c_1 = 2\, F_\infty - \frac{1}{2} F_{\infty,2} \qquad\qquad c_2 = \frac{1}{2} F_{\infty,2} - F_\infty. \tag{B.16}$$

The parameters F_{max}, dF_0 and F_∞ describe the tyre characteristics at a wheel load of $F_{z,nom}$, and the parameters $F_{max,2}$, $dF_{0,2}$ and $F_{\infty,2}$ at $2\, F_{z,nom}$. Table C.5 shows the tyre data used.

B.3. Combined Lateral and Longitudinal Vehicle Dynamics

Combining eqs. (2.16) and (B.1) leads to

$$
\underbrace{\begin{bmatrix} {}_{cf}\dot{\omega}_y \\ {}_{cr}\dot{\omega}_y \\ {}_v\dot{v}_x \\ {}_v\dot{v}_y \\ {}_v\dot{\omega}_z \end{bmatrix}}_{\dot{\mathbf{x}}} = \underbrace{\begin{bmatrix} 0 \\ 0 \\ {}_v\omega_z \,{}_v v_y \\ -{}_v\omega_z \,{}_v v_x \\ 0 \end{bmatrix} + \begin{bmatrix} \frac{1}{I_f}\left({}_{cf}T_y - {}_{cf}T_{y,ro} - {}_{wf}F_x\, r_f\right) \\ \frac{1}{I_r}\left({}_{cr}T_y - {}_{cr}T_{y,ro} - {}_{wr}F_x\, r_r\right) \\ \frac{1}{m}\left(2\,{}_{wf}F_x + 2\,{}_{wr}F_x - F_a\right) \\ \frac{2}{m}\left({}_{wf}F_y + {}_{wr}F_y\right) \\ \frac{2}{{}_v I_{zz}}\left({}_{wf}F_y\, l_f + {}_{wr}F_y\, l_r\right) \end{bmatrix}}_{\mathbf{f}(\mathbf{x},\delta,u_d,u_b)}
\tag{B.17}
$$

with five *Degrees of Freedom* (DOFs), the rotational speed of the front and rear wheels, ${}_{cf}\omega_y$, ${}_{cr}\omega_y$, the longitudinal and lateral vehicle speed, ${}_v v_x$, ${}_v v_y$ and the yaw rate ${}_v\omega_z$. The tyre forces ${}_{wf}F_x$, ${}_{wr}F_x$, ${}_{wf}F_y$ and ${}_{wr}F_x$ are calculated using eqs. (B.3) to (B.6) and the tyre model described in appendix B.2. The wheel torque ${}_{cf}T_y$ and ${}_{cf}T_y$ consists of the drive torque for the front and rear wheels ${}_{cf}T_d$, ${}_{cr}T_d$ and the brake torque on each axle ${}_{cf}T_b$, ${}_{cr}T_b$, described in eqs. (2.19) and (2.21). The air drag is given in eq. (2.14). The input for the model is the steering angle δ, the gas pedal position u_d and the brake actuation u_b.

C

Model Parameters

C.1. Controller Parameters

This chapter provides the parameters used for the controllers in the simulations of chapter 2.4.4.

Table C.1.: Data for the simulation of the CTG controller

Parameter	Value
k	2.5

Table C.2.: Data for the simulation of the MPC controller

Parameter	Value
T	$0.1\,\mathrm{s}$
N_p	70
N_c	1
$\mathbf{R}$	$\begin{bmatrix} 1 & 0 & 0 \\ 0 & 1 & 0 \\ 0 & 0 & 1 \end{bmatrix}$
$\mathbf{y}_{des}$	$\begin{bmatrix} 0 \\ 0 \end{bmatrix}$

Table C.3.: Data for the simulation of the SMC controller

Parameter	Value
r	$\begin{bmatrix} 1 \\ 1.5 \\ 3 \end{bmatrix}$
q	0.1
k	1

C.2. Vehicle and Tyre Parameters

The vehicle simulations were carried out with the vehicle data from table C.4 and the tyre parameters from table C.5.

Table C.4.: Vehicle data according to [Lexss]

Parameter	Value	Unit
m	1796	[kg]
$_v I_{zz}$	3006	[kgm^2]
l_f	1.337	[m]
l_r	1.471	[m]
h_{CG}	0.549	[m]
b_f	1.564	[m]
b_r	1.551	[m]
A_x	2.2	[m^2]
c_a	0.273	[-]

Table C.5.: Tyre data according to [Lexss]

Parameter		Value at		Unit
		$F_{z,nom}$	$2F_{z,nom}$	
Long.	$F_{max,x}$	3789	6688	[N]
	$F_{\infty,x}$	2809	4890	[N]
	$dF_{0,x}$	1963	3021	[N/%]
Lat.	$F_{max,y}$	3799	6581	[N]
	$F_{\infty,y}$	3565	5898	[N]
	$dF_{0,y}$	54028	94461	[N/rad]
$F_{z,nom}$		3000		[N]
f_r		0.01		[-]
r_0		0.3266		[m]
$_f c_{y,0}$		77500		[N/rad]
$_r c_{y,0}$		77500		[N/rad]
$c_{y,e}$		10000		[N/rad]
$_w v_{x\varepsilon}$		0.01		[m/s]

D

Sensor Position for the Measurements

Figure D.1 shows the position of the sensors in the ego and target vehicles for the measurements described in chapter 4.
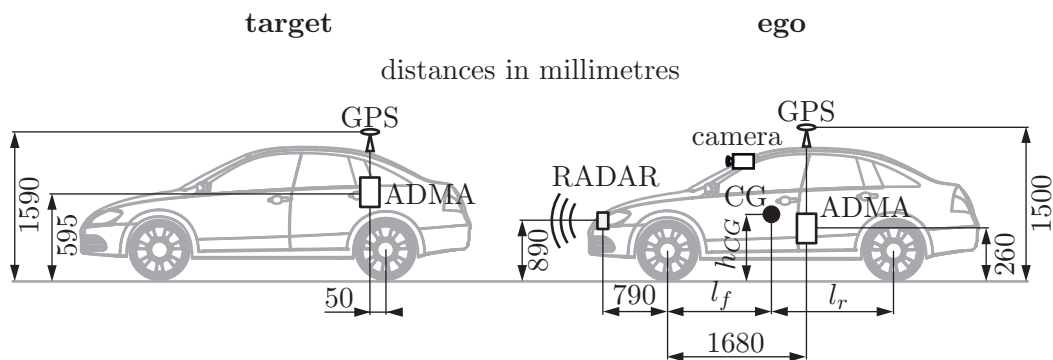
Figure D.1.: Positions of the sensors, all distances in millimetres

E

Simplex Method by Nelder-Mead

This description of the method is based on the lecture of Oberle, [Obe12]. The objective in the given example is to minimize $f(\mathbf{P})$ with respect to the parameters $\mathbf{P} = \begin{bmatrix} P_1 & P_2 & \cdots & P_{n_P} \end{bmatrix}^{\mathrm{T}}$. The idea behind this method is to calculate the function value $f(\mathbf{P})$ for $n_P + 1$ parameter sets, which are called simplex. The maximum function value is replaced by a new function value. This process is repeated until an exit condition is fulfilled.

Figure E.1 shows the different steps. The method was limited to two parameters ($n_P = 2$) in order to provide good visualization in two-dimensional plots. It could be easily extended for more parameters due to the compact notation in vector form.

The first step is to calculate the function values for a set of $n_P + 1$. The function values are sorted according to the rule

$$f(\mathbf{P}_b) < f(\mathbf{P}_{ib}) < f(\mathbf{P}_w),\tag{E.1}$$

where the index b means *best*, ib means *in between*, and w means *worst*. In the next step, the mean value of the parameters, excluding the worst one, are calculated, which reads

$$\bar{\mathbf{P}} = \frac{1}{n_P} \sum_{i \neq w} \mathbf{P}_i.\tag{E.2}$$

A new parameter set is generated by the reflection of $\mathbf{P}_w$ at $\bar{\mathbf{P}}$ by using

$$\mathbf{P}_{n1} = \bar{\mathbf{P}} + \alpha \left(\bar{\mathbf{P}} - \mathbf{P}_w \right).\tag{E.3}$$
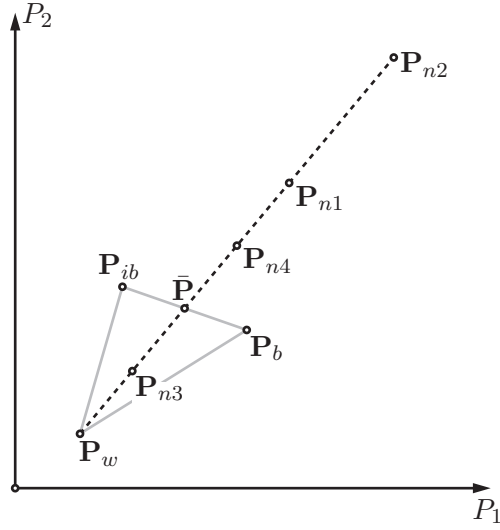
Figure E.1.: Nelder-Mead method for an optimization problem with $n_P = 2$, based on [Obe12]

In general, the reflection parameter is set to $\alpha = 1$. If $f(\mathbf{P}_b) < f(\mathbf{P}_{n1}) < f(\mathbf{P}_{ib})$, then $\mathbf{P}_w$ is replaced by $\mathbf{P}_{n1}$. Furthermore, if $f(\mathbf{P}_{n1}) < f(\mathbf{P}_b)$, then the expansion point

$$\mathbf{P}_{n2} = \bar{\mathbf{P}} + \beta \left(\bar{\mathbf{P}} - \mathbf{P}_w \right) \tag{E.4}$$

is calculated, where the expansion parameter has to fulfil the condition $\beta > \alpha$. If $f(\mathbf{P}_{n2}) < f(\mathbf{P}_{n1})$, then $\mathbf{P}_w$ is replaced by $\mathbf{P}_{n2}$; otherwise, $\mathbf{P}_{n1}$ is used.

If $f(\mathbf{P}_{n1}) > f(\mathbf{P}_{ib})$, then the contraction points $\mathbf{P}_{n3}$ or $\mathbf{P}_{n4}$ are calculated. The condition $f(\mathbf{P}_{n1}) > f(\mathbf{P}_w)$ leads to the contraction point

$$\mathbf{P}_{n3} = \bar{\mathbf{P}} + \gamma \left(\bar{\mathbf{P}} - \mathbf{P}_w \right) \tag{E.5}$$

and condition $f(\mathbf{P}_{n1}) < f(\mathbf{P}_w)$ leads to

$$\mathbf{P}_{n4} = \bar{\mathbf{P}} - \gamma \left(\bar{\mathbf{P}} - \mathbf{P}_w \right), \tag{E.6}$$

where in both cases $\gamma < \alpha$. If $f(\mathbf{P}_{n3}) < f(\mathbf{P}_w)$ or $f(\mathbf{P}_{n3}) < f(\mathbf{P}_w)$, then $\mathbf{P}_w$ is replaced by $\mathbf{P}_{n3}$ or $\mathbf{P}_{n4}$; otherwise, the simplex is shrunk around $\mathbf{P}_b$ reading

$$\mathbf{P}_i = \frac{\mathbf{P}_i + \mathbf{P}_b}{2}. \tag{E.7}$$

In general, the parameters $\alpha = 1$, $\beta = 2$ and $\gamma = 0.5$ are used. These steps are repeated until one of the exit conditions is fulfilled. The first one considers the change of the norm of two consecutive parameter vectors reading

$$\left\| {}^{is-1}\mathbf{P} - {}^{is}\mathbf{P} \right\| \leq \varepsilon_P, \tag{E.8}$$

where $^{is-1}\mathbf{P}$ is the parameter set of the previous iteration of $^{is}\mathbf{P}$. Another exit condition is related to the absolute change of the function value between two iteration steps reading

$$\left| f\left(^{is-1}\mathbf{P}\right) - f\left(^{is}\mathbf{P}\right) \right| \leq \varepsilon_f. \tag{E.9}$$

The iteration process is executed for the time when the condition

$$is \leq is_{max} \tag{E.10}$$

is fulfilled, which means that the iteration process is stopped if the number of iterations is reaches a defined maximum is_{max}.

List of Figures

List of Tables

Bibliography

[ABF+03]   K. Athanasas, C. Bonnet, H. Fritz, C. Scheidler, and G. Volk. VALSE- Validation of Safety-related Driver Assistance Systems. In *Proceedings of IEEE Intelligent Vehicles Symposium*, pages 610–615, June 9-11 2003. Columbus.

[Ada09a]   J. Adamy. *Fuzzy-Control*, chapter 5.3, pages 266–285. Nichtlineare Regelungen. Springer, Berlin, 1 edition, 2009.

[Ada09b]   J. Adamy. *Strukturvariable Regelungen im Gleitzustand*, chapter 5.2, pages 249–265. Nichtlineare Regelungen. Springer, Berlin, 1 edition, 2009.

[Ali10]   Z. Ali. Transitional Controller Design for Adaptive Cruise Control Systems. Dissertation, 2010. University of Nottingham.

[BCLT08]   G. Baffet, A. Charara, D. Lechner, and D. Thomas. Experimental evaluation of observers for tire-road forces, sideslip angle and wheel cornering stiffness. *Vehicle System Dynamics*, 46(6):501–520, May 2008.

[BHLSE13]   S. Bernsteiner, R. Holl, D. Lindvai-Soos, and A. Eichberger. Subjective Evaluation of Advanced Driver Assistance Evaluation of Standardized Driving Maneuvers. In *Proceedings of SAE 2013 World Congress*, pages 1–11. SAE International, April 16-18 2013. Detroit.

[BLR09]   B. Buxbaum, R. Lange, and T. Ringbeck. *3D-Imaging*, chapter 14, pages 187–197. Handbuch Fahrerassistenzsysteme. Vieweg+Teubner, Wiesbaden, 1 edition, 2009.

[BMLSE13]   S. Bernsteiner, Z. Magosi, D. Lindvai-Soos, and A. Eichberger. Phänomenologisches Radarsensormodell zur Simulation längsdynamisch regelnder Fahrerassistenzsysteme. In *Proceedings of VDI Electronic Systems for Motor Vehicles*, pages 1–12. VDI Wissensforum GmbH, October 16-17 2013. Baden-Baden.

[Boc09]   T. Bock. *Bewertung von Fahrerassistenzsystemen mittels Vehicle in the Loop-Simulation*, chapter 8, pages 76–83. Handbuch Fahrerassistenzsysteme. Vieweg+Teubner, Wiesbaden, 1 edition, 2009.

[BPSP11]   G. N. Bifulco, L. Pariota, F. Simonelli, and R. Di Pace. Real-time smoothing of car-following data through sensor-fusion techniques. In *Procedia - Social and Behavioral Sciences*, volume 20, pages 524–535, September 6-9 2011. Poznan.

Bibliography

[Bre09]   J. Breuer. *Bewertungsverfahren von Fahrerassistenzsystemen*, chapter 6, pages 55–68. Handbuch Fahrerassistenzsysteme. Vieweg+Teubner, Wiesbaden, 1 edition, 2009.

[CA07]   E. F. Camacho and C. Bordons Alba. *Introduction to Model Predictive Control*, chapter 1, pages 1–11. Model Predictive Control. Springer, London, 2 edition, 2007.

[Cav09]   D. Caveney. Vehicular Path Prediction for Cooperative Driving Applications through Digital Map and Dynamic Vehicle Model Fusion. In *Vehicular Technology Conference Fall*, pages 1–5, 20-23 Septermber 2009. Anchorage.

[DB06]   R. C. Dorf and R. H. Bishop. *Entwurf von Regelungssystemen im Zustandsraum*, chapter 11, pages 879–962. Moderne Regelungssysteme. Pearson Studium, München, 10 edition, 2006.

[Deu94]   Deutsches Institut für Normung (DIN). Fahrzeugdynamik und Fahrverhalten. Standard DIN 70000, DIN, January 1994.

[Don99]   E. Donges. A Conceptual Framework for Active Safety in Road Traffic. *Vehicle System Dynamics*, 32(2-3):113–128, 1999.

[Don09]   E. Donges. *Fahrerverhaltensmodelle*, chapter 2, pages 15–23. Handbuch Fahrerassistenzsysteme. Vieweg+Teubner, Wiesbaden, 1 edition, 2009.

[Dre02]   M. C. Drew. Coordinated Adaptive Cruise Control: Design and Simulation. Dissertation, 2002. University of California.

[dWB99]   C. Canudas de Wit and B. Brogliato. Stability issues for vehicle platooning in automated highway systems. In *Proceedings of the 1999 IEEE International Conference on Control Applications*, volume 2, pages 1377–1382, 22-27 August 1999. Kohala Coast.

[Eco68]   Economic Commission for Europe. Convention on Road Traffic Done at Vienna on 8 November 1968, 1968.

[Eco11]   Economic Commission for Europe. ECE-R 13-H - Uniform Provisions Concerning the Approval of Passenger Cars with Regard to Braking, 2011.

[Eco14]   Economic Commission for Europe. Report of the Sixty-Eighth Session on the Working Party on Road Traffic Safety, 2014.

[Eic11]   A. Eichberger. *Traffic safety systems and their benefit potential*, chapter 3, pages 66–105. Contributions to Primary, Secondary and Integrated Traffic Safety. Verlag Holzhausen GmbH, Austria, 1 edition, 2011.

[Eur12]   European New Car Assessment Program (Euro-NCAP). Assessment Protocoll - Overall Rating, Version 6.0. Testing protocol, Euro-NCAP, July 2012.

[Eur13]   European New Car Assessment Program (Euro-NCAP). Assessment Protocol - Safety Assist, Version 6.0. Testing protocol, Euro-NCAP, July 2013.

[Eur14a]   European Commission. Available at `http://ec.europa.eu/transport/`
             `road_safety/specialist/statistics/index_en.htm`, 2014. Accessed on
             July 24, 2014.

[Eur14b]   European New Car Assessment Program (Euro-NCAP). 2020 Roadmap.
             Testing protocol, Euro-NCAP, June 2014.

[FBE01]   P. Fancher, Z. Bareket, and R. Ervin. Human-Centered Design of an Acc-
             With-Braking and Forward-Crash-Warning System. *Vehicle System Dynam-
             ics*, 36(2-3):203–223, 2001.

[FEF14]   B. Fröhlich, M. Enzweiler, and U. Franke. Will this car change the lane?
             - Turn signal recognition in the frequency domain. In *Intelligent Vehicles
             Symposium Proceedings, 2014 IEEE*, pages 37–42, June 8-11 2014. Dear-
             born.

[Fei13]   H. Feigl. Analysis and evaluation: Potential influence of the Euro NCAP
             safety assessment on future brake systems. In *8th Intelligent Braking 2013*,
             pages 1–25, 26-27 November 2013. Frakfurt.

[Föl08]   O. Föllinger. *Analyse linearer und zeitinvarianter Systeme im Zustand-
             sraum*, chapter 12, pages 416–463. Regelungstechnik. Hüthing Verlag, Hei-
             delberg, 10 edition, 2008.

[Gäc12]   J. Gächter. Modellbildung, Reglerentwurf und Simulation eines Abstand-
             sregeltempomatsystems. Masterthesis, 2012. Graz University of Technol-
             ogy.

[Ged09]   G. Geduld. *Lidarsensorik*, chapter 13, pages 172–186. Handbuch Fahreras-
             sistenzsysteme. Vieweg+Teubner, Wiesbaden, 1 edition, 2009.

[Gen13]   Genesys. Technische Dokumentation ADMA. Technical Description ver.
             1.0, September 2013.

[GFB13]   W. R. Garrott, G. Forkenbrock, and F. Barickman. Overview of Advanced
             Braking Technologies that Rely on Forward Looking Sensors. In *2013 SAE
             World Congress and Exhibition*. SAE International, April 16-18 2013. De-
             troit.

[GOR07]   S. Gruber, N. Ocvirk, and J. Remfrey. *Bremssysteme*, chapter 7.2, pages
             475–523. Vieweg Handbuch Kraftfahrzeugtechnik. Friedr. Vieweg & Sohn
             Verlag, Wiesbaden, 5 edition, 2007.

[GPSV06]   O. Gietelink, J. Ploeg, B. De Schutter, and M. Verhaegen. Development of
             advanced driver assistance systems with vehicle hardware-in-the-loop simu-
             lations. *Vehicle System Dynamics*, 44(7):569–590, July 2006.

[GS11]   D. Gunia and J. Schülling. Modellbasiertes Testen des Fahrspur-Assistenten
             von Ford. *Automobiltechnische Zeitschrift*, 113(11):844–848, 2011.

[GT13]   B. Giesler and Müller Thomas. Opportunities and Challenges on the Route

to Piloted Driving. In *chassis.techplus 4th International Munich Chassis Symposium*, pages 1–26, June 13-14 2013. Munich.

[HD04]   M. Horn and N. Dourdoumas. *Einschränkungen beim Entwurf*, chapter 10, pages 185–200. Regelungstechnik. Addison-Wesley Verlag, München, 1 edition, 2004.

[Hir09]   W. Hirschberg. TMsimple: A simple to use tyre model. Technical report, Institut für Fahrzeugtechnik, Graz University of Technology, March 13 2009.

[Hol12]   R. Holl. Integration längsdynamisch regelnder Fahrerassistenzsysteme in das Gesamtfahrzeug. Masterthesis, 2012. Graz University of Technology.

[HW09]   W. Hirschberg and H. Waser. Kraftfahrzeugtechnik. Lecture notes, 2008/09. Institut für Fahrzeugtechnik, Graz University of Technology.

[HW10]   W. Hirschberg and H. Waser. Fahrzeugdynamik. Lecture notes, 2010. Institut für Fahrzeugtechnik, Graz University of Technology.

[Ins13]   Insurance Institute for Highway Safety (IIHS). Autonomous Emergency Braking Test Protocol (Version I). Testing protocol, IIHS, October 2013.

[Ise02]   R. Isermann. *Modellbildung von Maschinen*, chapter 6, pages 205–236. Meschatronische Systeme. Springer-Verlag, Berlin Heidelberg, 1 edition, 2002.

[Kah06]   H. Kahmen. *3D-Positionsbestimmung mit Satellitenverfahren*, chapter 10, pages 310–392. Angewandte Geodäsie: Vermessungskunde. Walter de Gruyer, Berlin, 20 edition, 2006.

[KD97]   U. Kiencke and A. Daiß. Observation of lateral vehicle dynamics. *Control Engineering Practice*, 5(8):1145–1150, June 1997.

[Kol13]   H. Kollienz. Entwicklung eines robusten Schätzers für Fahrzustandsgrößen für die Anwendung in Fahrerassistenzsystemen. Masterthesis, 2013. Graz University of Technology.

[Kre99]   E. Kreyszig. *Data Analysis - Probability Theory*, chapter 22, pages 1050–1103. Advanced Engineering Mathematics. John Wiley & Sons, New York, 8 edition, 1999.

[Lexss]   C. Lex. Estimation of the Maximum Coefficient of Friction between Tire and Road Based on Vehicle State Measurements. PhD Thesis, in press. Graz University of Technology.

[LP99]   C. Liang and H. Peng. Optimal adaptive cruise control with guaranteed string stability. *Vehicle System Dynamics*, 32(4):313–330, 1999.

[LP08]   M. Laiou and A. Pfeiffer. ACC Stop&Go bei der BMW Group: Übergänge in und aus dem Stillstand und Stillstandsmanagement. In *Integrierte Sicherheit und Fahrerassistenzsysteme*, pages 45–54, October 29-30 2008. Wolfsburg.

[LSKW10]   U. Lüthin, P. Schmok, L. Kühnke, and M. Wintermantel. Technical Description of the Radar System ARS300 - Industrial. Technical Description rev. 2.3, July 13 2010.

[Mag13]   Z. Magosi. Modellbildung und Simulation eines Radarsensors für die virtuelle Entwicklung von Fahrerassistenzsysremen. Masterthesis, 2013. Technische Universität Széchenyi István, Györ.

[Mah88]   B. R. Mahafza. *Introduction to Radar Analysis*. CRC Press, Boca Raton, 1988.

[Mau09]   M. Maurer. *Entwurf und Test von Fahrerassistenzsystemen*, chapter 5, pages 43–54. Handbuch Fahrerassistenzsysteme. Vieweg+Teubner, Wiesbaden, 1 edition, 2009.

[Men99]   R. Mende. Radarsysteme zur automatischen Abstandsregelung in Automobilen. Dissertation, 1999. Technische Universität Carolo-Wilhemina zu Braunschweig.

[MW04]   M. Mitschke and H. Wallentowitz. *Zweispurmodell, Vierradfahrzeug*, chapter 21, pages 710–758. Dynamik der Kraftfahrzeuge. Springer, Berlin, 4 edition, 2004.

[MY08]   S. Moon and K. Yi. Human driving data-based design of a vehicle adaptive cruise control algorithm. *Vehicle System Dynamics*, 46(8):661–690, 2008.

[Nat12]   National Highway and Traffic Safety Administration (NHTSA). Crash Imminent Braking System Performance Evaluation. Technical report, June 2012.

[Nat13a]   National Highway and Traffic Safety Administration (NHTSA). Forward Collision Warning System Confirmation Test. Testing protocol, February 2013.

[Nat13b]   National Highway and Traffic Safety Administration (NHTSA). Laboratory Test Procedure for the New Car Assessment Programm Electronic Stability Control Testing and FMVSS No. 126, Electronic Stability Control Systems Indicative Test for Compliance. Testing protocol, February 7 2013.

[Nat13c]   National Highway and Traffic Safety Administration (NHTSA). Lane Departure Warning System Confirmation Test and Lane Keeping Support Performance Documentation. Testing protocol, February 2013.

[Obe12]   H. J. Oberle. Optimierung. Lecture notes, 2012. Fachbereich Mathematik, Universität Hamburg.

[Off11]   Office for Official Publications of the European Commission. Roadmap to a Single European Transport Area - Towards a competitive and resource efficient transport system. White paper COM(2011) 144 final, European Commission, 2011.

[Raj06]   R. Rajamani. *Adaptive Cruise Control*, chapter 6, pages 153–186. Vehicle Dynamics and Control. Springer Science+Business Media, New York, 1 edition, 2006.

[Rei12]   K. Reif. *Funktions- und Softwareentwickung*, chapter 3, pages 61–81. Automobilelektronik. Vieweg+Teubner, Wiesbaden, 4 edition, 2012.

[Rob02]   Robert Bosch GmbH. *Autoelektrik Autoelektronik*. Friedr. Vieweg & Sohn Verlag, Braunschweig, 2002.

[Rob04]   Robert Bosch GmbH. *Adaptive Fahrgeschwindigkeitsregelung ACC*, chapter 12, pages 154–197. Sicherheits- und Komfortsysteme. Friedr. Vieweg & Sohn Verlag, Wiesbaden, 3 edition, 2004.

[RS40]   P. Riekert and T. E. Schunck. Zur Fahrmechanik des gummibereiften Kraftfahrzeugs. *Archive of Applied Mechanics*, 11(3):210–224, 6 January 1940.

[SAE03]   SAE Safety and Human Factors Commitee. SAE J2399 - Adaptive Cruise Control (ACC) Operating Characteristics and User Interface. Standard SAE J2399, SAE International, December 2003.

[SBB+07]   B. Schick, R. Büttner, K. Baltruschat, G. Meier, and H. Jakob. Methoden zur Bewertung von Funktion und Güte von Fahrerassistenzsystemen. In *Erprobung und Simulation in der Fahrzeugentwicklung*, pages 375–392. VDI, June 21-22 2007. Würzburg.

[SBD09]   C. Stiller, A. Bachmann, and C. Duchow. *Maschinelles Sehen*, chapter 15, pages 198–222. Handbuch Fahrerassistenzsysteme. Vieweg+Teubner, Wiesbaden, 1 edition, 2009.

[SEFL14]   Y. Shtessel, C. Edwards, L. Fridman, and A. Levant. *Introduction: Intuitive Theory of Sliding Mode Control*, chapter 1, pages 1–42. Sliding Mode Control and Observation. Springer Science+Business Media, New York, 1 edition, 2014.

[SGS10]   G. P. Stein, Y. Gdalyahu, and A. Shashua. Stereo-assist: Top-down stereo for driver assistance systems. In *IEEE Intelligent Vehicles Symposium*, pages 723–730. IEEE, June 21-24 2010. San Diego.

[SLZB14]   S. Schwab, T. Leichsenring, R. Zofka, and T. Bär. Durchgängige Testmethode für Assistenzsysteme. *ATZ Automobiltechnische Zeitschrift*, 116(9):54–59, 2014.

[SMS03]   G. P. Stein, O. Mano, and A. Shashua. Vision-based ACC with a single camera: bounds on range and range rate accuracy. In *IEEE Intelligent Vehicles Symposium*, pages 120–125. IEEE, June 9-11 2003. Columbus.

[Soc14]   Society of Automotive Engineers (SAE). Taxonomy and Definitions for Terms Related to On-Road Motor Vehicle Automated Driving Systems. Standard SAE J3016, January 2014.

[SS13]   M. Schrauf and P. Schöggl. Objective Driveability Assessment of Auto-
           mated / Autonomous Driving. In *International AVL Converence Engine &
           Environment*, pages 1–38, September 5-6 2013. Graz.

[Sta08]   Statistisches Bundesamt Deutschland. Unfallgeschehen im Straßenverkehr
           2007. Statistical report 5462401089004, Statistisches Bundesamt Deutsch-
           land, August 5 2008.

[Tec09]   Technical Committee ISO/TC 204. Intelligent transport systems - Full
           speed range adaptive cruise control (FSRA) systems - Performance require-
           ments and test procedures. Standard ISO 22179:2009(E), International Or-
           ganisation for Standardization (ISO), September 1 2009.

[Tec10]   Technical Committee ISO/TC 204. Intelligent transport systems - Adaptive
           Cruise Control systems - Performance requirements and test procedures.
           Standard ISO 15622:2010(E), International Organisation for Standardiza-
           tion (ISO), April 4 2010.

[Ton08]   A. A. Tonchev. Co-Simulation von Fahrzeugbremsen unter Berücksichti-
           gung des thermischen Verhaltens. PhD Thesis, 2008. Graz University of
           Technology.

[Wal12]   D. Wallner. Experimental and Numerical Investigations on Brake Squeal.
           PhD Thesis, 2012. Graz University of Technology.

[WDS09]   H. Winner, B. Danner, and J. Steinle. *Adaptive Cruise Control*, chapter 32,
           pages 478–521. Handbuch Fahrerassistenzsysteme. Vieweg+Teubner, Wies-
           baden, 1 edition, 2009.

[Weg09]   M. Wegscheider. Modellbasierte Komfortbewertung von Fahrerassistenzsys-
           temen. Dissertation, 2009. Graz University of Technology.

[Win09]   H. Winner. *Radarsensorik*, chapter 12, pages 123–171. Handbuch Fahreras-
           sistenzsysteme. Vieweg+Teubner, Wiesbaden, 1 edition, 2009.

[WSSR10]   U. Wehner, K. Schulze, B. Schonlau, and L. Rudolf. Entwicklung von Assis-
           tenzfunktionen am Fließband. *Automobiltechnische Zeitschrift*, 112(2):92–
           97, 2010.

[WWL+04]   H. Winner, K. Winter, B. Lucas, H. Mayer, A. Irion, H. Schneider, and
           J. Lüder. *Adaptive Fahrgeschwindigkeitsregelung ACC*, chapter 9, pages
           154–197. Sicherheits- und Komfortsysteme. Friedr. Vieweg & Sohn Verlag,
           Wiesbaden, 3 edition, 2004.

[XZ12]   Z. Xia and D. Zhao. Hybrid feedback control of vehicle longitudinal accel-
           eration. In *31st Chinese Control Conference (CCC)*, pages 7292–7297, July
           25-27 2012. Hefei.

[YSZS10]   R. Yim, M. Saito, J. Zhang, and N. Shimizu. Digital Lane Marking for
           Geo-Information Dissemination. In *17th ITS World Congress*, pages 1–12,
           October 25-29 2010. Busan.

[ZLC11]   Lin-Hui Zhao, Zhi-Yuan Liu, and Hong Chen. Design of a Nonlinear Observer for Vehicle Velocity Estimation and Experiments. *IEEE Transactions on Control Systems Technology*, 19(3):664–672, May 2011.